A Search for $B^+ \to K^+\nu\overline{\nu}$

by

Paul D. Jackson

M.Phys., Lancaster University, 1998.
M.Sc., University of Victoria, 2001.

A Dissertation Submitted in Partial Fulfillment of the
Requirements for the Degree of
DOCTOR OF PHILOSOPHY
in the Department of Physics and Astronomy.

Supervisor: Dr. R. V. Kowalewski

Abstract

A search for the rare, flavour-changing neutral current decay $B^+ \to K^+\nu\overline{\nu}$ is presented using 81.9 fb^{-1} of data collected at the $\Upsilon(4S)$ resonance by the *BABAR* experiment. Signal candidate events are selected through the identification of a high momentum charged kaon and significant missing energy, where the companion B^- in the event has decayed semileptonically via $B^- \to D^0\ell^-\overline{\nu}\ X$ and X is kinematically constrained to be either nothing or a low momentum transition photon or π^0. The analysis was performed blind and 6 candidates were selected with a background expectation of 3.4±1.2. This leads to a limit on the branching fraction of $\mathcal{B}\ (B^+ \to K^+\nu\overline{\nu}\ ) < 7.2 \times 10^{-5}$ at 90% confidence level. We also search for the reaction $B^+ \to \pi^+\nu\overline{\nu}$ and extract a limit on the branching fraction of $\mathcal{B}\ (B^+ \to \pi^+\nu\overline{\nu}\ ) < 2.5 \times 10^{-4}$ at 90% confidence level.

Contents

List of Tables

List of Figures

Acknowledgements

My thanks should really go to Bob Kowalewski. He has supervised this worked from its very inception and should be praised for that. Bob has achieved a fine balance between maintaining my interest, leading me along the right path and just leaving me alone to get on with things. A delicate balance to achieve with a student who is, at the best of times, difficult to read and understand. I salute you sir !

Let me take the oppurtunity to express my appreciation of others in the UVic Particle Physics group: Mike Roney, who leads the *BABAR* group, has been a constant support; Michel Lefebvre, Richard Keeler and Randy Sobie have provided great teaching, experienced leadership and a friendly environment among other things. I would also thank Charles Picciotto and Maxim Pospelov for some interesting lectures and discussions. The faculty at UVic provide a constant inspiration to work and achieve which isn't so easy when Victoria surrounds one with such natural beauty and ideal excuses to laze around procrastinating.

As I mention laziness and procrastination that leads me smoothly into mentioning the grad students in physics and astronomy at UVic. Dominique Fortin started as a graduate student at the same time as I did. He has been a great friend throughout my time in Victoria and I couldn't even begin to express my gratitude for that. Cheers Dom, may your star continue to shine brightly. My thanks go out to all the others who have been graduate students in the physics and astronomy group in Victoria during my time here.

Since I have you reading, I'll mention a few people from my time at SLAC who kept things moving along nicely: Steve Robertson, for his expert (and always humble) leadership of the Leptonic working group, Steve Sekula and Justin Albert, who joined me in the often painful process of ntuple production, and to all the good (and some of the bad) people of the *BABAR* collaboration who made the working environment at SLAC relaxed yet productive. During my time at SLAC my sanity was preserved by people such as Simon Jolly, Ed Hill, Kelly Ford and Sian Morgan. In one way or another they, and many others, helped me through my months at SLAC.

Of course, a balanced lifestyle is one of the keys to any achievement. In this aspect

of life I have indeed been blessed. Victoria has provided me with some good friends over the years who have helped me forget about my troubles when I had oh so many of them. My roommates at Wessex: Andrew Bohan (young priest), Mike Brown and Jay Meyer, plus Sean Farrell (old priest), were always around and perfectly in tune with my own social habits. I thank those guys for the parties, and the memories. Laura Vanags provided much needed help and support throughout the final year of my PhD. Her friendship has provided me with much happiness and has been such a great gift.

My final word of thanks I save for my family and friends back in England. Although so far away, they continue to provide me with their unwavering support and love. Particularly my parents, Arthur and Hilary. Whatever I write here will not express how truly grateful I am to them. They inspire and guide me and provide the foundation upon which I am lucky enough to build my life.

Chapter 1

Introduction

The purpose of research in particle physics is to uncover a description of, and provide a way to understand, the fundamental elements of nature. Over the last one hundred years this study has led to a view that the Universe is composed of a few fundamental particles and interactions which combine to paint an elegant portrait of the world around us. This description is summarized in the *Standard Model of Particle Physics*, generally referred to, simply, as the Standard Model. The predictive power of this model has been in exceptionally good agreement with experimental tests, and, it has been highly descriptive and successful at establishing the behaviour of particles and interactions. There are, however, many input parameters which have to be provided to the model, and hence, it is not able to predict all physical phenomena. It is believed that sufficiently high precision tests of Standard Model predictions will yield inconsistencies. Such discrepancies provide windows through which one may see new physical principles at work. One such opportunity is presented by the study of processes disallowed by the Standard Model, or processes which are inherently rare in their nature. These reactions have the potential to shed light on mysteries beyond the Standard Model as they are sensitive to effects which may considerably enhance their rate. The large sample of B mesons which the PEP-II/*BABAR* B–factory provides

lays fertile ground to test predictions of rare decays in the Standard Model, and, search for possible exciting new phenomena which may lie just beyond it.

1.1 Thesis Outline

In section 1.2 an outline of particle physics is provided while section 1.3 summarizes the analyses. In chapter 2 our current understanding of the subatomic world is presented, followed by an introduction to the relevant aspects of the Standard Model of particle interactions. Chapter 2 also includes a brief theoretical background to the work described herein. The experimental environment in which this work was carried out is presented in chapter 3, and the samples used are described in chapter 4. Chapters 5 to 9 are devoted to the details of the analyses undertaken and results are presented in chapter 10. Chapter 11 summarizes the results of the thesis.

1.2 Theory Overview

The Standard Model is composed of two types of fundamental[1] particles: fermions and bosons. Fermions can be subdivided into two categories: leptons and quarks, each of which has three generations. They carry integer charge, in the case of leptons, and one-third integer charge, in the case of quarks. Leptons interact, and are governed by the electroweak force; the same is true for quarks, which are also subjected to the strong force. Each quark has an associated colour 'charge', where colour is the charge by which the strong force couples. There are three types of colour charge which are distinguished by the labels red, blue and green. Each fermion has a corresponding

[1]This refers, in general, to a structure that is indivisible. It should not be confused with the term 'stable' since there are fundamental particles which are not stable and directly they are produced, they decay.

anti-particle[2] partner anti-fermion. In summary, the quark sector is composed of six *flavours* of quark, u, d, c, s, t, b, each of which can come in three colours. Each quark has a corresponding anti-particle, $\overline{u}$, $\overline{d}$, $\overline{c}$, $\overline{s}$, $\overline{t}$, $\overline{b}$, which can carry three anti-colours. There are three types of charged lepton: the electron, e^-, the muon, μ^-, and the tau, τ^-, where the sign denotes the particle charge. Each charged lepton is paired with a neutrino of the same type i.e. ν_e is paired with the e^- and the ν_μ and ν_τ are paired with the μ^- and τ^- respectively. Furthermore there are anti-particles for all of the leptons.

The quarks bind together in one of two ways: either as *mesons*: a quark and anti-quark pair, or as *baryons*: combinations of three quarks and/or anti-quarks. These are the only stable combinations of quarks that occur in nature and free quarks are forbidden.[3]

The fundamental forces of nature are mediated by the exchange of vector bosons, the second type of fundamental particles referred to above. The strong force is propagated by gluons which will not be described here. The photon, $W^\pm$ and Z^0 gauge bosons propagate the electroweak force. The photon, being massless, differs from the W and Z bosons since they are heavy (approximately 10^5 times heavier than an electron). The difference in apparent strengths between the electromagnetic and weak forces can be accounted for by this fact.

---

[2]An anti-particle has identical mass as the particle but has opposite electric charge and opposite colour charge. Some particles, such as the photon, are their own anti-particles.

[3]The coupling "constant" in strong interactions is, in fact, not constant, but depends on the distance of separation between the interacting particles. At short distances (less than the size of the proton) it is quite small but at large distances (charateristic of nuclear physics) it is big. This phenomenon is known as *asymptotic freedom*.

1.3 Analysis Overview

The B mesons created at the *BABAR* experiment consist of a anti-b quark paired with a lighter quark, either u or d. B mesons can be either charged, B^+ ($\bar{b}u$), or neutral, B^0 ($\bar{b}d$). This analysis will focus on B^+ decays. The mesons studied in *BABAR* are created in pairs from the decay of the $\Upsilon(4S)$ resonance i.e. $\Upsilon(4S) \rightarrow B^+B^-$.[4] The analyses presented in this thesis will involve searching for intrinsically rare decay modes of the type $B^+ \rightarrow Y\nu_\ell\overline{\nu}_\ell$, where $Y = K^+$ or π^+. Of the final state particles, only the Y system will be detectable.[5] In order to study this decay we begin by reconstructing[6] the other B meson in the event[7] to a set of detectable final states. After constraining the decay of one B meson to undergo the reaction $B^- \rightarrow D^0\ell^-\overline{\nu}\,X$,[8] the remainder of the event is studied for consistency with the signal decay modes under investigation.

---

[4]Studies of the $\Upsilon(4S)$ resonance have shown that it decays $\approx$50% of the time into either B^+B^- or $B^0\overline{B}^0$ pairs.

[5]Neutrinos (which are only subject to the weak force) interact very rarely with matter, which means, to high energy collider detector experiments, like *BABAR*, they are undetectable.

[6]The term "reconstruction" refers to the detection and identification of the particles associated with a particular decay.

[7]An event is considered to be produced each time the two beams cross and the minimum trigger requirements are satisfied within the detector.

[8]Although the charge of the B meson exemplifying the signal decay and the charge of *the other* B meson that is reconstructed are distinguished the charge assignments can in principle be exchanged. The convention chosen here, such that, signal $\Rightarrow$ B^+ and *the other* $\Rightarrow$ B^- (it may seem like "*the other* B" is somewhat loose terminology but much more detail will be provided later) will be adhered to throughout.

Chapter 2

Theory

2.1 Introduction

The decay $B^+ \rightarrow K^+\nu\overline{\nu}$ is a flavour-changing neutral current interaction. In this chapter, we discuss how these processes arise in the Standard Model of particle interactions and why they are of interest, potentially in extracting the Cabibbo-Kobayashi-Maskawa matrix elements V_{ts}. We investigate how the theory allows the rate of these decays to be predicted using techniques such as the Operator Product Expansion. The decay $B^+ \rightarrow K^+\nu\overline{\nu}$ is also a probe of new physics outside of the Standard Model. We discuss possible signatures of such new phenomena in these decays. Finally we summarize the current status of experimental results and theoretical calculations.

2.2 The Standard Model

2.2.1 Basic Principles

The Standard Model endeavours to explain phenomena within the realm of elementary particles and their interactions. It has thus far explained all experimental results, with exception of the generation of neutrino masses and the unobserved Higgs boson. The Standard Model is built upon a foundation of relativistic *quantum field theory*, which

embeds the dynamic framework of quantum mechanics within the spacetime structure of special relativity [1]. To this, we add the principle of *gauge invariance* [2], which postulates that the theory is invariant under transformations of the fields of the form:

$$\psi(x_\mu) \rightarrow e^{i\alpha_a(x)T_a}\psi(x_\mu), \tag{2.1}$$

where the T_a are the generators of the Lie group and the $\alpha_a(x)$ are a set of arbitrary real functions of the space-time coordinate x_μ, one for each generator. A gauge invariance within a quantum field theory forces the introduction of one or more spin 1 bosons which mediate an interaction between the matter fields. This interaction is characterized by a universal coupling constant and conserved charges. Quantum electrodynamics can be expressed as a quantum field theory with gauge invariance under the group $U(1)$. The Standard Model involves more complicated groups which endow it with a richer structure. Finally we will need the mechanism of *spontaneous symmetry breaking* [3] to generate the observed masses of the particles. We will find that effective flavour-changing neutral current processes, otherwise forbidden, are enabled as a consequence.

2.2.2 The Fundamental Constituents and their Interactions

The Standard Model of particle interactions is illustrated in Figure 2.1 as a survey of the elementary particles. The first division among these particles occurs between *bosons* carrying integer spin and *fermions* carrying half-integer spin. Each particle has a corresponding antiparticle which carries the opposite quantum numbers. In some cases, as with the photon and the Z, the particle is its own antiparticle. The spin-1 bosons are responsible for the electroweak and the strong interactions, the latter being described by quantum chromodynamics (QCD). We set aside the spin-0

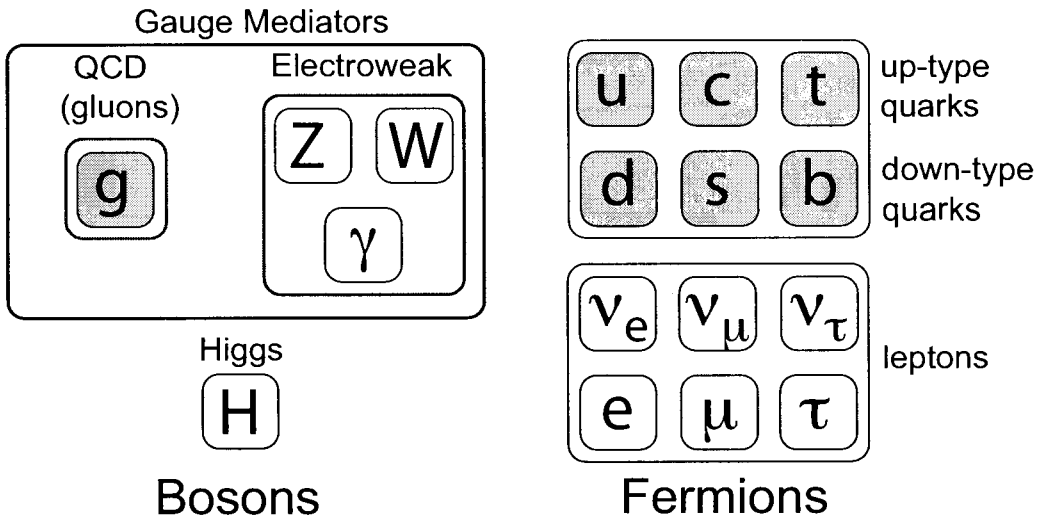

Figure 2.1: The constituents of the Standard Model of particle interactions.

Higgs field for later discussion. The gauge bosons arise from the gauge invariance of the quantum field theory: in order to preserve the gauge invariance of the kinetic term, it is necessary to introduce *gauge fields*, A^a_μ, by modifying the derivative term δ_μ into the covariant derivative D_μ:

$$\delta_\mu \rightarrow D_\mu = \delta_\mu + igT^a A^a_\mu \tag{2.2}$$

where the A^a_μ transform as:

$$A^a_\mu \rightarrow A^a_\mu - \frac{1}{g}\delta_\mu \alpha_a(x) \tag{2.3}$$

The T_a are the generators of the chosen Lie algebra, $SU(3)$ [4] in the case of QCD and $SU(2)_L \times U(1)_Y$ [5] for the electroweak interactions. The subscript L indicates that the charged-current weak force couples only to left-handed fermions.[1]

[1]The fermions are grouped into left-handed (i.e. chiral left) weak isospin doublet fields, and right-handed singlets.

The subscript Y denotes the weak hypercharge, defined by $Q = T^3 + Y/2$ where Q is the electric charge and T^3 is the third component of weak isospin. The A^a_μ are fields whose quanta of excitation are the particles mediating the elementary interactions in the Standard Model. Gauge and Lorentz invariance dictate that they are spin-1 Lorentz vector fields transforming under the adjoint representation of the group. The factor g is the universal coupling constant for the gauge group determining the strength of the interaction, with the covariant derivative constructed in such a way that the transformations of the gauge field cancel terms arising from the derivative of the gauge transformed field. The eight gauge bosons mediating chromodynamics are called gluons, while the four gauge bosons of the electroweak interactions after spontaneous symmetry breaking (described in section 2.2.3) are the $W^\pm$, the Z, and the photon γ. The representation of the T_a matrices within the covariant derivative for the fermions determines their group transformation and gauge interaction properties. If the T_a are a non-trivial representation of the group, the fermions couple with the corresponding gauge bosons via terms in the covariant derivative. Otherwise, they are singlets under the gauge group and do not interact through this interaction. In this way, the fermions are divided into two categories:

- Six *quarks*, which transform under the fundamental representation of chromodynamics, $SU(3)$, are said to carry colour (chromodynamic charge) and hence participate in QCD.

- Six *leptons*, which are $SU(3)$ singlets, carry no colour and do not interact via QCD.

The six quarks are classified into "up"-type quarks with electric charge $+2/3$ and "down"-type quarks with electric charge $-1/3$. They are divided into three gen-

erations, as depicted horizontally in figure 2.1. Pairs of left-handed up and down-type quarks in each generation are doublets of the $SU(2)_L$ gauge group of the electroweak interaction. The interaction projects out the left-handed component of the fermion field, resulting in parity violation. The right-handed components are singlets of $SU(2)_L$. The anti-fermions appear as conjugate terms in the Lagrangian, with the right-handed anti-fermions forming doublets and left-handed anti-fermions forming singlets. The leptons are likewise divided horizontally into generations and vertically into a $SU(2)_L$ doublet consisting of a neutrino, carrying no electric charge, and a charged lepton with electric charge -1. The various types of quarks and leptons (e.g. up, strange, μ, τ) are collectively called flavours.

2.2.3 The Weak Interaction

Spontaneous Symmetry Breaking

The manifestation of the mediators of the electromagnetic and weak interactions in the form of the massless photon and the massive W and Z is the result of the *spontaneous symmetry breaking* of the $SU(2)_L \times U(1)_Y$ gauge symmetry. Spontaneous symmetry breaking allows the creation of massive gauge bosons without spoiling the gauge symmetry which would otherwise result if explicit mass terms were inserted directly into the Lagrangian for the W and Z, something which is true for any particle. At the heart of the symmetry breaking is the introduction of the Higgs scalar field. While any number of gauge invariant configurations that are non-trivial representations of $SU(2)_L$ can break the symmetry, the simplest is a single $SU(2)_L$ doublet:

$$\phi = \begin{pmatrix} \phi^+ \\ \phi^0 \end{pmatrix} \tag{2.4}$$

We assume that the Higgs field carries no colour.

In order to preserve the gauge symmetry, the kinetic term of the Higgs field must enter via the gauge-covariant derivative:

$$L = |(\delta_\mu + igT^i \cdot W^i_\mu + ig'\frac{Y}{2}B_\mu)\phi|^2 - V(\phi) \tag{2.5}$$

Here the W^i_μ triplet and B_μ gauge bosons are introduced via gauge symmetry under the $SU(2)_L$ and $U(1)_Y$ groups, respectively. The Higgs potential $V(\phi)$ is such that its minima are at non-zero values of the Higgs field. The Higgs field then has a non-zero vacuum expectation value v and the $SU(2)_L \times U(1)_Y$ gauge fields acquire mass from terms quadratic in the Higgs field. In order to identify the physical manifestation of these fields, we identify the mass eigenstates. The combination $W^\pm_\mu = W^1_\mu \pm iW^2_\mu$ is diagonal with mass $\frac{1}{2}vg$. The other two fields are off-diagonal in the mass matrix; after diagonalising the mass matrix the eigenstates are:

$$A_\mu = \frac{g^{'}W^3_\mu + gB_\mu}{\sqrt{g^2 + g'^2}} \qquad Z_\mu = \frac{gW^3_\mu - g^{'}B_\mu}{\sqrt{g^2 + g'^2}} \tag{2.6}$$

with eigenvalues:

$$M_A = 0 \qquad M_Z = \frac{1}{2}v\sqrt{g^2 + g'^2} \tag{2.7}$$

In the aftermath, we identify the massless gauge field from the remaining $U(1)$ symmetry with the photon and the three massive bosons with the weak interaction. Fermion masses are likewise generated from the vacuum expectation value of the Higgs field via Yukawa terms:

$$-M[\overline{\psi}_L\phi\psi_R + \overline{\psi}_R\phi^\dagger\psi_L] \tag{2.8}$$

where M is arbitrarily chosen to construct the observed mass of the fermion. The

Standard Model makes no predictions for these fermion masses; they are input parameters to the theory which must be determined from experiment. The mechanism of spontaneous symmetry breaking thus generates all boson and fermion masses in the Standard Model and makes the theory renormalizable. Since we defined the Higgs field as a $SU(3)$ singlet, the $SU(3)$ symmetry of QCD is not broken, leaving the gluons massless.

2.2.4 Flavour-Changing Interactions

The Weak Charged Current

The W boson can mediate flavour-changing charged current interactions in the quark sector arising from terms:

$$-i\frac{g}{\sqrt{2}}\bar{d}\gamma^{\mu}\frac{1-\gamma^5}{2}uW_{\mu}^{+} + \text{H.C.},^{2} \tag{2.9}$$

where d is a down-type quark and u is an up-type quark. However, the mass eigenstates of the six quarks do not correspond to the flavour eigenstates, but are mixed in a unitary transformation. The transformation is described by a unitary 3×3 matrix V, known as the Cabibbo-Kobayashi-Maskawa (CKM) matrix [6]. The charged-current weak interactions between the three up-type quarks and the three down-type quarks can be summarized as:

$$(\overline{u},\overline{c},\overline{t})\frac{\gamma^{\mu}(1-\gamma^5)}{2}\begin{pmatrix} V_{ud} & V_{us} & V_{ub} \\ V_{cd} & V_{cs} & V_{cb} \\ V_{td} & V_{ts} & V_{tb} \end{pmatrix}(d,s,b)W_{\mu}^{-} + \text{H.C.} \tag{2.10}$$

where we have spelled out the CKM matrix explicitly. Unitarity and phase rotations of the quark wavefunctions allow the nine elements of the matrix to be expressed in

[2] H. C. $\Rightarrow$ Hermitian Conjugate

terms of three angles and one phase. Kobayashi and Maskawa proposed that this phase was the origin of CP violation and argued that at least three generations of quarks must exist in order for unitarity to permit a non-trivial phase. This prediction was made at a time when only three of the six quarks, up down and strange, were known to exist.

While the weak interactions are characterised by a universal coupling constant resulting from the $SU(2)_L \times U(1)_Y$ symmetry, the intergenerational quark interactions are scaled by the appropriate CKM matrix elements; certain transitions have greater rates due to favourable CKM elements whereas others are suppressed. The theory makes no predictions for the values of these elements aside from unitarity; they are yet another set of arbitrary parameters which must be obtained from experiment. Since the individual elements of the CKM matrix can be measured independently without invoking the theoretical requirement of unitarity, the requirement of unitarity can be used to overconstrain the CKM matrix and test the Standard Model of weak interactions.

The unitarity of the CKM matrix is conveniently summarized in *unitarity triangles*. In particular, unitarity imposes the following constraint on elements of the first and third column of the CKM matrix:

$$V_{ud}^* V_{ub} + V_{cd}^* V_{cb} + V_{td}^* V_{tb} = 0 \tag{2.11}$$

This is expressed graphically in the complex plane as a triangle in figure 2.2, where the sides of the triangle have been normalised and rotated by the second term in equation 2.11, which consists of relatively well known elements of the CKM matrix. The sides of the triangle, which correspond to magnitudes of the CKM elements, can be measured by analysing the rates of processes which involve these CKM elements.

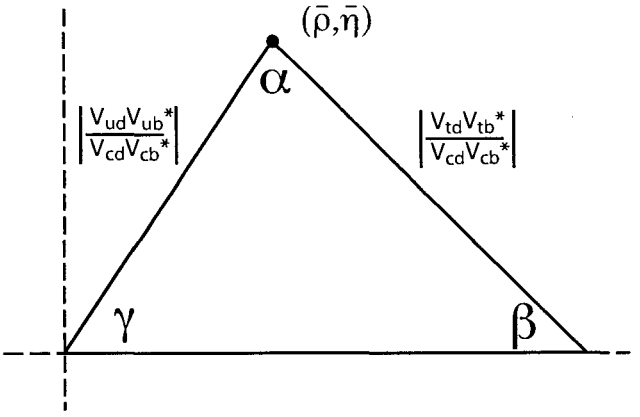

Figure 2.2: Unitarity triangle summarizing the orthogonality of the first and third columns of the CKM matrix. The length of the side of the triangle positioned on the x axis is normalised to be unity.

The angles, which correspond to relative phases between the elements, can be measured by CP-violating asymmetries.

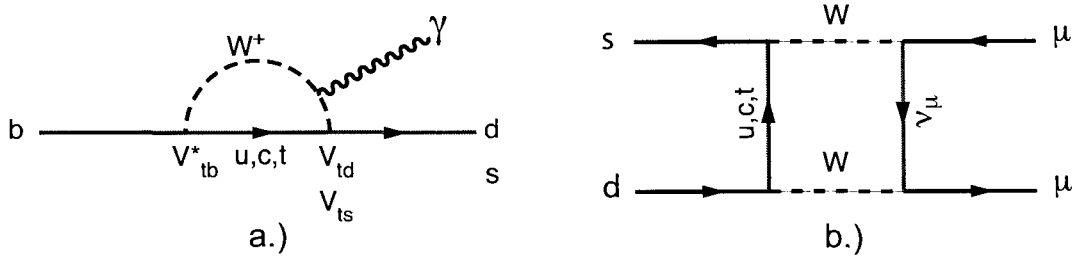

Figure 2.3: Effective Flavour-changing neutral current processes a.) $b \rightarrow d/s\gamma$ penguin diagram and b.) $K^0 \rightarrow \mu^+\mu^-$ box diagram.

GIM Mechanism

The coupling of the quarks to the neutral Z boson are flavour-diagonal by definition, with the result that there are no tree-level *flavour-changing neutral currents* in the

Standard Model. Such reactions can only proceed at higher orders in loop processes such as "penguin" and "box" diagrams shown in figure 2.3. These processes are collectively known as *effective flavour-changing neutral currents*. Unitarity of the CKM matrix has profound consequences for effective flavour-changing neutral currents. In the limit of degenerate quark masses they are forbidden: unitarity of the CKM matrix demands that the separate contributions from the quarks that mediate the loop cancel each other in the sum [7]. As an example the $b \rightarrow s\gamma$ penguin transition shown in figure 2.3 a) contains contributions from the three up-type quarks that mediate the loop scaled by the appropriate CKM matrix elements:

$$V_{tb}^{*}V_{ts} + V_{cb}^{*}V_{cs} + V_{ub}^{*}V_{us} \tag{2.12}$$

This quantity is identically zero from the unitarity relations between the second and third columns of the CKM matrix. The different quark masses break the degeneracy and allow these processes to occur at suppressed rates. Historically, Glashow, Illiopolous and Maiani proposed the existence of the charm quark, at a time when only three quarks were thought to exist, to explain the highly suppressed rate of $K_L^0 \rightarrow \mu^+\mu^-$, which could only proceed through diagrams like the box shown in figure 2.3 b). In the GIM mechanism, the contribution of the charm quark in the loop would cancel the contribution of the up quark in the diagram through orthogonality of the 2×2 matrix (corresponding to the unitarity of the CKM matrix). The GIM mechanism also explained the absence of flavour-changing Z interactions which would occur if the strange quark were not part of a weak $SU(2)_L$ doublet [8].

The spontaneous symmetry breaking process, which endows the quarks with different masses, is thus responsible for breaking the GIM mechanism in loop processes by disturbing the balance imposed by the unitarity of the CKM matrix, which would

otherwise forbid effective flavour-changing neutral current processes.

2.3 Radiative decays in the Standard Model

Effective flavour-changing neutral current processes proceed through virtual loops and thereby offer a testing ground of physics at high mass scales. We find a peculiar situation where the enormous mass of the top quark relative to the other quarks weakens the GIM suppression and enhances its contribution in these processes. If the CKM matrix elements of the up and charm contributions are known, we can isolate the top contribution to such processes, allowing the extraction of the corresponding CKM matrix elements involving the top quark. The weak interaction properties of the top quark, with mass of 175±9 GeV/c^2 [9], are thus accessible at much lower energy through these processes.

In addition, these processes are sensitive to other flavour-changing interactions not present in the Standard Model that may mediate the loop. Such contributions can affect the rate of the process. Hence, flavour-changing neutral currents are also sensitive to physics beyond the Standard Model.

2.3.1 The Operator Product Expansion

The Operator Product Expansion [10] expresses the full diagrammatic theory of an effective Hamiltonian constructed from a set of local operators $\mathcal{O}_i$, where the amplitude for a given process $I \rightarrow F$ (representing the intial, I, and final, F, states) is expressed as a sum of matrix elements of the local operators:

$$\langle F|\mathcal{H}_{\text{eff}}|I\rangle = \frac{G_F}{\sqrt{2}} \sum_i V_i C_i(\mu) \langle F|\mathcal{O}_i(\mu)|I\rangle \tag{2.13}$$

Here G_F is the Fermi constant, characterising the strength of the underlying weak

processes. The V_i are the appropriate CKM matrix elements for a given quark transition and the $\mathcal{O}_i$ are the local operators categorized by Dirac and colour structure forming a complete set for a given transition. The *Wilson coefficients*, C_i, serve as the numerical coefficients associated with these effective interactions. The amplitude of the effective Hamiltonian is thus expressed as a sum of local operator amplitudes and their Wilson coefficients. The division of mass scales is implied by the μ–dependence of the Wilson coefficients and the operators. The Wilson coefficients summarize the effects of interactions at scales higher than μ, while the operators absorb all the effects that occur at scales below μ. The choice of μ is arbitrary but is typically chosen to be $\mathcal{O}(m_b)$ for the study of B decays. Fortunately this is well above the scale $\Lambda_{\rm QCD}$ where perturbative QCD starts to break down. The operator product expansion offers a useful way to summarize the expected effects of new physics contributions from scales higher than μ. Since we integrate over these new degrees of freedom, they result, simply, in a modification of the Wilson coefficients in the Standard Model or additional Wilson coefficients associated with new operators that may be introduced with the new physics.

Therefore, in principle, the choice of μ should have no impact on the physical results of the calculation. It represents an arbitrary border line between physics occurring at "higher" and "lower" scales. As a result, the μ–dependence of the Wilson coefficients and the operator matrix elements must cancel. In practice however the Wilson coefficients contain explicit dependence on μ due to the truncation of the perturbative expansion; a full calculation to all orders would naturally eliminate this dependence, but is impractical to perform.

The Wilson coefficients are calculated by matching the predictions of the effective theory with the full theory with all degrees of freedom at a high mass scale,

typically M_W, where the relevant diagrams and their QCD corrections can be calculated via perturbation theory and evolved down to the relevant energy scale (in this case the b quark mass) via renormalization group equations. After renormalization, the operators can be identified within the full calculation and the Wilson coefficients extracted.

2.3.2 $B^+ \to K^+\nu\overline{\nu}$ in the Standard Model

The quark level process $b \to s\nu\overline{\nu}$ represents a rare effective flavour-changing neutral-current decay which is forbidden at tree-level in the Standard Model. Instead, it proceeds at the one-loop level via "penguin" and "box" diagrams such as those shown in figure 2.4, which are similar to the diagrams for the rare decay process $b \to s\,\ell^+\ell^-$ [11], except that the photonic penguin diagram is not allowed. In addition, the inclusive $b \to s\nu\overline{\nu}$ process is nearly free from theoretical uncertainties associated with strong interaction effects, permitting a fairly precise prediction of the Standard Model rate.

Within the Standard Model the process $b \to s\nu\overline{\nu}$ is governed by the effective Hamiltonian [12]

$$\mathcal{H}_{\text{eff}} = \frac{G_F}{\sqrt{2}}\frac{\alpha}{2\pi\sin^2(\theta_W)}V_{ts}V_{tb}^*X(x_t)\bar{b}\gamma^\mu(1-\gamma_5)s\overline{\nu}\gamma_\mu(1-\gamma_5)\nu \equiv c_L^{SM}\mathcal{O}_L \qquad (2.14)$$

obtained from Z^0 penguin and box diagrams where the dominant contribution comes from the top quark intermediate state. In equation 2.14 G_F is the Fermi constant, α is the fine structure coupling constant (at the Z^0 scale), θ_W is the Weinberg weak mixing angle and V_{ij} are CKM matrix elements; $x_t = (m_{\text{top}}/M_W)^2$. $\mathcal{O}_L$ represents the left–left four–fermion operator,

$$\mathcal{O}_L \equiv \bar{b}\gamma^\mu(1-\gamma^5)s\overline{\nu}\gamma_\mu(1-\gamma_5)\nu. \qquad (2.15)$$

The $\mathcal{O}(\alpha_s)$ contribution deriving from two-loop diagrams is taken into account in the

function X:

$$X(x) = X_0(x) + \frac{\alpha_s}{4\pi} X_1(x), \tag{2.16}$$

where [13],

$$X_0(x) = \frac{x}{8}\left[\frac{x+2}{x-1} + \frac{3x-6}{x-1}^2 \ln x\right]. \tag{2.17}$$

and [14, 15]

$$\begin{aligned} X_1(x) &= \frac{4x^3 - 5x^2 - 23x}{3(x-1)^2} - \frac{x^4 + x^3 - 11x^2 + x}{(x-1)^3} \ln x \\ &+ \frac{x^4 + x^3 - 4x^2 - 8x}{2(x-1)^3} \ln^2 x + \frac{x^3 - 4x}{(x-1)^2} L_2(1-x) \\ &+ 8x \frac{\partial X_0(x)}{\partial x} \ln x_\mu \end{aligned} \tag{2.18}$$

where $L_2(1-x) = \int_1^x dt \frac{\ln t}{1-t}$, and $x_\mu = \frac{\mu^2}{M_W^2}$, with $\mu = \mathcal{O}(m_{\rm top})$. Such a correction (the second term in equation 2.16), using $m_{\rm top} = 175 \pm 9$ GeV/c^2 and $\alpha_s(m_b) = 0.23$, is around 3%.

The presence of a single operator governing the $b \to s\nu\overline{\nu}$ transition is a welcomed feature, since, within the Standard Model, the theoretical uncertainty is only related to the value of one Wilson coefficient c_L^{SM}. In the case of $b \to s\ell^+\ell^-$ for example, the effective Hamiltonian consists of several terms and the uncertainty of a set of coefficients appearing in interfering terms must be accounted for. Moreover, possible new physics effects contributing to $b \to s\nu\overline{\nu}$ can only modify the Standard Model value of the coefficient, c_L, or introduce a new right–right operator,

$$\mathcal{H}_{\rm eff} \equiv c_L \mathcal{O}_L + c_R \mathcal{O}_R, \tag{2.19}$$

($\mathcal{O}_R \equiv \overline{b}\gamma^\mu(1+\gamma_5)s\overline{\nu}\gamma_\mu(1+\gamma_5)\nu$), with c_R only receiving contributions from phenomena beyond the Standard Model. Beyond the Standard Model contributions to the

$b \to s\nu\overline{\nu}$ process have been discussed in detail in the literature [16–35]. It is interesting to note "new", heavy virtual particles mediating the loops in the $b \to s\nu\overline{\nu}$ process should also manifest themselves in processes such as $b \to s\ell^+\ell^-$ and $b \to s\gamma$. Since these latter processes have already been measured [11,36] there must be something different about $b \to s\nu\overline{\nu}$ such that it remains interesting to study experimentally. The neutrinos in the final state make us sensitive to the coupling to third generation leptons through the process $b \to s\nu_\tau\overline{\nu}_\tau$. The analogous reaction with charged leptons, $b \to s\tau^+\tau^-$, is experimentally extremely challenging (and has thus far not been attempted). Hence the $b \to s\nu\overline{\nu}$ process is sensitive to potential new physics where couplings to the third generation could be significantly enhanced [19,30]. Furthermore, since two of the three final state particles are unobserved (the neutrinos) there is sensitivity to other decays where invisible final state particles are present in the $b \to s$ decay [37,38].

The inclusive rate for the decay $b \to s\nu\overline{\nu}$, summed over the three neutrino flavours, has been estimated to be $(4.1^{+0.8}_{-1.0}) \times 10^{-5}$ [39]. The current best limit on the inclusive rate comes from a search by the ALEPH collaboration [40] in which they determine $\mathcal{B}(b \to s\nu\overline{\nu}) < 6.4 \times 10^{-4}$ at the 90% confidence level. The process $b \to d\nu\overline{\nu}$ proceeds via a similar mechanism, but is suppressed relative to $b \to s\nu\overline{\nu}$ due to the relative sizes of the V_{td} and V_{ts} matrix elements.

Unfortunately, experimental searches for inclusive $b \to q\nu\overline{\nu}$ processes (where $q = d, s$) are extremely difficult in a B-factory environment due to the presence of two unobserved neutrinos which limit the availability of kinematic constraints which can be exploited in order to suppress other B decay backgrounds. Instead, we choose to search for specific exclusive states which proceed via $b \to q\nu\overline{\nu}$ processes. This thesis presents search for two exclusive states: $B^+ \to K^+\nu\overline{\nu}$ and $B^+ \to \pi^+\nu\overline{\nu}$. The

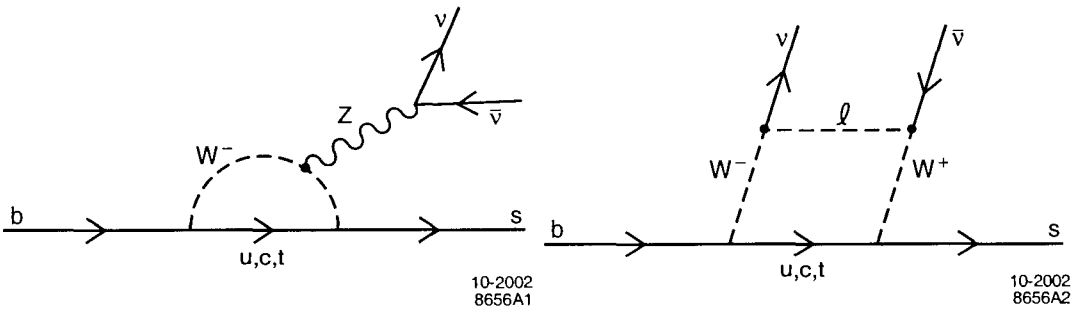

Figure 2.4: Electroweak penguin (left) and box (right) Feynman diagrams for the process $b \to s\nu\overline{\nu}$ predicted by the Standard Model. In both cases the amplitudes are expected to be dominated by the heavy t quark contribution.

theoretical predictions for the rates of these exclusive processes are somewhat less precise than the inclusive rate. For example, the decay rate for $B^+ \to K^+\nu\overline{\nu}$ has been estimated to be $\mathcal{B}(B^+ \to K^+\nu\overline{\nu}\,) = (3.8^{+1.2}_{-0.6}) \times 10^{-6}$ [19, 20]. To date, the only limit on the exclusive rate, $B^+ \to K^+\nu\overline{\nu}$, was published by the CLEO experiment [41] with a 90% confidence limit of $\mathcal{B}(B^+ \to K^+\nu\overline{\nu}\,) \leq 2.4 \times 10^{-4}$, approximately two orders of magnitude above the predicted rate.

There are currently no published experimental limits on the exclusive $B^+ \to \pi^+\nu\overline{\nu}$ reaction. However, theoretical estimates predict that it is suppressed relative to $B^+ \to K^+\nu\overline{\nu}$ by the factor $\mid V_{td}/V_{ts} \mid^2$ (which is $\approx$30). Hence, although both reactions are searched for, the thesis will focus mainly on the $B^+ \to K^+\nu\overline{\nu}$ channel.

Chapter 3

The Experimental Environment

3.1 Introduction

The design of the *BABAR* detector [43] at the PEP-II[1] B factory is optimized for CP violation studies, but it is also well suited to searches for rare B decays. The PEP-II B factory is an asymmetric e^+e^- collider designed to operate at a centre-of-mass energy of 10.58 GeV, the mass of the $\Upsilon(4S)$ resonance.[2] In PEP-II, the 9.0 GeV electron beam collides head-on with the 3.1 GeV positron beam resulting in a Lorentz boost to the $\Upsilon(4S)$ resonance of $\beta\gamma$=0.56. This boost makes it possible to separate the decay vertices of the two B mesons. This allows us to determine their relative decay times Δt, and thus to measure the time dependence of their decay rates, since, without the boost, this distance would be too small to be measured by any vertex tracker. The other crucial characteristic of the PEP-II B factory is the high luminosity (the design luminosity of $3\times10^{33}\text{cm}^{-2}\text{s}^{-1}$ has already been eclipsed). This permits the study of very small branching ratios, which is an inherently common characteristic of rare B decays. The need to fully reconstruct final states places special requirements on the

[1]PEP is an acronym for Positron Electron Project

[2]The $\Upsilon(4S)$ resonance decays entirely to pairs of B mesons, $B\overline{B}$.

detector. The apparatus must have excellent reconstruction efficiency for charged particles and very good momentum resolution to separate small signals from background. Time dependent CP violation requires good vertex resolution in directions both transverse and longitudinal to the beam direction. In order to know the flavour of the B, and to study semileptonic decays, efficient electron and muon identification is required, with low hadron misidentification probabilities. An efficient and accurate identification of hadrons over a wide momentum range is critical, not only for the reconstruction of exclusive states, but also for the study and reconstruction of inclusive kinematic quantities like invariant mass distributions.

Figure 3.1 shows a longitudinal cross-section through the centre of the *BABAR* detector and figure 3.2 shows an end view of the detector.

3.2 PEP-II and the Interaction Region (IR)

PEP-II is an e^+e^- storage ring. The High Energy Ring (HER) stores 9 GeV electrons and the Low Energy Ring (LER) stores 3.1 GeV positrons. Thus PEP-II operates at a centre-of-mass energy of 10.58 GeV, the mass of the $\Upsilon(4S)$ resonance, which is moving with respect to the laboratory frame. The cross-section for the production of fermion pairs at the $\Upsilon(4S)$ mass is shown in Table. 3.1. Approximately 12% of the data are taken 40 MeV below the peak of the resonance, and hence below $B\overline{B}$ threshold, to provide a sample of non-resonant background called continuum, $e^+e^- \rightarrow q\overline{q}$, where $q = u, d, s, c$.

The asymmetric energies produce a boost of $\beta\gamma = 0.56$ in the laboratory frame for the resulting B mesons. As a consequence, the decay points of the B mesons produced from the decay of the $\Upsilon(4S)$ resonance are separated by an average of approximately 250 μm along the beam axis, taken as the z axis in the *BABAR* coordinate

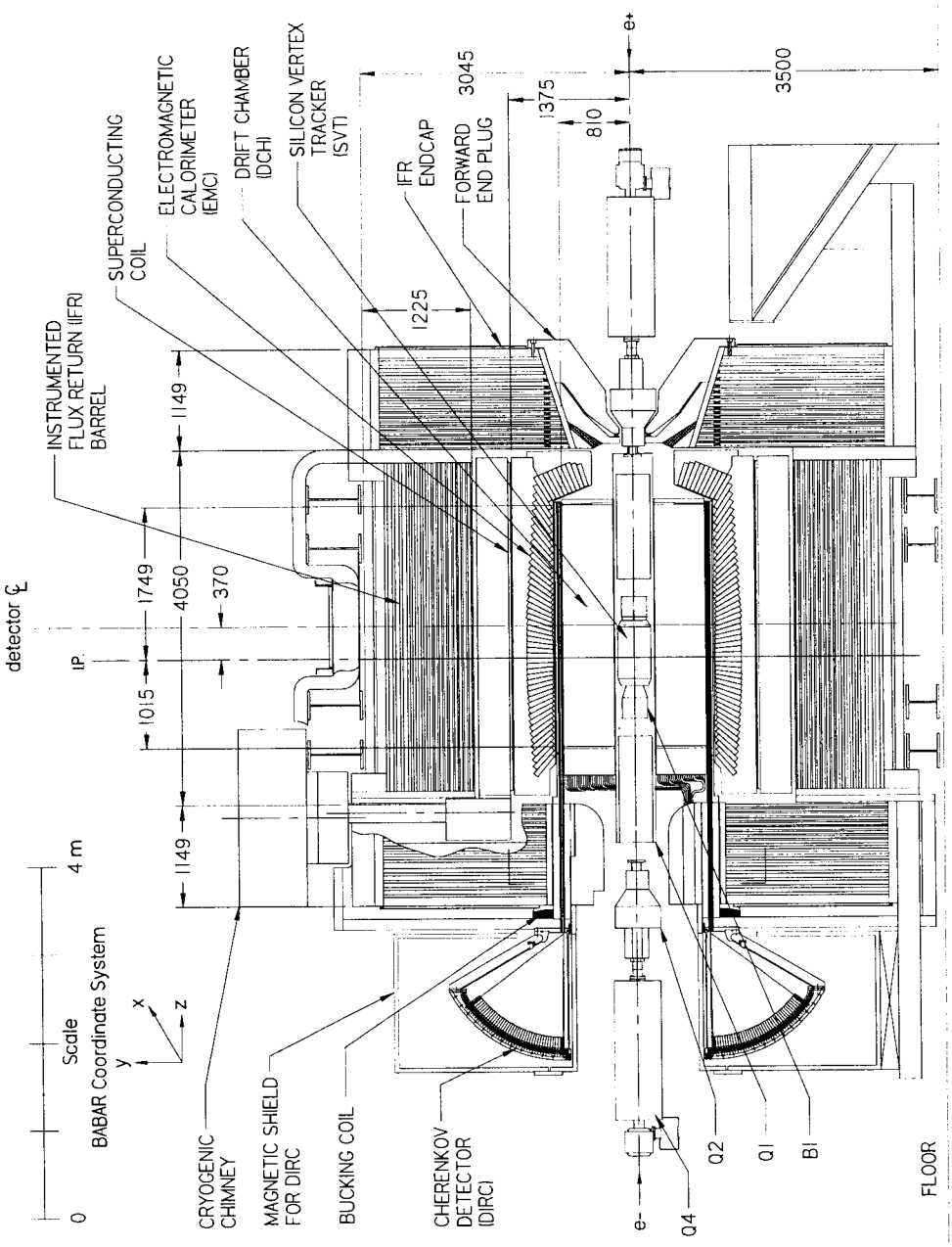

Figure 3.1: Longitudinal view of the *BABAR* detector.

system. Selecting the boost for an optimal physics performance requires balancing two conflicting effects: a) The average B decay vertex separation in z is related to

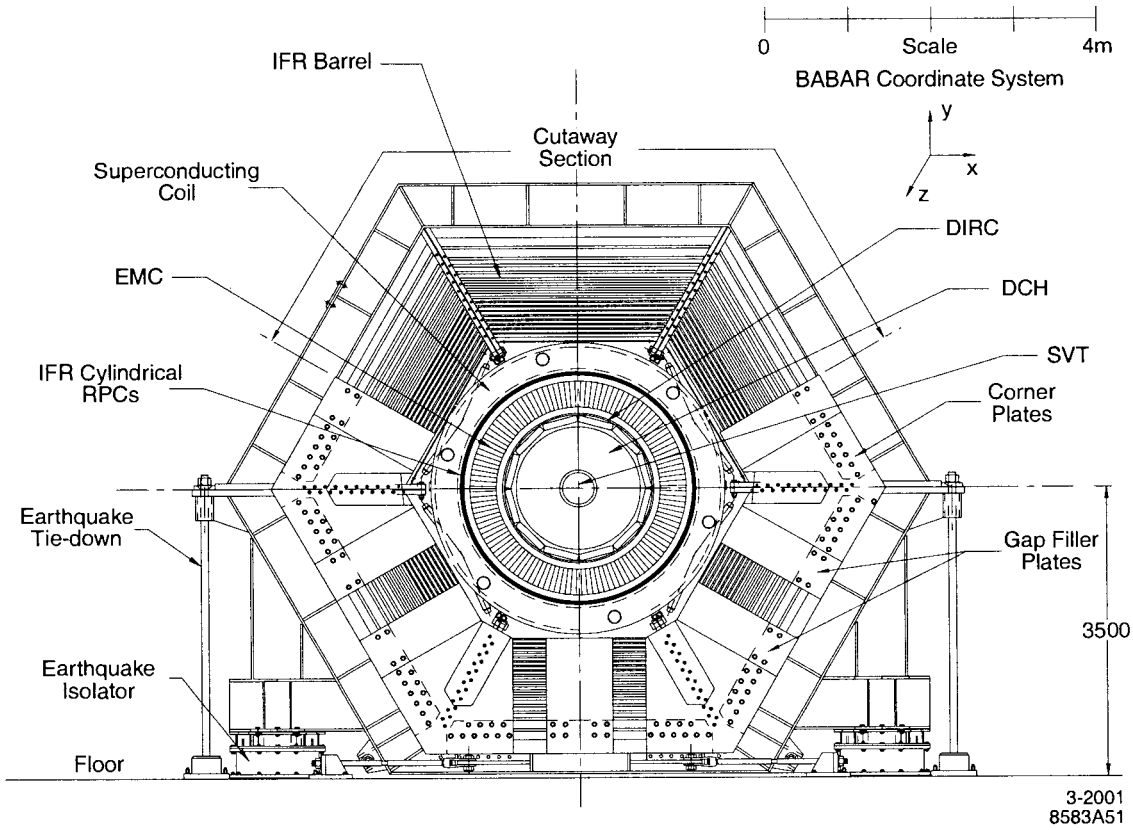

Figure 3.2: An end view of the *BABAR* detector.

$\gamma\beta c\tau$, where τ is the lifetime of the B. Thus increasing the boost would result in an increase in the separation of the B decay vertex making it easier to resolve the two decay vertices. b) However, if the boost is too great the tracks will all be boosted in the forward direction thereby worsening the z resolution. Also, choosing too large a boost, would degrade the physics performance by allowing too many particles to escape undetected down the beam pipe.

A schematic representation of the acceleration and the storage system is shown in

Table 3.1: Production cross-sections at the $\Upsilon(4S)$ resonance.

$e^+e^- \rightarrow$	Cross-section (nb)
$b\bar{b}$	1.05
$c\bar{c}$	1.30
$s\bar{s}$	0.35
$u\bar{u}$	1.39
$d\bar{d}$	0.35
$\tau^+\tau^-$	0.94
$\mu^+\mu^-$	1.16
e^+e^-	~ 40

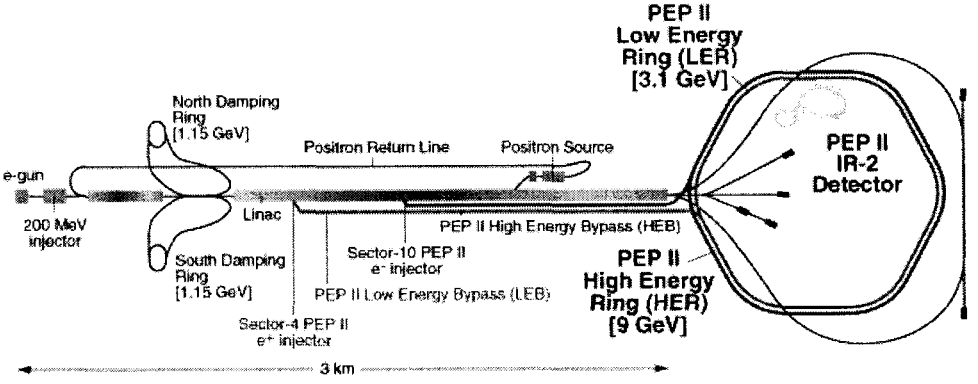

Figure 3.3: A schematic representation of the acceleration and storage system at PEP-II.

Fig. 3.3. An electron gun is used to create two electron bunches that are accelerated to approximately 1 GeV before entering one of the damping rings, whose purpose is to reduce the dispersion in the beams. After that, those electrons are accelerated in the Linac. The other bunch is diverted to collide with a tungsten target to create a positron beam, which in turn passes through the damping ring and is accelerated into the Linac.

On reaching their respective design energies at the end of the Linac, the electron

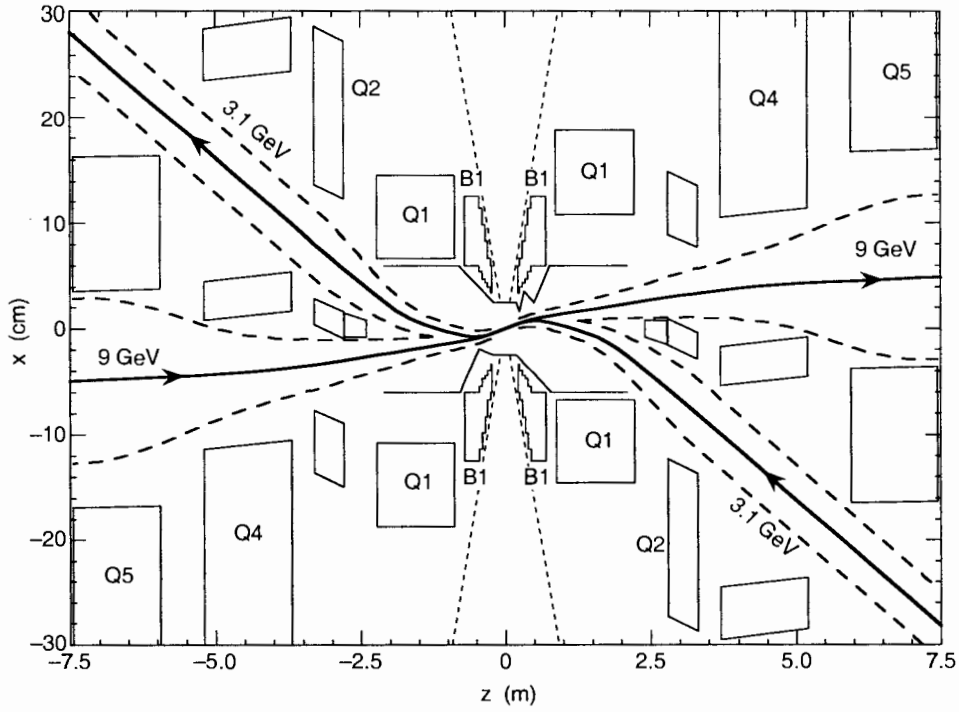

Figure 3.4: A plan view of the interaction region. The x scale is exaggerated. The beams collide head-on and are separated magnetically by the B1 dipole magnets. The focusing of the beams is achieved by using the quadrupole magnets, Q1, Q2, Q4 and Q5. The dashed lines indicate the beam stay-clear region and the detector acceptance cutoff at 300 mrad.

and positron beams are fed into the PEP-II storage rings. It is here that they collide at the interaction region as shown in Fig. 3.4. A primary impediment to achieving currents of the required magnitude are beam-beam interference and related beam instabilities. After collision at the interaction point (IP) the beams are separated by the dipole magnet B1, located at ± 21 cm on either side of the IP, the two beams are separated within 62 cm of the IP, thus avoiding spurious collisions between out of phase bunches. To achieve this the B1 magnets had to be located entirely within the *BABAR* detector volume. The strong focusing of the beam is achieved by using an array of quadrupole magnets. The innermost focusing magnet (Q1) is common to

both beams and partially enters the detector volume. The support tube of the Q1 magnets runs through the centre of the detector between the drift chamber and the silicon vertex tracker. Q2 is used to focus only the LER whereas Q4 and Q5 are used only for the HER. Both Q1 and B1 are permanent magnets while Q2, Q4 and Q5 are standard iron electromagnets. The IP is surrounded by a water-cooled beryllium pipe with an outer radius of 2.8 cm, presenting about 1.08% of a radiation length to particles at normal incidence.

The impressive luminosities are achieved by using high beam currents, a multi-bunch mode and strong focusing of the beams. Within four years of operation PEP-II has not only achieved its design luminosity of $3.3 \times 10^{33}\,\mathrm{cm}^{-2}\mathrm{s}^{-1}$ but, at time of writing has surpassed it by about a factor of 2.[3]

The high luminosity of PEP-II has important implications in terms of acceptable background levels for the proper functioning of the detector. Background sources include synchrotron radiation, interactions between the beam and the residual gas in the rings, and electromagnetic showers produced in beam-beam collisions. Bremsstrahlung and Coulomb scattering of the beam particles off the residual gas in the rings dominate the Level 1 trigger rate, the instantaneous silicon vertex detector dose rates, and the total drift chamber current. Energy-degraded beam particles resulting from such interactions are bent by the separation dipole magnets horizontally into the beam pipe, resulting in occupancy peaks for almost all of the *BABAR* subdetectors in the horizontal plane. The rate of this background is proportional to the product of the beam currents and the gas pressure in the rings. At higher luminosities the background from radiative Bhabha scattering is expected to be crucial.

[3]The peak luminosity achieved is $7.0 \times 10^{33}\,\mathrm{cm}^{-2}\mathrm{s}^{-1}$.

3.3 Detector Overview

A layout of the *BABAR* detector is shown in figure 3.2. In what follows, the relevant subsections of the apparatus will be described in more detail.

Trajectories of charged particles are measured in the silicon vertex tracker which is surrounded by a cylindrical wire chamber, the drift chamber. A novel Cherenkov detector used for charged particle identification surrounds the drift chamber. The electromagetic showers of electrons and photons are detected by the CsI crystals of the electromagnetic calorimeter which is located just inside the solenoidal coil of the super-conducting magnet. Muons and neutral hadrons are detected by arrays of resistive plate chambers that are inserted in the gaps of the iron flux return of the magnet. The detector acceptance is $17° < \theta_{\rm lab} < 150°$ in the laboratory frame ($-0.95 < \cos\theta_{\rm CM} < 0.87$ in the centre of mass frame) where θ is the polar angle. Through the thesis θ will be assumed to mean $\theta_{\rm lab}$ unless explicitly stated otherwise.

3.4 The Silicon Vertex Tracker

The silicon vertex tracker(SVT) [44] was designed to provide precise reconstruction of charged particle trajectories and decay vertices near the interaction region. Good vertexing is crucial for *CP* violation studies, it is imperative to measure the mean spatial position of each B meson decay vertex along the z axis with better than 80 μm resolution. As many of the decay products of the B have a low transverse momentum (p_T) the SVT must also provide track reconstruction for particles with p_T less than 120 MeV/c, as these tracks do not reach the drift chamber. Reconstruction of low momentum tracks is important in order to fully constrain the decay products of the B's. Furthermore, as it is the detector closest to the beams, it must withstand

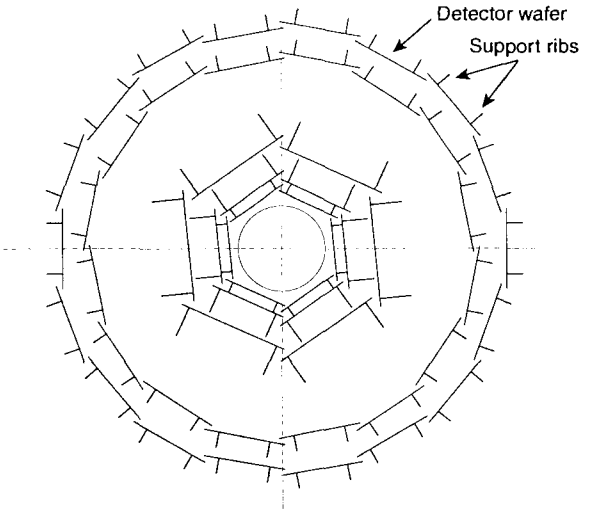

Figure 3.5: SVT layout in x–y view. Only barrel wafers are shown. The central cylinder corresponds to the beam pipe whose outer radius is 2.8 cm.

an integrated dose of 2 Mrad of ionizing radiation. A radiation monitoring system capable of aborting the beam is needed to ensure that the device is not exposed to radiation that would exceed the design tolerance within the anticipated lifetime of the experiment. As the SVT is inaccessible during normal running, robustness and reliability are essential qualities of its design.

3.4.1 Silicon Vertex Tracker Overview

The SVT is a five-layer double–sided silicon micro–strip detector. Figure 3.5 shows the layout of the detector in the x–y plane and figure 3.6 shows an r–z view of the upper half. The acceptance of the device is $17.2° < \theta < 150°$ in the laboratory frame. To reduce the effect of multiple scattering on the determination of the track impact parameters, it is important to minimize the amount of material between the IP and the first measuring plane and to place the first layer of the SVT as close as possible

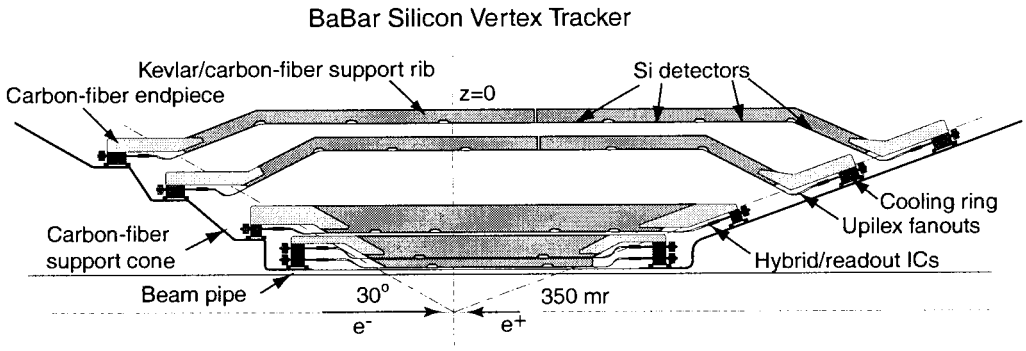

Figure 3.6: SVT layout: cross-sectional view of the upper half. The first layer radius is 3.3 cm, and the maximum fifth layer radius is 14.4 cm. The outer layers have an arch structure to minimize the amount of silicon needed for the solid angle coverage and to reduce large incidence angles.

to the beam pipe.

The first three layers are arranged in a barrel structure, divided into sextants. Their primary goal is to provide precision angular measurements of the azimuthal angle, ϕ, and the polar angle, θ, and impact parameter measurements. The outer layers are required for pattern recognition and stand-alone tracking. Within each layer, silicon wafers are combined into modules. There are 6 modules in the first three layers. The modules have 4 wafers each in the first two layers and 6 wafers each in the third layer. Layers 4 and 5 have 16 and 18 modules with 7 and 8 wafers per module, respectively. The total number of wafers is 340. This design was chosen to minimize the amount of silica required to cover the solid angle, without compromising the efficiency. Each module is divided into two halves, forward and backward. To measure the z coordinate there are strips on the inner sides of the detector that run perpendicular to the beam direction while the strips on the outer sides run orthogonal to the z strips in order to measure the ϕ coordinate.

As the SVT is the closest sub-detector to the interaction point, the radiation doses are constantly monitored with 12 silicon photo-diodes, located at a radius of 3 cm from the beam pipe. Even though the instantaneous dose can be very high during beam injection, the subsystems lifetime is determined not by the instantaneous rates, but by the total integrated radiation dose.

3.4.2 Performance

The SVT hit resolution can be calculated by comparing the number of associated hits to the number of tracks crossing the active area. The combined hardware and software efficiency as a function of the track incident angle, for each of the five layers is about 97%. The measured charged particle energy loss as it passes through the

silicon is used for particle identification and achieves a 2σ separation between kaons and pions up to a momentum of 500 MeV/c and between kaons and protons beyond 1 GeV/c.

The SVT has been operating efficiently since its installation in the *BABAR* experiment and has satisfied the original goal for vertex and low transverse momentum hit resolution.

3.5 The Drift Chamber

The Drift Chamber(DCH) [45] is arguably the most important subsystem of the experiment. It is the main tracking device of *BABAR* and provides trajectory information for charged particles with momenta greater than approximately 100 MeV/c. It complements the SVT in the measurements of the impact parameter and can improve the SVT's momentum measurement of charged particles by providing additional information. The DCH is used for particle identification through the measurement of ionisation loss (dE/dx) and it is the central component of the charged particle trigger (L1).

3.5.1 Drift Chamber Overview

A longitudinal section of the DCH is shown in Fig. 3.7. The apparatus consists of 280 cm long concentric cylinders with end-plates made of aluminum, strung with low-mass aluminum wires and filled with a 80:20 mixture of helium:isobutane. A low density helium-based gas mixture is used to reduce multiple scattering. It achieves a dE/dx resolution of approximately 7.5%.

The inner radius is at 23.6 cm and the outer radius is at 80.9 cm, with respect to the interaction point. The forward-backward coverage is $-1.11 < z < 1.66$ m due

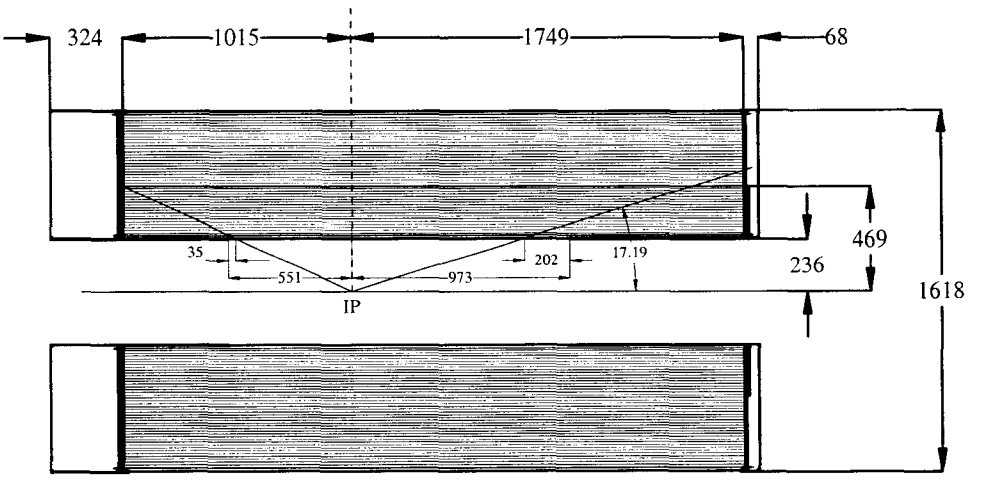

Figure 3.7: Longitudinal cross-section of the drift chamber with principle dimensions in mm.

to the $\Upsilon(4S)$ boost along the z axis. In order to facilitate track matching between the SVT and the DCH and reduce photon conversion, the DCH cylinder walls were made as thin as possible. The inner cylinder is 1 mm of beryllium or 0.28% radiation length and the outer cylinder consists of 2 layers made of carbon fibre on a nomex core of 1.5% of radiation length. The total thickness of the DCH is approximately 1.08% of radiation length at normal incidence.

The wires are organized into 40 layers of small hexagonal cells, subdivided into 10 super-layers in an alternating axial (A) and stereo (U,V) pattern, as shown in Fig. 3.8. The stereo angle increases radially from ± 45 mrad to ± 76 mrad. The stereo measurements are used for extracting the longitudinal (z) position information. There are a total of 7,104 small drift cells typically 1.2 x 1.9 cm^2 in size. Each cell contains a 20 μm gold-plated tungsten-rhenium sense wire, surrounded by a grid of gold-plated aluminum field wires which are 120 μm and 80 μm thick. Near the sense wire, isochrones are circular; however, they become distorted close to the field wires. A potential of 1900$\rightarrow$1960 V is applied to the sense wires, while the field wires are

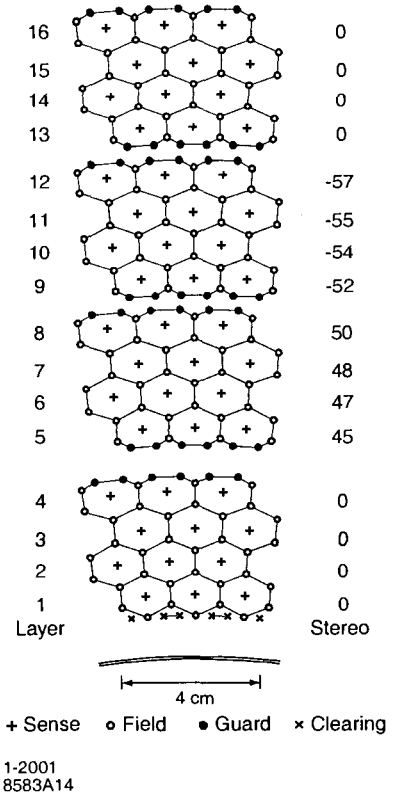

Figure 3.8: Schematic layout of the drift chamber layer arrangement. The layers are arranged into 10 super–layers comprised of 4 layers each. Stereo angles are quoted in mrad.

grounded. This potential difference gives an avalanche gain of about 5×10^4. The cells are designed to provide an average intrinsic spatial resolution better than 40 μm.

The DCH meets the design expectations. It contributes primarily to the measurement of the momentum transverse to the beam, p_T, while the angle and position measurement near the interaction point is dominated by the silicon vertex tracker. The data is well represented by the following formula:

$$\frac{\sigma_{p_T}}{p_T} = (0.13 \pm 0.01)\%\ p_T(\text{GeV}) + (0.45 \pm 0.03)\% \tag{3.1}$$

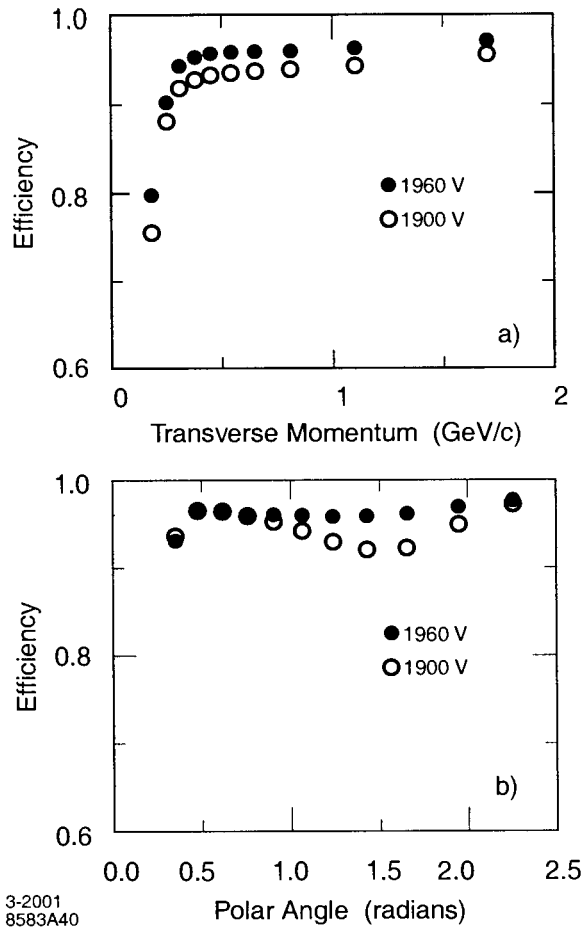

Figure 3.9: The track reconstruction efficiency in the DCH at operating voltages of 1900 V and 1960 V as a function of a) transverse momentum and b) polar angle. The measurement at the DCH voltage of 1900 V(open circle) and 1960 V (solid circle) are shown.

3.5.2 Tracking Performance

Charged tracks are defined by five parameters (d_0, ϕ_0, ω, z_0, and $\tan\lambda$). These parameters are measured at the point of closest approach to the axis, d_0 and z_0 are the distance of this point from the origin of the coordinate system in the x–y plane and along the z axis, λ is the dip angle relative to the transverse plane, $\omega = {p_T}^{-1}$ is its curvature, ϕ_0 is the azimuth of the track. Track reconstruction in *BABAR*

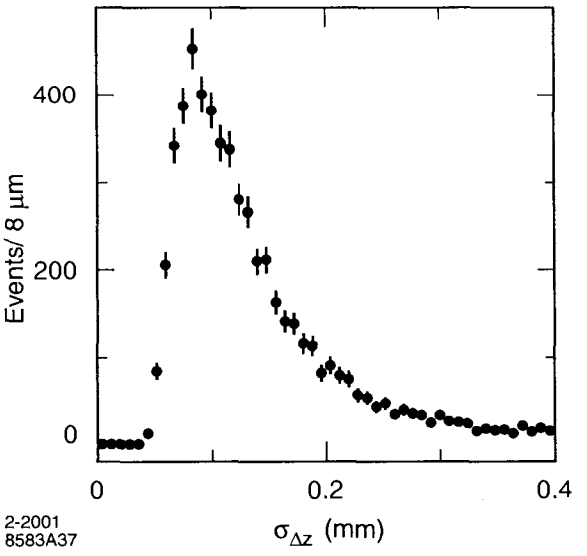

Figure 3.10: Estimated error in the difference Δz between the B^0 meson decay vertices for a sample of events in which one B^0 is fully reconstructed.

can be performed independently by the SVT and the DCH, thus making it possible to determine the absolute tracking efficiency of the DCH to the number of tracks detected by the SVT, provided that corrections for fake tracks found in the SVT and scattering of the tracks from the support tube are applied. A small additional correction needs to be applied to account for the fact that the two tracking subsystems are linked together at one stage by a common track finding algorithm. This method of estimating tracking efficiencies is applied to both the Monte Carlo and data sample, Fig. 3.9 shows the tracking efficiency as a function of transverse momentum and polar angle for a sample of multi-hadron events. During the years 1999-2000 the data were taken with two different voltage settings of 1900 V and 1960 V. The tracking efficiency at 1960 V was measured to be $(98 \pm 1)\%$ for tracks with $p_T > 200$ MeV/c and polar angle $\theta > 500$ mrad; at 1900 V, the efficiency is slightly lower, by about 5%, for tracks at normal incidence. The resolutions of the five track parameters are monitored using Bhabhas and dimuon events. The resolutions in the coordinates, d_0

and z_0 are dependent on the transverse momentum, which are obtained using multi-hadron events and are about 25 μm and 40 μm respectively at p_T of 3 GeV/c. From 2001 until the present time the DCH has operated at 1930 V.

The estimated error in the measurement of the difference along the z axis between the decay vertices of the two neutral B mesons where one B is fully reconstructed while the other is partially reconstructed is shown in Fig. 3.10. The r.m.s. width of 190 μm is dominated by the reconstruction of the partially reconstructed B^0 (170 μm) while the rms for the resolution for the fully reconstructed B^0 is 70 μm.

3.5.3 Bunch T0

With the PEP-II beam crossing rate of 4.2 ns it is impossible to tell, in real time, which event arose from which beam crossing. Therefore, we use information from the reconstruction to determine this. Using track segments found independently in each DCH superlayer it is possible to relate the ΔT0 to the time of the interaction producing the particle. The time-of-flight of the particle must be accounted for in this procedure. The resulting resolution on the collision time is on the order of $\sim$1 ns for an typical event.

3.6 The Detection of Internally Reflected Cherenkov Light

Good particle identification is crucial for measurements that depend on the need to identify the flavour of the B meson or to identify kaons and/or pions with high purity and efficiency. K/π separation up to momenta of 0.7 GeV/c is obtained by measuring the ionisation energy loss, dE/dx, in the SVT and/or the DCH. The detector of internally reflected Cherenkov light(DIRC) [46] provides the particle identification

for higher momentum tracks and hence is crucial to many analyses.

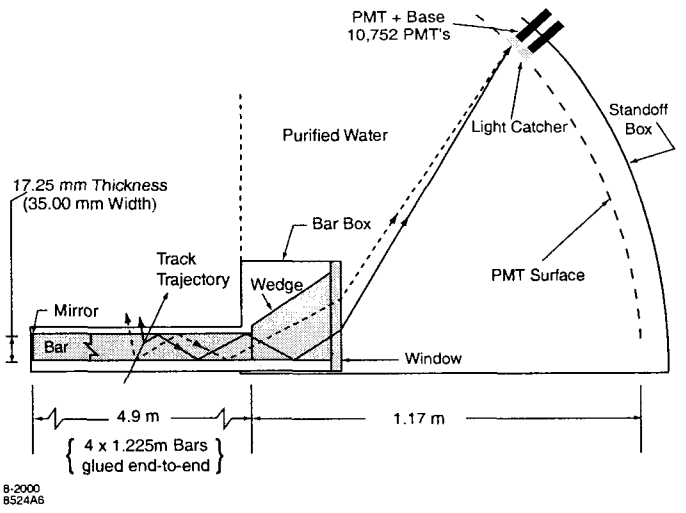

Figure 3.11: Schematic of the DIRC fused silica radiator bar and imaging region.

3.6.1 DIRC Overview

A schematic of the DIRC geometry to illustrate the principles of light production, transportation, and imaging is shown in figure 3.11. The DIRC uses thin, long rectangular bars made of synthetic fused silica (quartz) [47] both as Cherenkov radiators and light guides (with a refractive index $n \approx 1.47$). The 144 bars are arranged in a 12-sided polygonal barrel with a radius of about 84 cm around the beam axis. The DIRC bars extend 178 cm forward from the interaction point of *BABAR* covering 87% of the polar solid angle in the centre-of-mass frame. Each set of 12 bars are housed in a bar box surrounded by nitrogen (refractive index $n \approx 1$). The Cherenkov angle is given by the relation

$$\cos\theta_c = 1/n\beta. \tag{3.2}$$

where $\beta = v/c$, v = speed of the particle, c = speed of light. Since the refractive index of the radiator bar is larger than $\sqrt{2}$, a fraction of the Cherenkov photons produced

by a relativistic charged particle traversing the quartz bar will undergo total internal reflection, regardless of the incidence angle of the tracks, and propagate along the length of the bar. Only one end is instrumented, so a mirror (reflectivity $\approx 92\%$) is placed perpendicular to the bar axis on the other end. Photons exiting the bar in the downward direction, or with large angles in the radial direction, are partly recovered into the instrumented area by a prism at the readout end. The prism reduces the required photon-sensitive area by more than a factor of two, while introducing little complexity to the image reconstruction.

A thin (9 mm) quartz window separates the prism from the standoff box (SOB), a water tank filled with 6000 litres of purified water (index $n \approx 1.33$) built in a toroidal shape. The backplane of the SOB is divided into 12 sectors, each equipped with 896 conventional photo-tubes of approximately 25% detection efficiency at 400 nm wavelength (spectral range: 250 nm – 650 nm) pointing to the exit of a corresponding bar box.

3.6.2 Performance

The overall single photon resolution is about 9.6 mrad, dominated by the track reconstruction and the chromatic aberrations. The resolution on a track scales as $\sigma_\gamma/\sqrt{N_\gamma}$, where σ_γ is the resolution of a single photon and N_γ is the number of detected photons. N_γ is about 30 for normal incidence tracks. The average track Cherenkov angle resolution, measured in dimuon events, turns out to be 2.5 mrad, which leads to a approximately 4σ separation between kaons and pions at 3.3 GeV/c momenta.

3.7 The Electromagnetic Calorimeter

The *BABAR* electromagnetic calorimeter (EMC) [48] is designed to measure the energy in the electromagnetic showers with excellent efficiency, energy and angular resolution over the energy range of 20 MeV to 9 GeV. This capability allows for reconstruction of π^0 and η mesons and for the separation of photons, electrons and positrons from charged hadrons. The active elements consist of thallium-doped caesium iodide (CsI(Tl)) crystals.

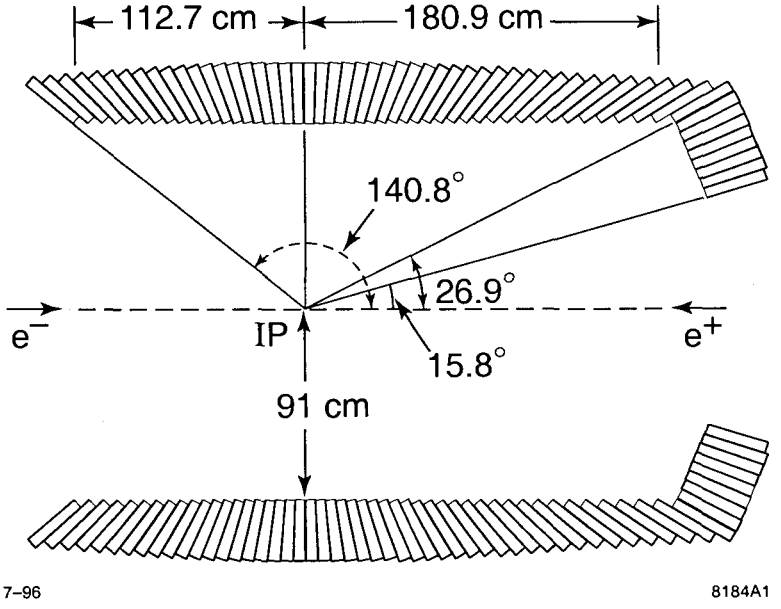

Figure 3.12: Layout of the EMC showing the barrel and the forward end-cap region.

3.7.1 Electromagnetic Calorimeter Overview

The EMC is presented in figure 3.12 and consists of a cylindrical barrel and a conical forward end-cap. The range of coverage in the centre-of-mass solid angle is $-0.916 \leq \cos\theta \leq 0.895$, the backward-forward asymmetry reflecting the boost of the collision in the laboratory frame. The barrel section covers the centre-of-mass solid angle of

$-0.916 \leq \cos\theta \leq 0.715$ and has an inner radius of 91 cm. It contains 5760 barrel crystals, arranged in 48 polar angle rows, each row has 120 identical crystals around the azimuthal direction. Each crystal is held in a 250 μm thick carbon fiber composite compartment, that are grouped into 2804 modules of 3 crystals wide and 7 crystals long. The forward end-cap is a conic section and covers a centre-of-mass solid angle of $0.718 \leq \cos\theta \leq 0.895$. It contains 820 end-cap crystals grouped into 20 modules of 41 crystals each.

The crystals have a trapezoidal shape with typical dimensions of 47×47 mm^2 at the front face and 60×60 mm^2 and ranges from 17.5 to 16 radiation length thickness in the forward and the end-cap regions respectively. The emission of the scintillation light produced in the crystals permits the use of silicon photo-diodes which are attached to the back faces of the crystals. The signal is amplified and sent to the data acquisition board and to the Level 1 trigger system. The average light yield per crystal is 7300 photo-electrons/ MeV varying between 5000 and 10000 over an electronic noise of the order of 900 photo-electrons.

3.7.2 Performance

The calorimeter has an efficiency of more that 96% for detecting photons, above a minimum measurable energy of about 20 MeV. The limit is largely determined by beam and event related backgrounds and the amount of material in front of the calorimeter. At low energy, the energy resolution of the EMC is measured periodically with a radioactive source. At high energy the energy resolution is measured from Bhabha scattering events and is parameterized by :

$$\frac{\sigma_E}{E} = \frac{(2.32 \pm 0.30)\%}{E(\text{ GeV})^{\frac{1}{4}}} \oplus (1.85 \pm 0.12)\% \tag{3.3}$$

where E is the photon energy in GeV. At lower energies the resolution is dominated by fluctuations in photon statistics and by beam generated backgrounds and at higher energies(> 1 GeV) by the non-uniformity in light collection from leakage or absorption in the material between or in front of the crystals. The reconstructed π^0 mass has a

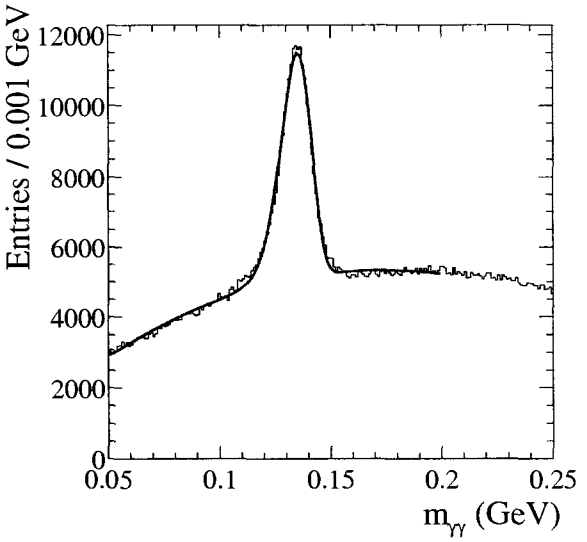

Figure 3.13: Invariant mass of two photons in $B\overline{B}$ events. The energies of the photons and the π^0 are required to be between 30 MeV and 300 MeV. The solid line is the fit to data.

width of 6.9 MeV/c^2 and is shown in Fig. 3.13. The mass resolution is dominated by the energy resolution at lower energies (below 2 GeV). At higher energies, the mass resolution is dominated by the angular resolution. The latter is determined primarily by the transverse crystal size. The angular resolution can be found from analyses of π^0 and η decays. The angular resolution can be parameterized by

$$\sigma_\theta = \frac{3.87 \pm 0.07}{\sqrt{E(\text{ GeV})}} \oplus (0.00 \pm 0.04) \text{ mrad} \tag{3.4}$$

3.8 The Superconducting Solenoid

The *BABAR* solenoid provides a 1.5 T field to permit measurement of the transverse momentum of charged particles. The solenoid is manufactured from superconducting niobium titanium filaments. The filaments are wound into strands of diameter 0.8 mm, 16 of which are then formed into *Rutherford cable* measuring 1.4×6.4 mm. The final conductor consists of Rutherford cable coextruded with pure aluminium stabilizer measuring 4.93×20.0 mm for use in the outer, high current density portion of the solenoid, and 8.49×20.0 mm for the central, lower current density portion. The conductor is then wrapped in an insulating dry wrap fiberglass cloth which is vacuum impregnated with epoxy. The solenoid is indirectly cooled to 4.5 K using a thermo-syphon technique where liquid helium is circulated in channels welded to the solenoid support cylinder and maintains the low temperature.

The solenoid is situated between the EMC and Instrumented Flux Return (see section 3.9 for further details). The main magnet parameters are outlined in more detail in table 3.2. The variation in the magnetic field is less than a few percent, which simplifies charged track reconstruction in the SVT and DCH. The field is large enough to provide sufficient momentum resolution; the 1.5 T field causes a 3 GeV/c particle to bend 3 cm before it reaches the outside of the DCH. The field uniformity is important since the tracks are asummed to move along helices near the origin. Field non–uniformities are accounted for in the track-fitting algorithms but not in the trigger and pattern recognition software.

Table 3.2: The parameters of the *BABAR* magnet.

Parameter	Value
Central Field	1.5 T
Maximum Radial Field	<0.25 T
Mean Solenoidal diameter	3060 mm
Solenoid length	3513 mm
Stored Energy	27 MJ

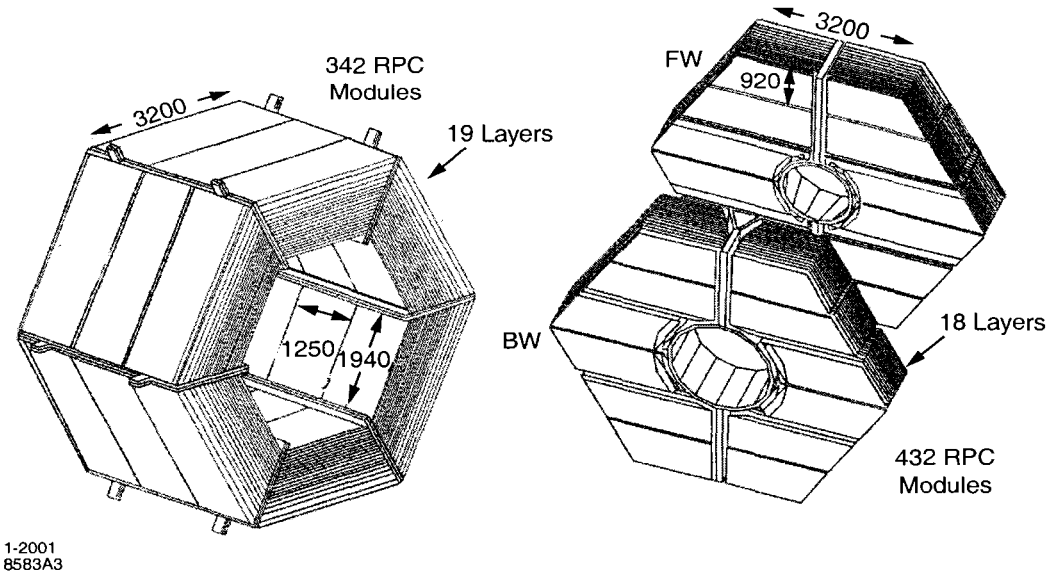

Figure 3.14: The Instrumented Flux Return consists of three sections: the barrel (left), containing 342 RPC modules between 19 layers of steel, and the forward and backward end-caps (right), with a total of 432 RPC modules in 18 layers. 32 more RPCs are placed in the two cylindrical layers (not shown here).

3.9 The Instrumented Flux Return

The Instrumented Flux Return (IFR) was designed to be the primary muon identification system, based on the assumption that they are the only charged particles capable of penetrating so far through the detector. The subsystem was designed to provide high efficiency and good purity muon detection over a wide range of angles and momenta. In addition, the IFR provides detection of long-lived neutral hadrons, primarily K_L^0 and neutrons. They are observed through their interaction with the steel as small clusters of hits. The neutral hadron reconstruction is limited to direction; the calorimetric information alone is too coarse to provide useful input.

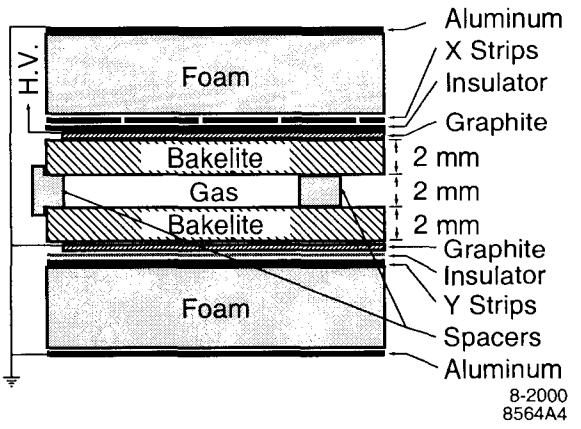

Figure 3.15: Cross section of a planar RPC with the schematics of the High Voltage (HV) connection.

3.9.1 Instrumented Flux Return Overview

The IFR configuration is shown in Fig. 3.14 and consists of three parts: the barrel and the forward and backward end-caps. All of them are subdivided into sextants. Penetration of the IFR varies with momentum, so the device is segmented non-uniformly. Particles can be missed if they deeply penetrate the cracks in the IFR coverage. The active detectors are 806 Resistive Plate Chambers (RPC) [49], located in the gaps between the layers of steel. There are 19 RPC layers in the barrel, and 18 layers in the end-caps. Additionally, there are two layers of cylindrical RPCs between the EMC and the magnet. The thickness of the steel layers ranges from 2 cm in the inner 9 layers to 10 cm in the outermost layers. The total thickness of iron at normal incidence is 65 cm in the barrel region, 60 cm in the endcaps.

RPCs are gas chambers enclosed between Bakelite plates. In both the planar and cylindrical RPCs, the gap between the Bakelite sheets is 2 mm, and the sheets themselves are 2 mm thick. One of the plates is kept at approximately 8 kV, and

the other is grounded, so that an ionizing particle crossing the gas gap will produce a quenched discharge. This ionization induces a pulse which is picked up by aluminum strip electrodes which run in perpendicular directions on the outside of the Bakelite. The Bakelite is chosen for its resistive properties (10^{11-12} Ω–cm) which localize the discharge. The gas used is a mixture of 56.7% argon, 38.8% Freon-134a, and 4.5% isobutane.

3.9.2 Performance

The IFR reconstruction joins hits across layers into two-dimensional clusters in each dimension. Within each sector, clusters in each dimension are then combined into a three-dimensional cluster.

Muon identification in the IFR starts by associating hits in the RPC strips within a certain transverse distance from the extrapolated trajectory of a reconstructed charged track. Selections are based on information such as the quality of the cluster track match and a comparison of the interaction lengths traversed by the track in the detector and the expected number of interaction lengths for a muon of the same momentum and angle. The minimum momentum for muon identification using the IFR is about 600 MeV/c, based on the transverse momentum necessary to enter the detector. Between momenta of 1.5 GeV/c and 3.0 GeV/c, where most of the primary leptons from semileptonic decays of the B meson lie, the IFR achieves nearly 90% efficiency for muon identification with 6–8% pion misidentification.

3.10 The Trigger System

The trigger system is designed with two stages. The Level 1 trigger is performed in hardware using information collected from the front-end electronics. The Level 3

trigger is performed in software on a farm of 32 PC's. Important features of these systems are described in the following subsections.

3.10.1 Level 1 Trigger

The Level 1 trigger system is a hardware-based trigger system. It uses information from three subsystems - DCH, EMC and IFR - to make its decision and hence is broken into three trigger subsystems.

The Drift Chamber Trigger (DCT) uses all 7104 DCH channels to assemble clusters of cell hits into track segments (using the Track Segment Finder hardware, or TSF). The DCT then assembles track segments into full tracks (using the Binary Link Tracker) and checks those tracks against preset transverse momentum thresholds (via the Drift Chamber PT discriminator boards). For tracks originating from the IP, the TSF is 97% efficient. For high momentum tracks ($p_T > 0.8$ GeV/c) the DCT is 94% efficient.

The Electromagnetic Trigger (EMT) divides the EMC crystals into 280 *towers* each containing $7\times40(\theta\times\phi)$ crystals. When the tower energy thresholds cross 20 MeV the bit for that tower is set and sent to the EMT. This occurs every 269 ns. The EMT is 99% efficient at triggering on energy clusters above 180 MeV, the average energy deposited by a minimum ionizing particle at normal incidence. The IFR Trigger (IFT) is used primarily to trigger on $\mu^+\mu^-$ events and cosmic rays.

Information from the DCT, EMT and IFT is assembled and passed to the Global Level Trigger (GLT). The GLT is sent to the Fast Control and Timing System (FCTS) where the final trigger decision is made and the FCTS then informs the subsystems to send their information to the Level 3 farm. The Level 1 system delivers triggers at a rate of 1 kHz. Out of this total rate Bhabha and annihilation physics contributes

130 Hz. Cosmic rays contribute 100 Hz and much of the remaining triggers are due to lost particles interacting with the beam pipe or other components. For $B\overline{B}$ events the trigger is >99.9% efficient. For rare B decay modes with low multiplicity, such as $B^0 \rightarrow \pi^0\pi^0$ or $B^+ \rightarrow K^+\nu\overline{\nu}$, the Level 1 trigger is 99.7% efficient [43].

3.10.2 Level 3 Trigger

The Level 3 trigger is a software-based trigger which performs a full event reconstruction and classification. The trigger is performed in three stages. In the first stage, events are classified according to the trigger information from the FCTS. In the second stage *BABAR* event reconstruction algorithms are applied to the event to find quantities of interest and filters are applied to test whether these quantities satisfy imposed selection criteria. The last stage creates the Level 3 output information, a set of classifications for each event. For a typical run the desired physics events contribute 13% of the total output while the calibration and diagnostic sample contributes 40%.

Chapter 4

Data and Monte Carlo Samples

4.1 Introduction

The *BABAR* detector began taking data in May 1999. Between 1999 and a scheduled shutdown in the summer of 2002 the experiment recorded $81.9\,\text{fb}^{-1}$ of data at the $\Upsilon(4S)$ resonance ("on-peak") and $9.7\,\text{fb}^{-1}$ below $B\overline{B}$ threshold ("off-peak"). Cross-sections for different e^+e^- reactions at the $\Upsilon(4S)$ resonance are given in table 3.1. Taking the off-peak data permits the study of contributions from $e^+e^- \rightarrow f\overline{f}$ where f can be any of the charged leptons or light quarks u, d, s, or c.

In tandem with the data collection, the *BABAR* collaboration generates a large collection of simulated Monte Carlo samples. Typically a ratio of $3:1$ is maintained for on-peak processes and $1:1$ for off-peak events. The work described herein also relies on specifc signal Monte Carlo to study various selection criteria and the efficiency of the overall event selection. We perform comparisons between the data and simulation at all stages of the event selection in order to study how well the data are modeled and to study the levels of background expected in particular parameter spaces.

4.2 The *BABAR* data set

The period from 1999-2000 is referred to as "Run 1", while period from 2001 - summer 2002 is referred to as "Run 2". The analysis presented here uses the full data sets collected in both Runs 1 and 2. At all stages of data taking (including processing and storage) the *BABAR* collaboration maintains data quality by using a set of quality assurance criteria. There are periods during data-taking where the detector encounters problems. In such cases, the data is flagged by the current shift taking team and can be examined at a later time.

If a problem is found to have a occurred throughout a lengthy period of data-taking this can often be dealt with when the data are processed. If no feasible solution is found that data is dispensed with. The Run Quality Manager (RQM) makes a final decision regarding data quality after processing has taken place. Only those samples of the highest quality are used for physics analysis.

A single triggered "event" which is stored to disk is the smallest unit of data. A "run" is that period of time that refers to events collected in a single time period that the *BABAR* data acquisition system (DAQ) was in constant operation. Any run will commonly contain at least 10,000 events and usually lasts no more than two hours. The following criteria must be satisfied for a good run to be selected:

1. The run type is "colliding beams", that is to say that the electron and positron beams are in collision for the duration of the run.

2. All detector subsystems are in a "good" state meaning that no system was suffering problems that prevented data from being taken.

3. The global data quality flag is set as "good"

4. The luminosity recorded is >0

5. The run was successfully processed and reconstructed.

4.3 The *BABAR* Monte Carlo simulation

The simulation of physics processes is performed in a number of stages by the *BABAR* Simulation Production (SP) group. All Monte Carlo simulations (MC) which are to be used for official results must be performed by this group. Specific simulations can be requested by the *BABAR* working groups. The Monte Carlo simulations produced from 2000-2002 for comparison with Run 1 and Run 2 data is referred to as SP4 (Simulation Production 4).

The stages of the Monte Carlo production are described in the following sections.

4.3.1 Event Generation

The first stage of the simulation involves generating four-vectors for the physical processes. This is done by a collection of C^{++} software which has been developed over several years. This software is managed by a single *BABAR* application called `GenFwkInt` (Generators Framework Interface) [51]. Generic $B\overline{B}$ events, for example, are simulated by the routine `EvtGen` (EventGenerator) which is part of the `GenFwkInt` framework package. Other events which are routinely generated are $\mu^+\mu^-$ and Bhabha's. The generator simulates the spread of energies allowed in the PEP-II beam collisions to determine the energy available to the resulting particles. The four-vector generators are detailed in [51].

4.3.2 Simulation of material within the detector volume

Once four-vectors are generated the particles are propagated through a model of the material of the *BABAR* detector. All secondary interactions are performed at this stage along with interactions with the material. The simulation is performed by an application called BOGUS (*BABAR* Object-oriented `GEANT4` based Unified Simulation) which is built on the `GEANT4` simulation toolkit [52].

As particles pass through the active regions of the detector the energy, charge and angular information are used to calculate positions and idealized energy deposits in the detector. Such quantities are referred to as "Ghits". They are stored in persistent containers in an Objectivity database for later use in calculating detector response. While `GEANT4` provides particle transport algorithms, the *BABAR* collaboration has developed its own routines specific to the simulation of that particular detector.

4.3.3 Detector response and backgrounds

At this stage idealized Ghits are retrieved from the database and digitized, that is, transformed into realistic signals which mimic those collected from the detector electronics. Real background events are stored in a database and are mixed with simulated events to more closely reproduce the data. The outcome of this stage is a set of raw objects called "digis" which are stored in a database for use in the reconstruction phase. These functions are performed using the `SimApp` application. After calculating the detector response and mixing in the backgrounds Level 1 and Level 3 trigger conditions are applied to the event.

This stage produces an event containing raw subdetector information and hence is analogous to the real data recorded by the *BABAR* detector. In the final stage of simulation the full event reconstruction algorithm for finding charged particles and

Table 4.1: Data and Monte Carlo samples used for the analyses described in this thesis.

Data set/MC type	Number of events (in millions)	Luminosity [fb^{-1}]	Cross-section [nb]
Run 1 on-peak	111.8	20.7	5.4
Run 2 on-peak	330.5	61.2	5.4
Run 1 off-peak	11.2	2.6	4.3
Run 2 off-peak	30.0	7.0	4.3
$B^+ \to K^+\nu\overline{\nu}$, $B^- \to X$	2.39	62800	3.8×10^{-5}
$B^+ \to \pi^+\nu\overline{\nu}$, $B^- \to X$	0.15	–	–
B^+B^- generic	163.5	311.4	0.54
$B^0\overline{B}^0$ generic	120.2	229.0	0.54
$c\overline{c}$	112.6	86.6	1.30
$u\overline{u}, d\overline{d}, s\overline{s}$	162.5	77.4	2.10
$\tau^+\tau^-$	79.3	84.4	0.94

recording neutral objects within *BABAR* is applied.

4.3.4 Monte Carlo samples used in this analysis

Signal Monte Carlo simulations are generated to contain one B meson decay and a second B which is forced to decay to a signal mode, $B^+ \to K^+\nu\overline{\nu}$ or $B^+ \to \pi^+\nu\overline{\nu}$.

The samples we use in this analysis are outlined in table 4.1. The term "generic" means that the final state of the decay is not constrained, so any final state can be allowed (with the correct branching fraction).

Chapter 5

Recoil Method Physics

5.1 Introduction

As described in chapter 3, the collision of beams from PEP–II produces the $\Upsilon(4S)$ resonance, which subsequently decays exclusively to pairs of B mesons (either B^+B^- or $B^0\overline{B}^0$). The experimentally challenging feature of a search for $B^+ \to K^+\nu\overline{\nu}$ is the presence of the two unobserved neutrinos in the final state. These particles are missing, indeed they are undetectable in the B–factory environment. Therefore, since there is only one stable particle in the final state many other processes have the potential of mimicking the one which we are searching for. If desperate times call for desperate measures, then difficult measurements call for novel techniques!

Hence, it is the rare nature of the reaction for which we are searching that dictates the method chosen to perform the analysis. The search we perform requires the reconstruction of one of the B mesons in the event. By first isolating a sample of events where one B meson has decayed into a measurable final state, we can begin to account for the majority of the particles in the event. We shall refer to this process as *tagging* the B meson.

If one of the B's is fully reconstructed then any charged tracks and neutral clusters

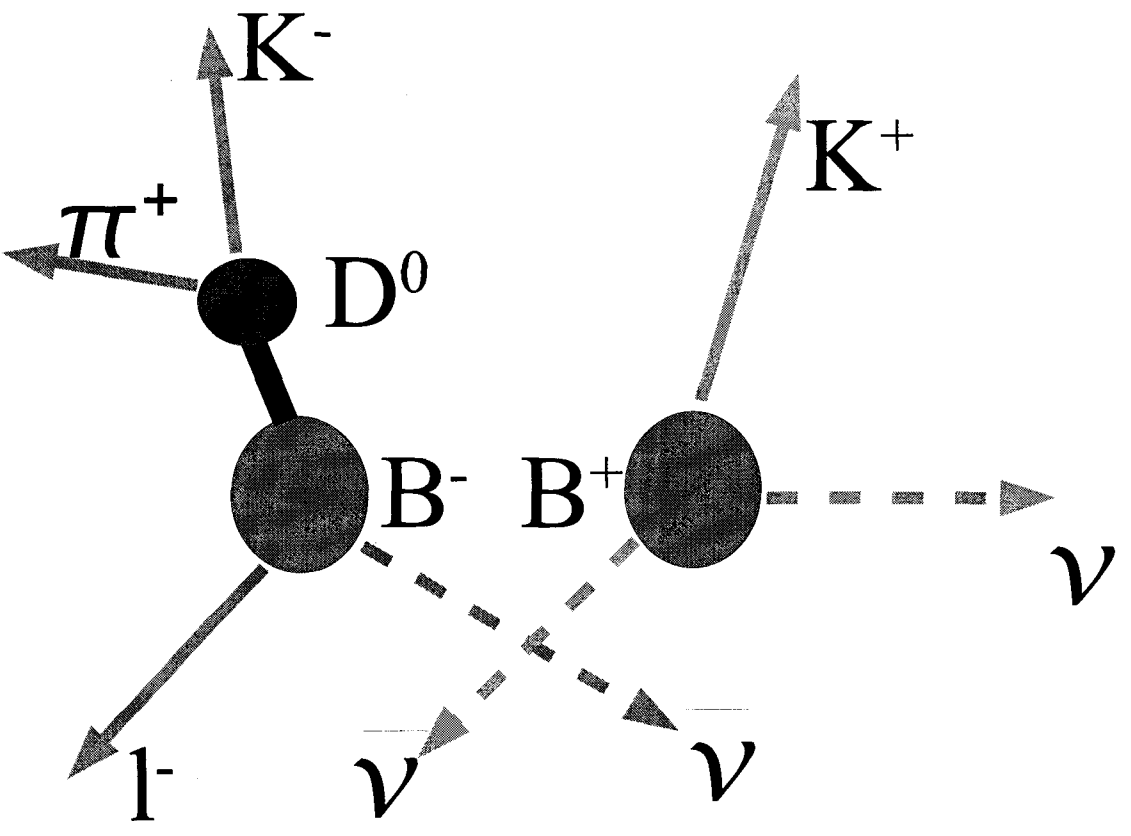

Figure 5.1: A schematic view of the recoil method applied to a signal event. The two B decays are separated in space for ease of drawing the figure.

remaining in the event can all be assumed to have been produced by the accompanying B decay. By doing this we can study the properties of the *recoil* system for consistency with the decay we are searching for as depicted in figure 5.1. In what is to follow, the reconstructed B will be referred to as the "tag" B and the accompanying B meson will be the "recoil" B.

In order to study rare decays in the recoil system, the tag sample used must provide a high statistics subset of the data. The choice of the final states considered

for the tag B mesons is therefore critical if one is to obtain a statistically meaningful sample. For this analysis a unique and completely new approach to tagging B mesons was developed. The tag B meson is reconstructed via a set of semi–leptonic, open–charm modes[1]. These processes have inherently large branching fractions. They are referred to as semi–leptonic, open–charm states due to the net charm intrinsic to the D meson and the final state lepton. These modes will be collectively depicted by the decay $B \rightarrow D\ell\nu(X)$. The ℓ denotes either an electron or a muon and after imposing kinematic requirements on the $D^0\ell$ combination, the X is usually either nothing or a soft transition pion or photon from a higher–mass charm state.

To help accurately isolate the $B \rightarrow D\ell\nu(X)$ decay process, the author has developed a software package called `BToDlnuXUser` [55] for use within the *BABAR* collaboration. The reconstruction of $D\ell$ candidates can be performed by utilising this package. The data and Monte Carlo samples outlined in chapter 4 are processed with `BToDlnuXUser`. Further constraints can then be placed on the events to improve the quality of the selected candidates. The selection of $D\ell$ candidates proceeds by building up the D^0 mesons from lighter charged and neutral mesons. The D^0 meson decay is reconstructed as either $D^0 \rightarrow K^-\pi^+$, $D^0 \rightarrow K^-\pi^+\pi^+\pi^-$ or $D^0 \rightarrow K^-\pi^+\pi^0$. These D^0 decay modes are chosen since they provide both the highest statistics hadronic decay modes and they are the cleanest. Using this technique neutral modes can be studied via $\overline{B}^0 \rightarrow D^+\ell^-\overline{\nu}$ where $D^+ \rightarrow K^-\pi^+\pi^+$. Also, if an acceptable $D^{*+}\ell^-\overline{\nu}$ candidate can be formed by combining a reconstructed D^0 with a low momentum charged pion, it is used as a $\overline{B}^0$ tag in place of the B^- tag candidate. Only those events with reconstruced B^- tags are considered suitable to study the recoiling B^+ and hence

[1]The analyses described herein were the first where this method was used. The technique has subsequently been applied to several other related analysis modes.

perform a search for $B^+ \rightarrow K^+\nu\overline{\nu}$. Using this method, missing particles in the tag B are not a problem provided that the detected particles are properly assigned. This semi–leptonic tagging method has been outlined in greater detail elsewhere [55].

In the following sections the reconstruction of mesons used in this analysis is described. In section 5.3 we will describe the reconstruction of B^- meson candidates from the objects we have associated with particular mesons and leptons. Selection criteria will be imposed to the $D^0\ell$ combinations in an attempt to ensure that they are consistent with the properties of B decays.

5.2 Meson Reconstruction

The particles observed in the detector from the decay modes used in this selection are $K^\pm$, $\pi^\pm$, $e^\pm$, $\mu^\pm$ and γ. The objects corresponding to these particles, and reconstructed in the detector, are organised into lists according to whether they are charged or neutral.

5.2.1 Charged track selection

ChargedTracks are all tracks reconstructed in the drift chamber and/or silicon vertex tracker with parameters determined using a $\pi^\pm$ mass hypothesis.

For a charged track to be considered suitable to be a daughter particle from the decay of a heavier meson it must have a momentum, measured in the lab frame, of less than 10 GeV/c. Furthermore, the distance of closest approach to the beam spot centroid must be consistent with $\sqrt{(\Delta x)^2 + (\Delta y)^2} < 1.5$ cm, and $|\Delta z| < 10$ cm.

5.2.2 Photon and π^0 selection

All "bumps" (local maxima of calorimeter energy deposit) not matched with any track are considered suitable to be clusters that are contained on a neutral cluster list.

The π^0 candidates used in this selection are collected into a list which is refitted with π^0 mass constraint, and requires that the $\gamma\gamma$ pair are entries on the neutral cluster list with:

- both bumps having a minimum energy of 30 MeV and the sum of their energies being at least 200 MeV.
- a pair invariant mass in the range of 110-155 MeV/c^2 assuming both entries are photons originating from the detector origin.
- both bumps having a lateral shower shape (LAT) consistent with the expected pattern of energy deposits for an electromagnetic shower, as determined by a cut of LAT < 0.8. The LAT variable was first used by the ARGUS collaboration is described in detail elsewhere [53].

5.2.3 K_S^0 selection

The K_S^0 candidates are reconstructed in the charged pion channel, $K_S^0 \rightarrow \pi^+\pi^-$, where two oppositely charged pions are combined by trying to find a common vertex. The candidate must lie within a loose mass window around the K_S^0 mass between 300 and 700 MeV/c^2.

5.2.4 D reconstruction

Using the reconstructed charged tracks and π^0's we can attempt to form higher mass states such as the D^0 meson. This is done by studying all possible combinations of tracks and neutral clusters to find a match consistent with the decay of a D^0. The kaon candidates must pass a loose kaon selection criteria which uses information from the SVT, DCH and DIRC, depending upon the momentum of the track. The likelihood-based selector (which is referred to in more detail in section 6.1) needs to return a value more consistent with coming from a kaon than a pion, hence the selector is referred to as the *NotAPion* selector. All other charged tracks are considered pions. The D^0 decay modes of particular interest in this analysis are $D^0 \rightarrow K^-\pi^+$, $D^0 \rightarrow K^-\pi^+\pi^+\pi^-$ and $D^0 \rightarrow K^-\pi^+\pi^0$. These decays consist of two or four charged tracks and zero or one π^0.

They are constructed thus:

- $D^0 \rightarrow K^-\pi^+$: pairs of tracks having an invariant mass within 90 MeV/c^2 of the nominal D^0 mass.
- $D^0 \rightarrow K^-\pi^+\pi^+\pi^-$: sets of four tracks with an invariant mass within 90 MeV/c^2 of the nominal D^0 mass.
- $D^0 \rightarrow K^-\pi^+\pi^0$, $\pi^0 \rightarrow \gamma\gamma$: pairs of tracks combined with a π^0 candidate having an invariant mass within 160 MeV/c^2 of the nominal D^0 mass.

The rather wide acceptance region within the invariant mass is applied to allow events to populate the "sideband" regions of the D^0 mass spectrum. These sideband samples are then used in order to study background contributions in the tagging sample from

Table 5.1: D^0 decay modes which are used by this event selection. The D^0 mass is that used in the Monte Carlo. For the states which proceed via intermediate resonances ($D^0 \to K^-\pi^+\pi^+\pi^-$ and $D^0 \to K^-\pi^+\pi^0$) the branching ratios are summed over resonant and non-resonant contributions in the Monte Carlo, and include intermediate branching ratio factors for resonance decay into the final state shown in the table.

Parent D^0 mass	Decay Mode	Branching Ratio
1865 MeV/c^2	$D^0 \to K^-\pi^+$	3.83%
	$D^0 \to K^-\pi^+\pi^+\pi^-$	7.49%
	$D^0 \to K^-\pi^+\pi^0$	13.90%

both continuum and B decays. This is explained in more detail in chapter 7. For the signal search these criteria are tightened still further as shown in table 5.2.

All of the D candidates are vertexed. A vertex fit is performed where we demand that the probability of χ^2 is >0.1% for $D^0 \to K^-\pi^+$ decays and >0.5% otherwise.

5.3 Tag B reconstruction

5.3.1 Lepton selection

In this tagging technique we require that a lepton, either electron or muon, with a centre-of-mass momentum p* >1.35 GeV/c be present. Both the electron and muon selectors are cut based and are described in greater detail in appendix A. For the electron selector, the ratio of the energy deposited in the EMC to the momentum of the particle measured at the origin is the variable with the most discriminating power. The muon selector suffers from dropping RPC efficiencies throughout the data collection period hence making our selection of muons somewhat less efficient than that of electrons. For use in the $B^- \to D^0\ell^-\overline{\nu}$ reconstruction the leptons must have the same charge as the kaon used in the D^0 reconstruction.

5.3.2 $D\ell$ selection

A suitable tag B candidate is formed by combining the reconstructed D^0 and a charged track consistent with a lepton hypothesis. To these $D^0\ell$ combinations further selection criteria are imposed in an attempt to ensure that they originated from a $B^- \rightarrow D^0\ell^-\overline{\nu}\ X$ decay. Furthermore, we must also account for the possibility that the meson in the $D^0\ell$ candidate is a daughter of some higher–mass charm state such as D^{*0}, D^{*+} or D^{**}. In the case of D^{*+} we attempt to exclusively reconstruct the decay $D^{*+} \rightarrow D^0\pi^+$. Charged pions are combined with the reconstructed D^0's and if a combination that lies within 3 MeV/c^2 of the nominal $D^{*+} - D^0$ mass difference is found it is considered to be a D^{*+} candidate. Any suitable candidate has the charged track removed from the track list and is considered a neutral B tag. Such tag candidates are not considered during the search for $B^+ \rightarrow K^+\nu\overline{\nu}$. This procedure is not carried out for daughter particles from other higher mass charm states such as D^{*0} and D^{**}. Since these daughter particles are not included among the tag particles they will populate those tracks and neutral clusters considered as originating from the recoil B. Although the exclusive reconstruction procedure mentioned for the $D^{*+} \rightarrow D^0\pi^+$ decays is not carried out in the case of neutrals, if a γ can be added to the $D^0\ell$ combination to reduce the unassigned neutral energy while making a suitable $D^{*0}\ell$ candidate this photon is associated with the tag. Note therefore that in the case of the $D^{*0} \rightarrow D^0\pi^0$ transition only the highest momentum of the two γ's will be considered. Therefore, no attempt is made to fully reconstruct the $B^- \rightarrow D^{*0}\ell^-\overline{\nu}$ but simply to correctly assign neutral energy with the B meson with which it was associated. A more detailed description of neutral energy assignment is given in appendix B. A vertex fit is performed on all of the $D^0\ell$ candidates where we demand

that the probability of χ^2 is >0.1% for $D^0 \to K^-\pi^+$ and >0.5% otherwise.

The search for $B^+ \to K^+\nu\overline{\nu}$ will occur in the recoil of B^- events and hence the discussion of tagging in what is to follow will focus solely on $B^- \to D^0\ell^-\overline{\nu}$. Selection criteria are imposed on the second Fox-Wolfram moment [54], R_2 (where R_2 is calculated using all charged tracks), and the missing mass as shown in figure 5.2 where there must be three or fewer charged tracks recoiling against the reconstructed B. Studies have shown that the disagreement in these two distributions arises from unmodelled four-fermion processes. The following constraints are applied: $R_2 < 0.84$ and M_{missing} >1.0 GeV/c^2. It should be noted that these selection criteria have little impact on the signal search when the multiplicity and neutral energy associated with the recoil B is restricted. However, these criteria do serve to ensure that the loose distributions we plot show good agreement between data and simulation without these discrepancies becoming apparent.

The cosine of the angle between the direction of the B and the sum of the D and lepton momenta, $\cos\theta_{B,D\ell}$, calculated in the $\Upsilon(4S)$ rest frame is essential to this selection. The angle is not measured directly since there is no handle on the B direction. Instead we can calculate this quantity by assuming that the only particle missed in our reconstruction is a massless neutrino. Subsequently the energy of the tag B meson can be determined from the electron and positron beam information in the centre–of–mass frame. Equating the four-vector of the colliding electron to P_e and that of the positron to P_p one can define the energy of the B mesons, E_B as

$$E_B = \frac{1}{2}\sqrt{(P_e + P_p)^2}, \tag{5.1}$$

and the momentum magnitude of the B meson, $\mid \vec{p}_B \mid$ as

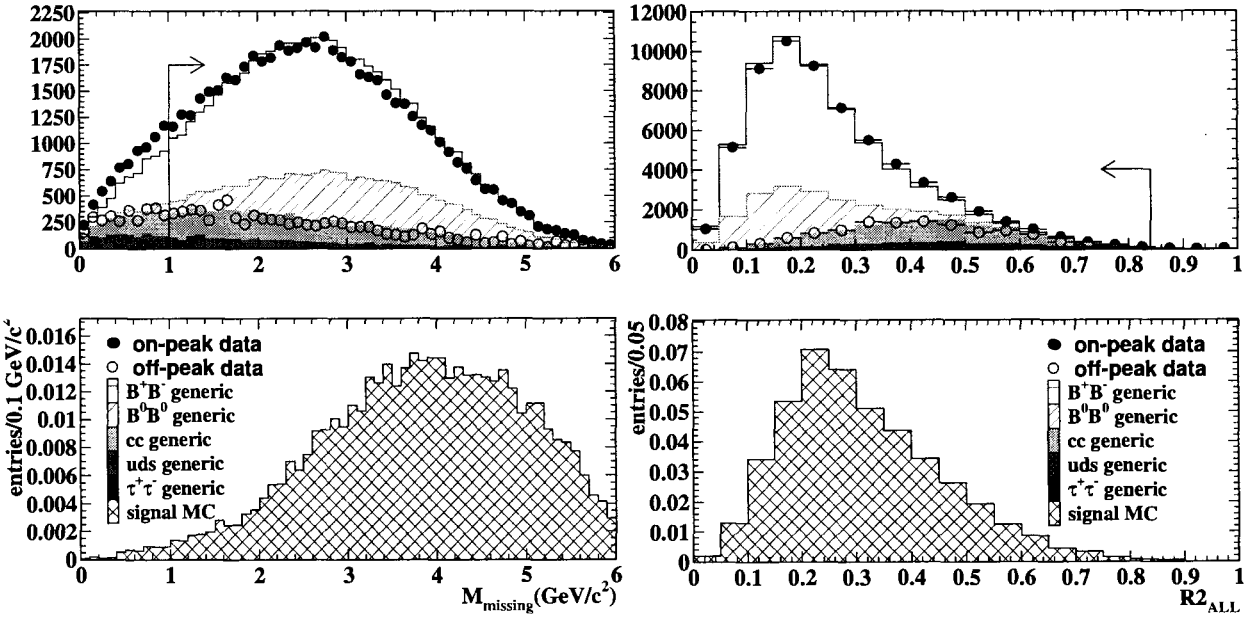

Figure 5.2: A plot of the missing mass (GeV/c^2) (on the left) and R_2 (on the right) using all MC ($B\overline{B}$, $q\overline{q}(q = u, d, s$ or $c)$ and $\tau^+\tau^-$), onpeak and offpeak data. All distributions are scaled to the onpeak data luminosity. The $B^+ \rightarrow K^+\nu\overline{\nu}$ signal MC is plotted for comparison.

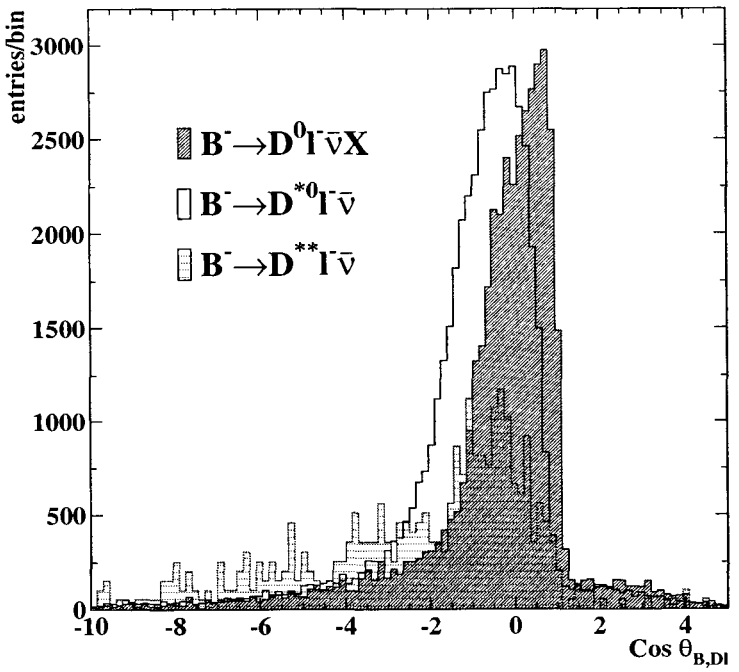

Figure 5.3: The $\cos\theta_{B,D\ell}$ distribution for for events with a true $B^+ \to D^0\ell\nu(X)$, $B^+ \to D^{*0}\ell\nu$ and $B^+ \to D^{**}\ell\nu$. This illustrates the asymmetric nature of $\cos\theta_{B,D\ell}$ for events with a higher-mass charm state. All distributions are normalised to equal area.

$$| \vec{p}_B | = \sqrt{E_B^2 - m_B^2}. \tag{5.2}$$

The angle between the $D\ell$ and the B^- meson is defined as

$$\cos\theta_{B,D\ell} = p_{\vec{B}} \cdot p_{\vec{D\ell}} / |p_B||p_{D\ell}|. \tag{5.3}$$

If one assumes that the only particle missing is a neutrino then this can be written,

$$\cos\theta_{B,D\ell} = \frac{(2\,E_B E_{D^*\ell} - m_B^2 - m_{D^*\ell}^2)}{2\,|\vec{p}_B||\vec{p}_{D^*\ell}|}. \tag{5.4}$$

If this is truly the case, and the only particle missing is the neutrino, $\cos\theta_{B,D\ell}$ should lie in the physical range (-1,+1). A loose selection is applied to this variable in order to allow for the possibility of missing a soft particle when reconstructing the tag. Such events populate the negative region of the $\cos\theta_{B,D\ell}$ distribution hence we allow events with $-2.5 < \cos\theta_{B,D\ell} < 1.1$. The motivation for the asymmetry of this restriction can be seen in figure 5.3 where the $D^0\ell$ combinations resulting from higher mass charm state decays have $\cos\theta_{B,D\ell}$ that tend towards negative values. This plot shows the true Monte Carlo contributions from $B^- \to D^0\ell^-\overline{\nu}(X)$, $B^- \to D^{*0}\ell^-\overline{\nu}$ and $B^- \to D^{**}\ell^-\overline{\nu}$ decays. The D^{**} decays include essentially any higher mass charm state. The unphysical upper constraint on $\cos\theta_{B,D\ell}$ of 1.1 is to account for any reconstruction and detector effects (energy and momentum resolution) that may feed into the calculation. This distribution is plotted in figure 5.4 for all MC contributions scaled to the dataset luminosity with onpeak data overlayed, the signal MC is plotted for comparison.

Having searched an event for a suitable tag candidate a provision is made to account for the possibility of more than one suitable tag having been found. The candidate that has a value of $\cos\theta_{B,D\ell}$ closest to zero is the one that is taken as being the most suitable for further study, hence the "peaking" towards zero in figure 5.4. Although not necessarily the optimal choice this decision was used so as to exploit the kinematic constraints provided by $\cos\theta_{B,D\ell}$ and to avoid utilising the D^0 invariant mass distribution in the best $D\ell$ selection. The D^0 mass remains unbiased by making this choice and allows the sidebands of the distribution to be used to estimate (or subtract) background in the signal region. Applying all the criteria in table 5.2 and the subsequent selection of the best $D^0\ell$ candidate in the event yields our final sample $B^- \to D^0\ell^-\overline{\nu}$ candidates.

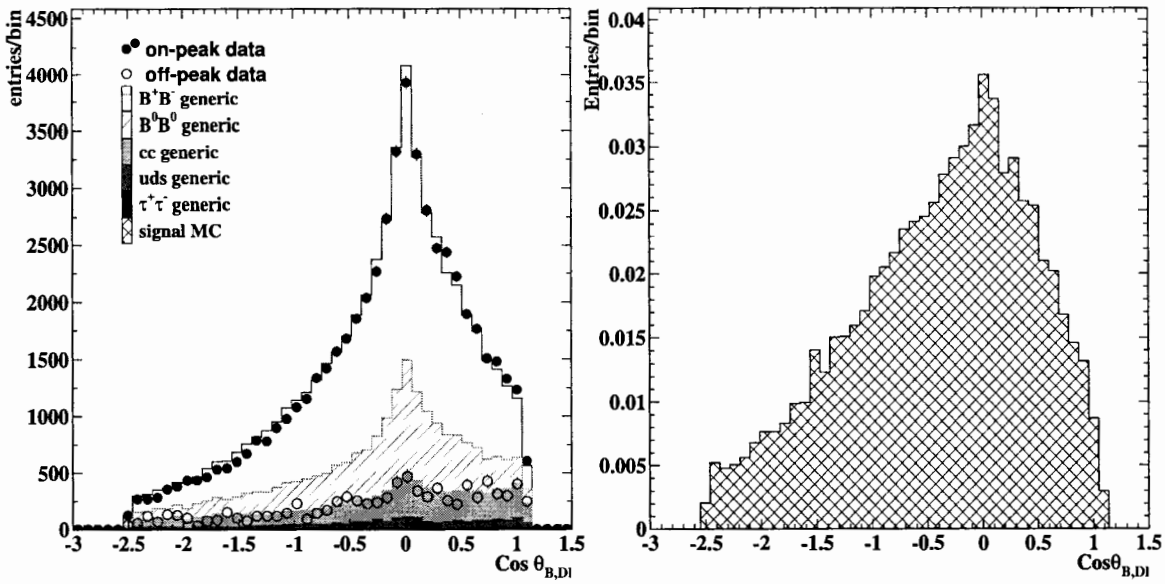

Figure 5.4: A plot of the $\cos\theta_{B,D\ell}$ for all modes using all MC ($B\overline{B}$, $q\overline{q}(q = u, d, s$ or $c)$ and $\tau^+\tau^-$), onpeak and offpeak data. All distributions are scaled to the onpeak data luminosity. The $B^+ \to K^+\nu\overline{\nu}$ signal MC is plotted on the right.

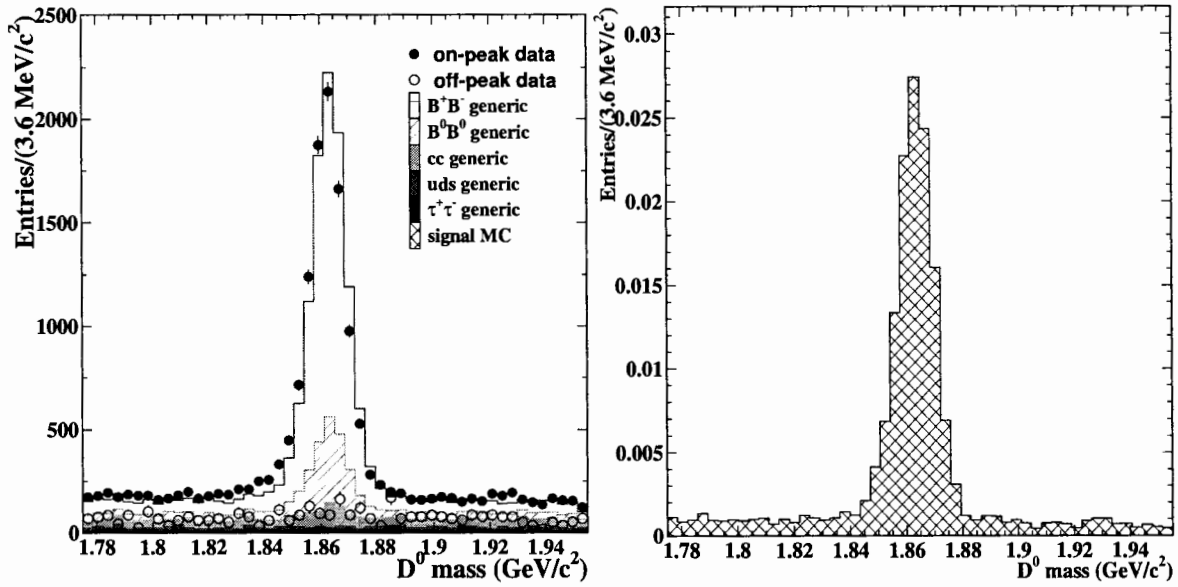

Figure 5.5: A plot of the D^0 mass for $D^0 \to K^-\pi^+$, showing, on the left, individual MC contributions and offpeak data all scaled to the onpeak dataset luminosity. The onpeak data is overlayed. The $B^+ \to K^+\nu\overline{\nu}$ signal MC is plotted on the right.

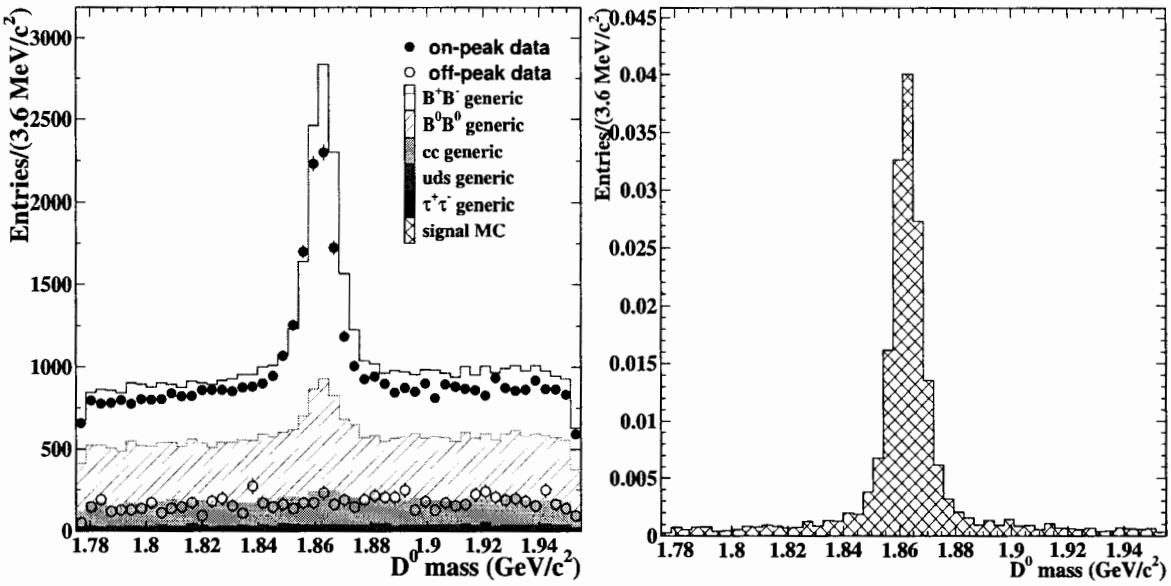

Figure 5.6: A plot of the D^0 mass for $D^0 \to K^-\pi^+\pi^+\pi^-$, showing, on the left, individual MC contributions and offpeak data all scaled to the onpeak dataset luminosity. The onpeak data is overlayed. The $B^+ \to K^+\nu\overline{\nu}$ signal MC is plotted on the right.

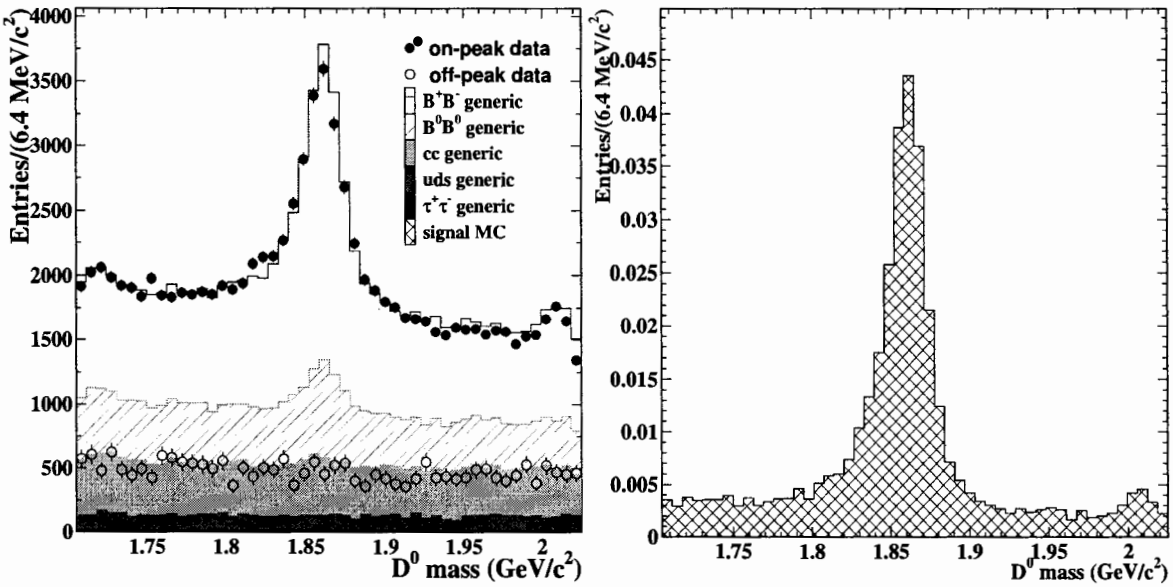

Figure 5.7: A plot of the D^0 mass for $D^0 \to K^-\pi^+\pi^0$, showing, on the left, individual MC contributions and offpeak data all scaled to the onpeak dataset luminosity. The onpeak data is overlayed. The $B^+ \to K^+\nu\overline{\nu}$ signal MC is plotted on the right.

Table 5.2: Selection criteria for tagged events. The table is split by D decay mode as some criteria are mode dependent.

	$D^0 \to K^-\pi^+$	$D^0 \to K^-\pi^+\pi^+\pi^-$	$D^0 \to K^-\pi^+\pi^0$
N $D\ell$	≤ 9	≤ 9	≤ 9
N J/ψ	0	0	0
P(D Vtx)	$> 1\times10^{-3}$	$> 5\times10^{-3}$	$> 5\times10^{-3}$
P($D\ell$ Vtx)	$> 1\times10^{-3}$	$> 5\times10^{-3}$	$> 5\times10^{-3}$
$D\ell$ mass(GeV)	> 3.0	> 3.0	> 3.0
D momentum(GeV)	> 0.5	> 0.5	> 0.5
D^{*+} mass window (MeV)	$\pm$ 3	$\pm$ 3	$\pm$ 3
$\cos\theta_{B,D\ell}$ window	-2.5 $\to$ 1.1	-2.5 $\to$ 1.1	-2.5 $\to$ 1.1
$p_{\text{tag lepton}}$ (GeV)	> 1.35	> 1.35	> 1.35
D mass window	$\pm 3\sigma$	$\pm 3\sigma$	$\pm 3\sigma$
Number of tracks remaining	$\leq$ 3+2V0	$\leq$ 3+2V0	$\leq$ 3+2V0

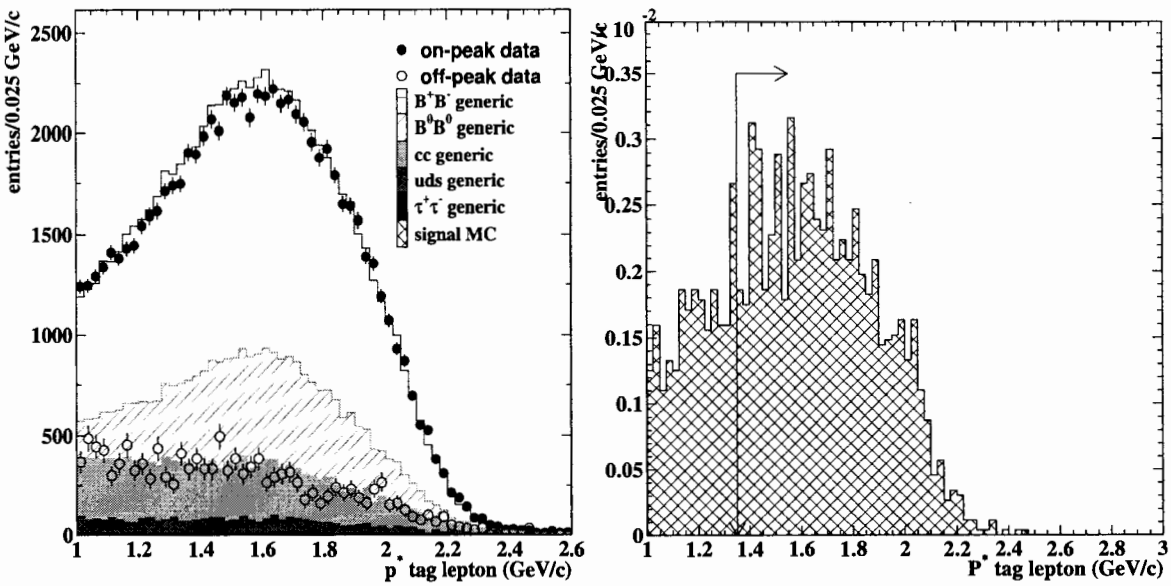

Figure 5.8: A plot of the p* lepton used in the tag for all modes using all MC ($B\overline{B}$, $q\overline{q}(q = u, d, s$ or $c)$ and $\tau^+\tau^-$), onpeak and offpeak data. All distributions are scaled to the onpeak data luminosity. The $B^+ \to K^+\nu\overline{\nu}$ signal MC is plotted on the right.

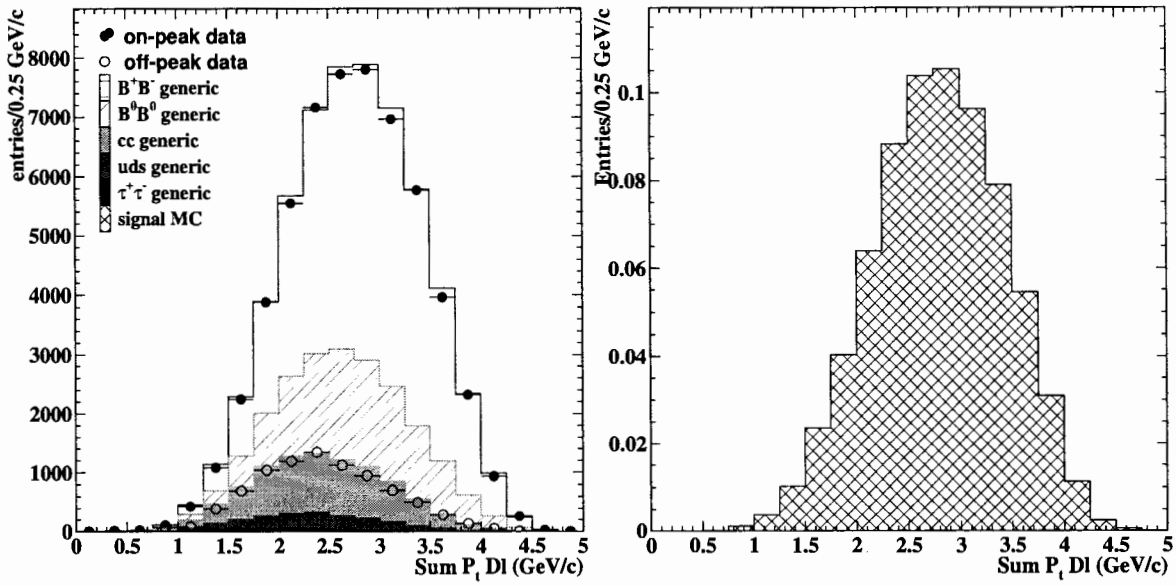

Figure 5.9: A plot of the sum of the transverse momenta used in the $D\ell$ for all modes using all MC ($B\overline{B}$, $q\overline{q}(q = u, d, s$ or $c)$ and $\tau^+\tau^-$), onpeak and offpeak data. All distributions are scaled to the onpeak data luminosity. The $B^+ \to K^+\nu\overline{\nu}$ signal MC is plotted on the right.

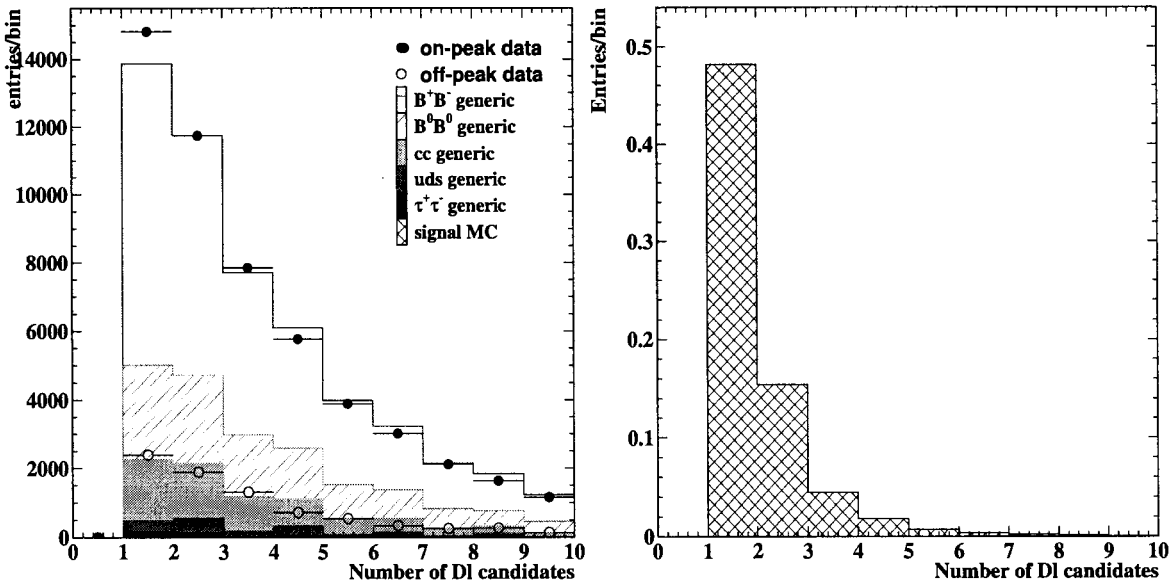

Figure 5.10: A plot of the number of $D\ell$ candidates for all modes using all MC ($B\overline{B}$, $q\overline{q}(q = u, d, s$ or $c)$ and $\tau^+\tau^-$), onpeak and offpeak data. All distributions are scaled to the onpeak data luminosity. The $B^+ \to K^+\nu\overline{\nu}$ signal MC is plotted on the right.

The search for $B^+ \to K^+\nu\overline{\nu}$ is then carried out on the subset of events containing these candidates. Figures 5.4 to 5.10 show distributions where the best $D^0\ell$ has been selected. All figures, unless stated otherwise, show the individual MC contributions from B^+B^-, $B^0\overline{B}^0$, $q\overline{q}$ (where $q = u, d, s, c$) and $\tau^+\tau^-$ scaled to the dataset luminosity with the onpeak and offpeak data (scaled to onpeak luminosity) overlayed. In each of these plots a selection is applied to only look at those events with three remaining tracks or less, and less than 1 GeV of remaining neutral energy after the tag side particles have been assigned. In this way the generic Monte Carlo sample and the data have a signal side at least similar to the $B^+ \to K^+\nu\overline{\nu}$ signal, but with a higher track multiplicity. Figures 5.5, 5.6 and 5.7 show the D^0 invariant mass distributions for all contributions(left) and signal MC(right) after applying the selection criteria in table 5.2.

In the event that the $D^0\ell$ combination came from a semileptonic $B^- \to D^0\ell^-\overline{\nu}$ decay then the remaining activity within the detector can be associated with the recoil B. It is clear therefore that this technique can be applied to many analyses where the reconstruction of one of the two B's in the event is desired. The semileptonic reconstruction method has been used in the search for the rare decays $B^+ \to \tau^+\nu$ [56] and $B \to$invisible$(+\gamma)$ [57] and is currently used in analyses studying $B \to \pi\ell\nu$, $B \to X_u\ell\nu$ and $B \to X_s\gamma$. There is strong potential for the future use of this technique with many other leptonic, radiative and semileptonic B decays.

The tagging efficiency using the signal Monte Carlo is separated by mode and given in table 5.3. We have a data sample of 88.9×10^6 $B\overline{B}$ pairs which, using the efficiency from table 5.3, corresponds $\sim$5600 tags/ fb^{-1}.

Table 5.3: Measurements of the tagging efficiency using the three D^0 decay modes considered for the $B^- \to D^0 \ell^- \overline{\nu}$ decay channel

Tag decay channel	Tag efficiency
$D^0 \to K^- \pi^+$	$(1.34 \pm 0.02) \times 10^{-3}$
$D^0 \to K^- \pi^+ \pi^+ \pi^-$	$(1.54 \pm 0.03) \times 10^{-3}$
$D^0 \to K^- \pi^+ \pi^0$	$(2.41 \pm 0.03) \times 10^{-3}$
Total	$(5.30 \pm 0.05) \times 10^{-3}$

5.4 Hadronic B reconstruction

A complimentary method, exploited by a related analysis, involves the reconstruction of the tag B decaying into a set of hadronic final states. The essence of this tag B reconstruction method is to search for decays of the form $B^- \rightarrow D^0 X^-$ by starting from an exclusively-reconstructed D^0 candidate, then combining this candidate with additional $\pi^\pm$, $K^\pm$, $K^0_S(\rightarrow \pi^+\pi^-)$ and π^0 $(\rightarrow \gamma\gamma)$ candidates until the combination yields a candidate within the expected energy range for a B decay. In order to separate signal candidate B events from background combinations, two variables, ΔE and $m_{\rm ES}$, are defined. The variable ΔE can be used to impose energy conservation on the fully reconstructed B meson. ΔE is referred to as the *energy difference* and is defined thus,

$$\Delta E = E^*_B - \sqrt{s}/2, \tag{5.5}$$

where E^*_B is the energy of the B candidate in the $\Upsilon(4S)$ rest frame and $\sqrt{s}$ is the total energy of the e^+e^- system in the centre-of-mass rest frame Specifically, all candidates must have a ΔE which lies within an initial window -0.2 GeV $< \Delta E <$ 0.2 GeV. Additional mode-specific ΔE requirements are imposed. Only a single B candidate is selected per event and, if more than one suitable candidate is found, the "best" candidate is chosen to be the one with ΔE closest to zero. Consequently, the ΔE distribution of selected candidates will peak at zero, even for incorrectly reconstructed candidates. ΔE is treated in the same way that the $\cos\theta_{B,D\ell}$ distribution is for the semi–leptonic reconstruction technique. The *beam energy-substituted mass*, $m_{\rm ES}$ is defined as:

$$m_{\rm ES} = \sqrt{(\sqrt{s}/2)^2 - p^{*2}_B}, \tag{5.6}$$

where p^*_B is the B candidate momentum in the centre-of-mass rest frame. It is interesting to note that since $|p^*_B| << \sqrt{s}/2$ the experimental resolution on $m_{\rm ES}$ is

dominated by fluctuations in the beam energy. The $m_{\rm ES}$ distribution remains unbiased by the reconstruction process and is therefore used throughout this technique as both a signal selection variable and to define regions for background studies. This is analogous to the use of the D^0 mass in the semi–leptonic technique. One should note that, due to the missing neutrino, ΔE and $m_{\rm ES}$ cannot be used in the case of the $B \rightarrow D\ell\nu(X)$ technique.

Tag B candidates use one of four D^0 decay modes: $D^0 \rightarrow K^-\pi^+$, $D^0 \rightarrow K^-\pi^+\pi^+\pi^-$, $D^0 \rightarrow K^-\pi^+\pi^0$ and $D^0 \rightarrow K^0_s\pi^+\pi^-$. Reconstructed D^0 candidates are required to satisfy similar criteria to those described in section 5.2.4. Although D^{*0} candidates are not explicitly included in this technique, $D^{*0} \rightarrow D^0\pi^0$ decays will still contribute with reasonable efficiency to the tag B reconstruction. For example, the decay $B^- \rightarrow D^{*0}\pi^-$ would be reconstructed as $B^- \rightarrow D^0\pi^-\pi^0$. Since the only purpose of the B reconstruction is to "veto" tracks and clusters from the signal-side, this assignment is sufficient, since all daughter particles of the tag B have been correctly identified as such. Imposing an additional constraint on the mass difference $m_{D^{*0}} - m_{D^0}$ would only further lower the reconstruction efficiency with no significant improvement in the backgrounds.

Recoil analyses can be performed using both hadronic and semi–leptonic reconstruction methods. In the case of the search for $B^+ \rightarrow K^+\nu\overline{\nu}$ and $B^+ \rightarrow \pi^+\nu\overline{\nu}$, analyses were pursued using both techniques. The hadronic reconstruction technique explicitly vetos leptons when selecting the tag candidate tracks. Therefore, the two reconstruction methods produce mutually exclusive data samples it permitting the combination of the statistically independent results to obtain an improved limit. This thesis will concentrate only on the details of searches in the recoil of semi–leptonic tags.

Chapter 6

Search for $B^+ \to K^+\nu\overline{\nu}$

Signal candidate events are selected from events in which a suitable tag B candidate is found by examining the detector activity which is not associated with the daughters of the reconstructed tag. The recoiling signal candidate is presumed to be composed of all reconstructed objects (tracks and clusters) not associated with the tag B. Under the hypothesis that the $B^+ \to K^+\nu\overline{\nu}$ decay is the only signal-side[1] activity, and assuming a perfect detector, one would expect only a single charged track associated with the signal kaon. However, in practice, additional activity, mostly in the EMC, is present due to both detector and physics effects (such as Bremsstrahlung and hadronic split-offs). The basic signal side selection involves searching for a single track that satisfies imposed requirements such that it is consistent with coming from a kaon, while limiting additional activity within the detector volume. The candidate kaon track must:

- lie within the angular acceptance of the DIRC $0.469 < \theta < 2.457$;
- satisfy the *tight* kaon identification requirements from

[1]When we make reference to a "side" with regards to the recoiling signal candidate and the tag this is only to distinguish the two B's since in practice there is no separation or preferred direction.

the *PidKaonSMSSelector*, as discussed in section 6.1;

- have a charge which is opposite to that of the lepton used on the tag side.

As the kaon is the only signal candidate particle we directly search for, the amount of other activity in the detector, due to charged tracks or neutral clusters, provides a signature of how consistent the event is with a signal candidate. Isolating the events that contain such background activity is one requirement involved in defining our signal candidate search. Hence, it is paramount to understand the activity within the detector and the sources from which these spurious detector responses arise. Along with identifying a suitable signal candidate kaon track this provides the only means by which we can search for the $B^+ \to K^+\nu\overline{\nu}$ signal in the presence of background. There are several quantities which can be used to separate signal from background after the tag side particles have been removed from the event. These include:

- the number of reconstructed charged tracks not assigned to the tag B;
- the extra neutral energy in the calorimeter not assigned to the tag B;
- the momentum of the kaon candidate track;
- the number of remaining K_L^0 candidates reconstructed in the EMC and IFR;
- the polar angle distribution of kaon candidate tracks;
- various event shape variables.

This list is not necessarily an exhaustive one. The quantities we list are those which have been studied in detail and were found to exhibit sensitivity for this search. The

above quantities will be addressed separately in the following sections, where we shall explain how each variable is used to select signal candidates and suppress background. Some of the variables are not used in the final cut selection but are described here in order to furnish the reader with the understanding of why that choice was made. It should be noted that the analysis was performed blind as described in detail in section 7.1. Distributions are plotted in this section with loose selection criteria applied. In all cases distributions have the best B tag selected and for most plots three or fewer charged tracks and less than 1 GeV of unassociated neutral energy in the EMC are demanded. It should be noted that for variables such as E_{extra} and charged track multiplicity these requirements are clearly not imposed. Also, for quantities such as the kaon momentum, a suitable kaon candidate must be selected.

6.1 Kaon identification

Kaon selection, and issues relating to it in *BABAR*, have been analysed in depth elsewhere [59].

The *PidKaonSMSSelector* is based on likelihood ratios mainly between the particle types: pion, kaon and proton. The tight kaon selection is optimised to keep the mis-identification below 2% up to a momentum of 4 GeV/c. For candidate kaons with momenta of $p > 0.6$ GeV/c, identification is based primarily on angular information from the DIRC. The signature of kaons in the Cherenkov detector is quite complex. Their Cherenkov angle distribution from Monte Carlo after the likelihood fit described in [59] is shown in figure 6.1. The fit steps through the different particle hypotheses fitting the Cherenkov angle and arrival time distribution of the photons associated to a track. The kaon band is labelled as region (C). Region (A) is populated by tracks for which no Cherenkov angle fit is performed, because either they

did not reach the DIRC (8% of which is due to solid angle coverage of the DIRC), or produced a small amount of photons compared to background photons near to particle threshold. Close to kaon threshold, kaons do show up in the electron, muon and pion band with a rather wide spread, marked as region (B). These kaons decayed or interacted before the DIRC and the reaction products did not deviate much from their mother kaon direction. Region (D) corresponds to the proton band.

For momenta below 0.6 GeV/c energy loss measurements (dE/dx) from both the SVT and DCH are used. This will not be relevant for the momentum range of the signal candidates we select (see section 6.3) and therefore we impose the constraint that selected candidates must lie within the DIRC acceptance. The charged kaon identification efficiency obtained by this selection is 85% - 95% for a momentum range of 1 GeV/c $< p^* <$ 3 GeV/c. This analysis has an efficiency which is fairly uniform in the region of interest as figure 17 in [59] presents. The charged track multiplicity of the signal side candidate is plotted in figure 6.2. It is clear that demanding there is only a single charged track recoiling against the reconstructed B candidate removes a large portion of the background events.

6.2 Neutral Energy

Figure 6.3 shows the total remaining neutral energy in the event after all tag side tracks and neutral clusters have been accounted for. This variable will be referred to herein as E_{extra}. In a perfect detector, E_{extra} for a reconstructed signal event would be zero (modulo any unassociated energy from the tag B). However, in practice this is not the case. Unassigned neutral energy comes not only from unassociated tag-side photons but also Bremsstrahlung photons (from electrons in the tag B), split-offs from hadronic showers (where neutrals can be cast laterally into the calorimeter) and beam

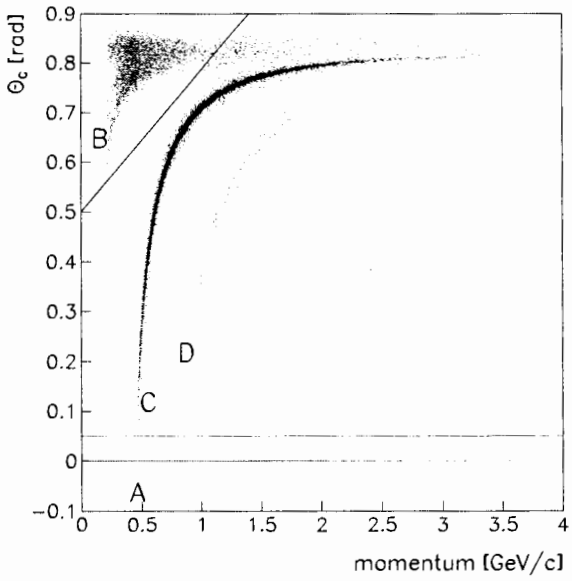

Figure 6.1: Distribution of Cherenkov angle measurements versus track momenta for simulated kaon tracks.

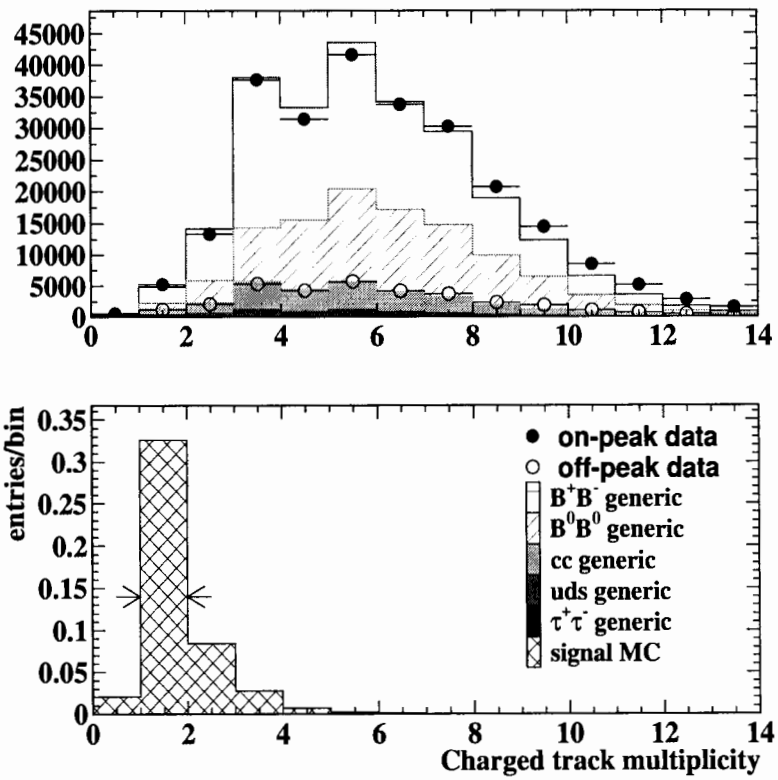

Figure 6.2: A plot of the number of remaining tracks after all the tag side particles have been removed from the event. All Monte Carlo ($B\overline{B}$, $q\overline{q}(q = u, d, s$ or $c)$ and $\tau^+\tau^-$), onpeak and offpeak data are plotted. Distributions are scaled to the onpeak data luminosity. The $B^+ \to K^+\nu\overline{\nu}$ signal Monte Carlo is plotted for comparison. The arrow corresponds to the cut applied.

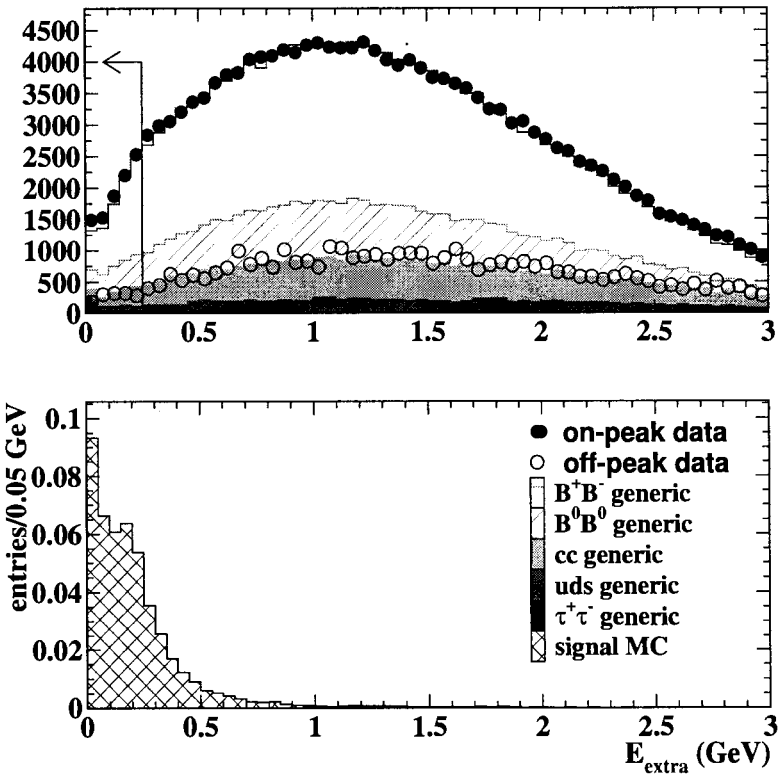

Figure 6.3: A plot of the remaining neutral energy after all the tag side particles have been removed from the event. All Monte Carlo ($B\overline{B}$, $q\overline{q}(q = u, d, s$ or $c)$ and $\tau^+\tau^-$), onpeak and offpeak data are plotted. Distributions are scaled to the onpeak data luminosity. The $B^+ \to K^+\nu\overline{\nu}$ signal Monte Carlo is plotted for comparison. The arrow corresponds to the cut applied.

related background photons. Other neutral clusters can come from neutral hadrons (predominantly K_L^0's) interacting in the calorimeter. The neutral energy clusters that are considered for this analysis are outlined in more detail in appendix B.

In order to retain a large portion of the signal while minimizing the background the $B^+ \to K^+\nu\overline{\nu}$ signal is searched for in the region where E_{extra} is less than 250 MeV. This value was optimized as outlined in section 6.7. This selection criterion is essential for isolating the signal region from backgrounds and is used in the definition of the "signal box". We study a number of sideband regions prior to extracting the signal yield and these, along with the signal region, are all described in section 7.4. In figure 6.4 we show the average multiplicity of π^0's and neutral clusters in an event. Although there is a clear separation between signal and background events these quantities are strongly correlated with E_{extra} and so they are not considered for the final selection criteria.

6.3 Kaon Candidate momentum

Figure 6.5 shows the centre-of-mass frame momentum of the remaining signal candidate track with all generic Monte Carlo contributions plotted and data overlayed. As can be seen the SM signal candidates have preferentially higher momenta than those from the background. A cut is applied on this variable at $p_K^* > 1.25$ GeV/c in order to reduce background and retain a high portion of the signal sample. As part of the "cut-and-count" analysis, and in order to extract a limit for the Standard Model $B^+ \to K^+\nu\overline{\nu}$ decay, we impose this constraint on the kaon momentum. The final yields and efficiencies are also quoted in bins of the kaon momentum. If there is no positive signal observed in this search limits on non-Standard Model processes can be placed. However, any non-Standard Model process may distort the kaon momen-

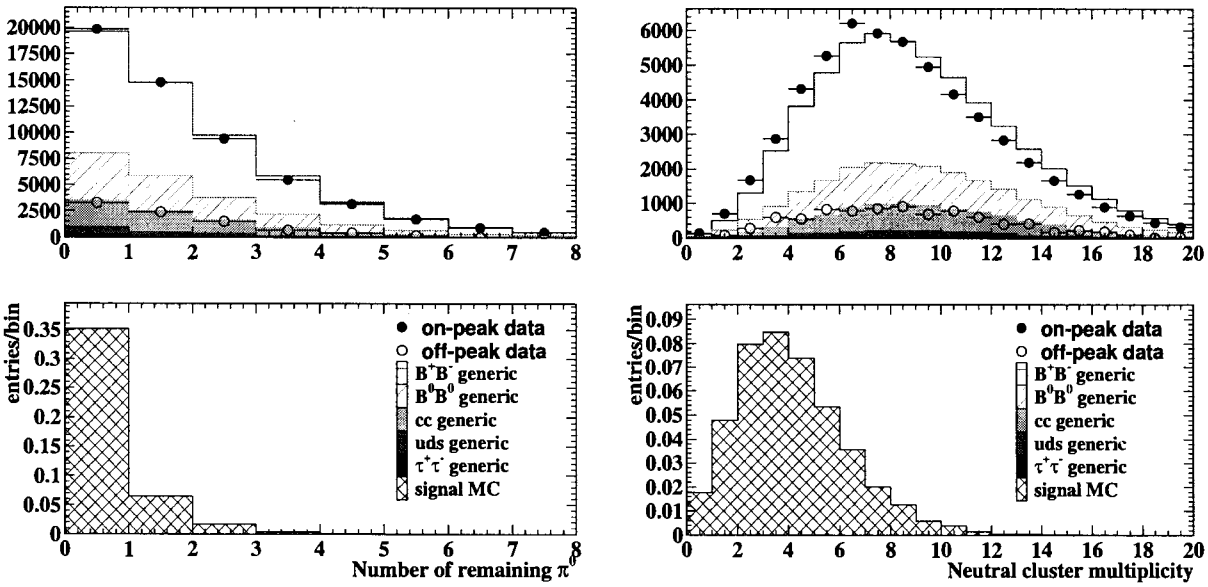

Figure 6.4: Number of π^0 (left) and γ's (right) remaining in the event after removal of the tag candidate. Background Monte Carlo and data are overlayed and signal Monte Carlo is plotted for comparison.

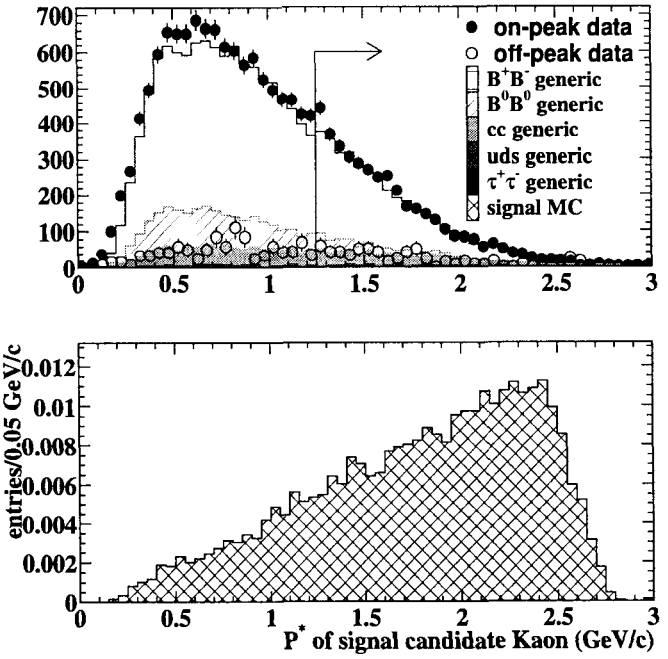

Figure 6.5: A plot of the momentum of the signal candidate track after all the tag side particles have been removed. Background Monte Carlo ($B\overline{B}$, $q\overline{q}(q = u, d, s$ or $c)$ and $\tau^+\tau^-$), onpeak and offpeak data. All distributions are scaled to the onpeak data luminosity. The $B^+ \to K^+\nu\overline{\nu}$ signal Monte Carlo is plotted for comparison. The arrow corresponds to the cut applied.

tum spectrum such that it differs from that expected in the Standard Model decay. Extracting the final result as a function of the kaon momentum enables limits to be produced on models requiring this information.

For the signal Monte Carlo samples used, the kaon momentum spectrum is generated using a phase space model. This distribution is reweighted using models extracted from the literature [19, 20].

6.4 Neutral hadrons, K_L^0's, in the EMC and IFR

Since our signal mode involves only a single kaon, events containing neutral hadron candidates and IFR activity should be from background sources.

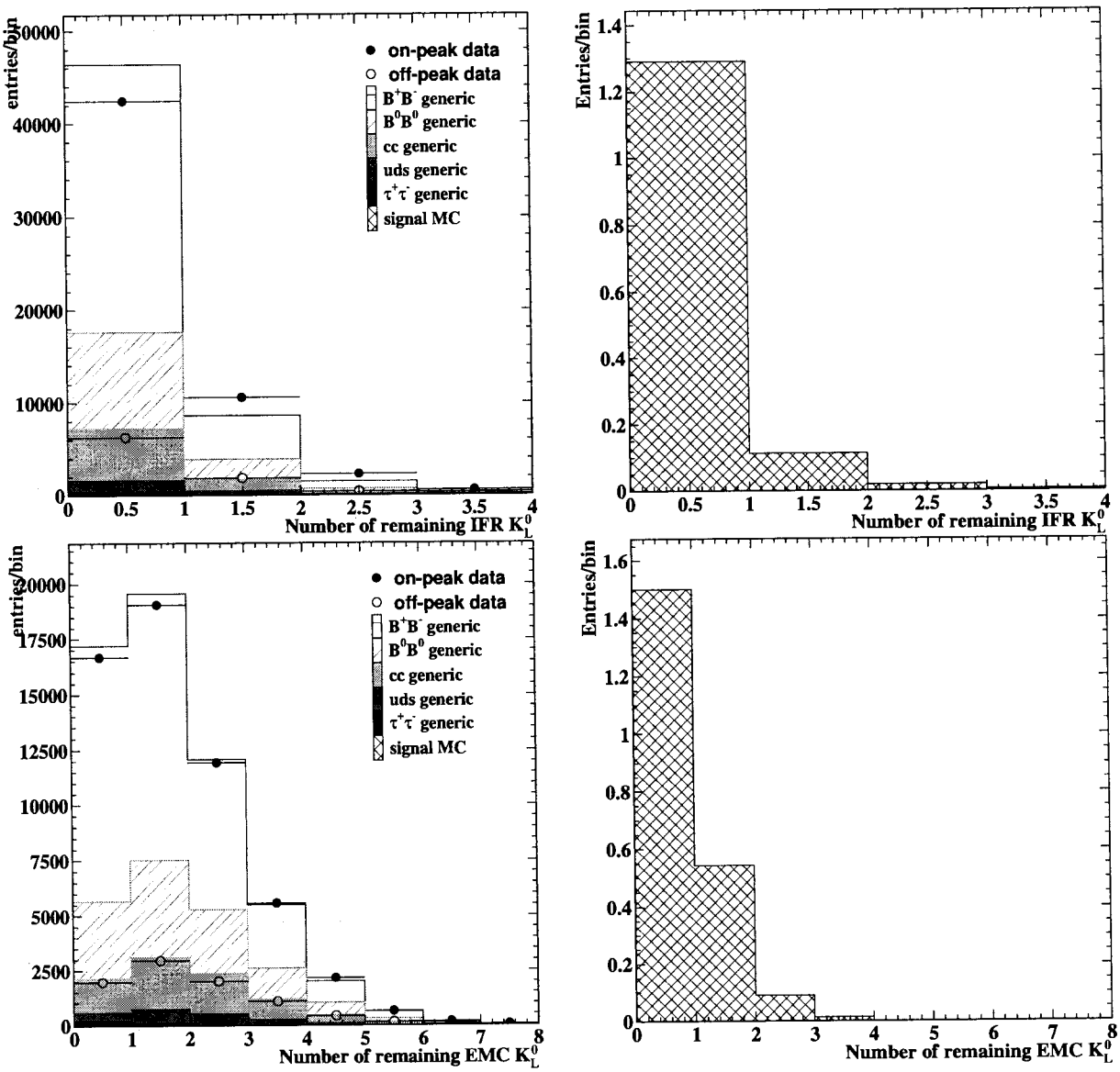

Figure 6.6: Number of K_L^0 candidates in the event and EMC only K_L^0 candidates. All Monte Carlo and data are overlayed and signal Monte Carlo is plotted for comparison.

We construct K_L^0 candidates in the IFR by using as input a list of neutral hadron candidates. We then impose the following requirements:

- at least two planar layers must have recorded hits;
- a polar angle fiducial cut on the cluster of -0.75 < cos θ < 0.93;
- the relative position between the cluster centroid and the EMC position of any track with at least 0.75 GeV/c of momentum must satisfy $|\theta_{K_L^0}$ - $\theta_{trk}|$ < 350 mrad, as well as -750 < $\phi_{K_L^0} - \phi_{trk}$ < 300 mrad for positively charged tracks, and -300 < $\phi_{K_L^0} - \phi_{trk}$ < 750 mrad for negatively charged tracks.

The candidates passing these criteria are gathered together and collectively referred to as as the *IFRTightKlList*.

K_L^0 candidates can also be constructed from EMC information. The requirements for these are:

- the centroid of the cluster must have cos θ <0.935;
- the cluster energy is at least 200 MeV and not more than 2 GeV;
- the probability returned by a track-shower matching algorithm is less than 1%;
- require that the K_L^0 does not form a $\gamma\gamma$ mass between 100 and 150 MeV/c^2;
- reject two–bump clusters with a cluster energy larger than 1 GeV that are consistent with being merged π^0's.

The candidates that successfully pass the criteria imposed on the EMC K_L^0's are collected into the *EMCTightKlList*.

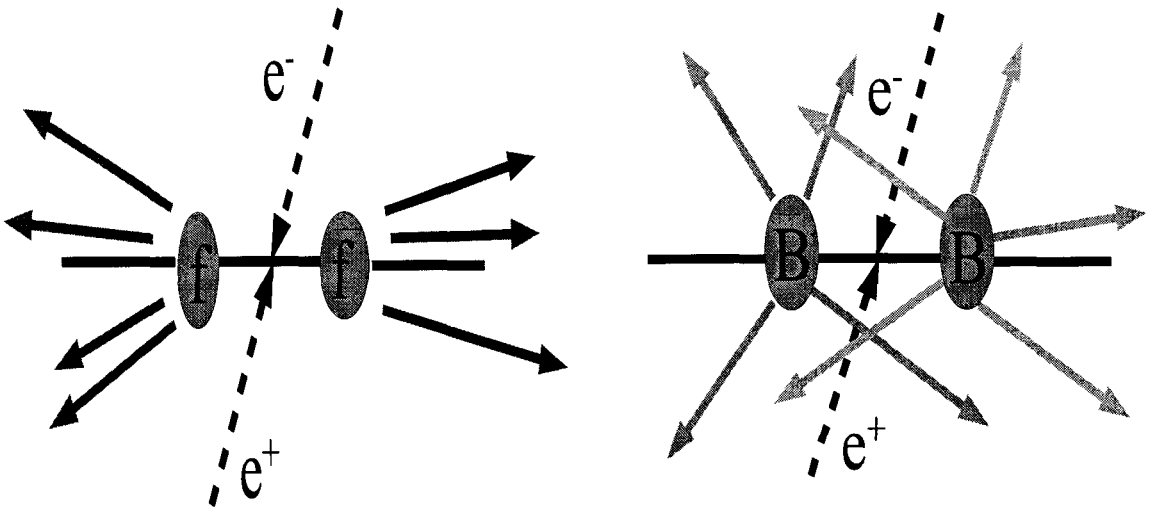

Figure 6.7: A graphical representation of a continuum background process(left) and a $B\overline{B}$ process(right).

Events containing K_L^0's have been seen to be a source of background in many of the rare decay analyses with missing energy in *BABAR*. Studies have been carried out regarding a veto on K_L^0's that deposit energy in the EMC [58]. Since this would be a real physics background to the signal we are searching for we consider it to be important. The distributions of the number of K_L^0 in the event using the *EMCTightKlList* and *IFRTightKlList* are shown in figure 6.6. Even with these loose criteria imposed we see some separation between signal and backgrounds. However, for this analysis we do not impose any cut on the number of K_L^0 candidates on either the *EMCTightKlList* or the *IFRTightKlList*. This is discussed further in section 6.7.

6.5 Shape Variables

There is significant contamination of the tag B sample due to combinatoric backgrounds from continuum events. In the case of $c\overline{c}$ events this can occur when either

a real or combinatoric D^0 is combined with a lepton to produce a B^+ candidate with the properties of the tag B's we consider. In the case of $u\overline{u}$, $d\overline{d}$, $s\overline{s}$ or $\tau^+\tau^-$ the D^0 is also combinatoric in nature. We can suppress these backgrounds by exploiting the topologies of continuum events compared with $B\overline{B}$ decays. This is displayed graphically in figure 6.7. $B\overline{B}$ decays are much more spherical in nature than the more "jet-like" continuum events.

Figure 6.8 shows $\cos\theta_{K,\ell}$, the cosine of the angle between the K candidate and the lepton used in the reconstructed B. Figure 6.9 shows $\cos\theta_{K,D^0}$, the cosine of the angle between the K candidate and the D^0 meson used in the reconstructed B. Figure 6.10 shows $\cos\theta_{\vec{T},K}$, the cosine of the angle between the K candidate and the thrust axis of the rest of the event, $\vec{T}$. Since we expect continuum processes to exhibit a "jet-like" topology compared to the more spherical B decay we can exploit angular correlations between the kaon and the tag-side particles. This serves the purpose of removing a significant fraction of the potentially large background coming from $c\overline{c}$ processes. Selection on these variables provides good discrimination between signal and background and is particularly effective at removing the potentially troublesome $c\overline{c}$ background. The $B\overline{B}$ background and signal Monte Carlo is essentially flat in these variables whereas the continuum is strongly peaked at ± 1. Cutting on the $\cos\theta_{\vec{T},K}$ provides excellent background rejection while also maintaining a high signal efficiency. We choose to cut only on this quantity such that $|\cos\theta_{\vec{T},K}| < 0.8$.

6.6 Polar angle of Kaon candidate

The polar angle of the signal candidate track has been studied for use in the selection. No cut was made on this variable in the analysis. Figures 6.11 and 6.12 show scatter plots of polar angle versus p^*_K and E_{extra} respectively. We plot the background Monte

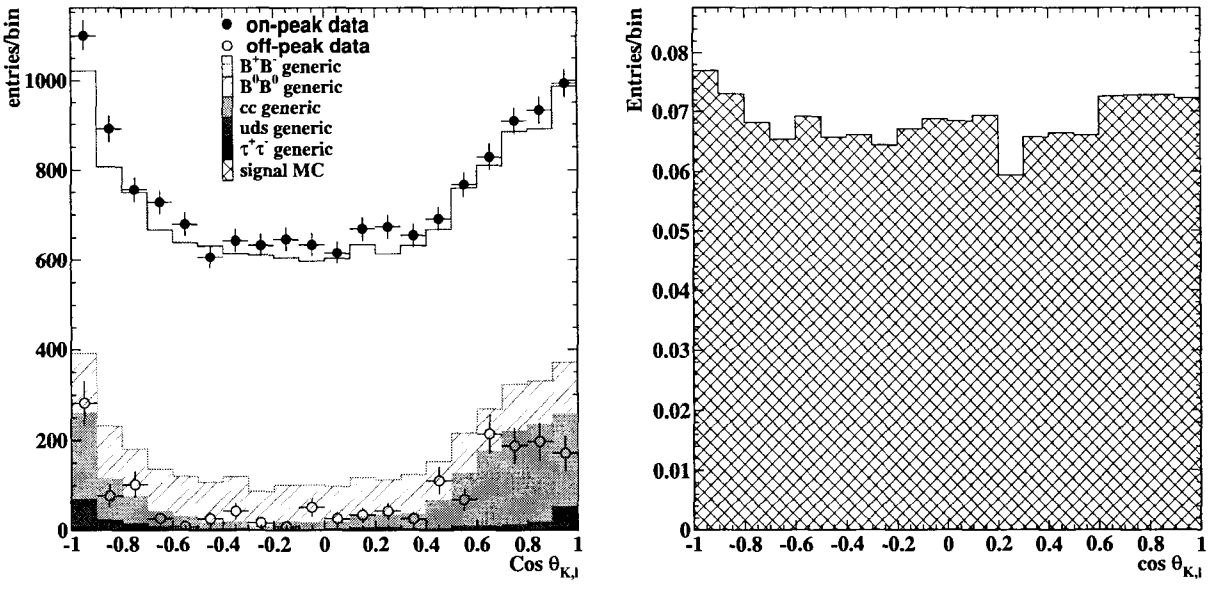

Figure 6.8: Cosine of the angle between the K and lepton used in the tag after the removal of the tag candidate tracks and clusters, cos $\theta_{K,\ell}$. All Monte Carlo contributions and data are plotted (left) with the signal Monte Carlo plotted (right) for comparison.

Carlo simulation events and signal Monte Carlo events for comparison. One can see that there are a number of high momentum kaons in the B^+B^- background events that populate the high polar angle region.

6.7 Optimization procedure

In the analysis we expect to have background events in the signal box and sideband events that we can use to estimate the background. The signal is thus

$$N_{\rm sig} = N_{\rm cand} - N_{\rm side} \times A \tag{6.1}$$

where $N_{\rm cand}$ is the total number in the signal box, $N_{\rm side}$ is the number in the sidebands, and A is a scale factor to account for the different areas of the signal box and sideband regions ($A = 7/3$ the way we form these regions). The statistical error on the signal is then

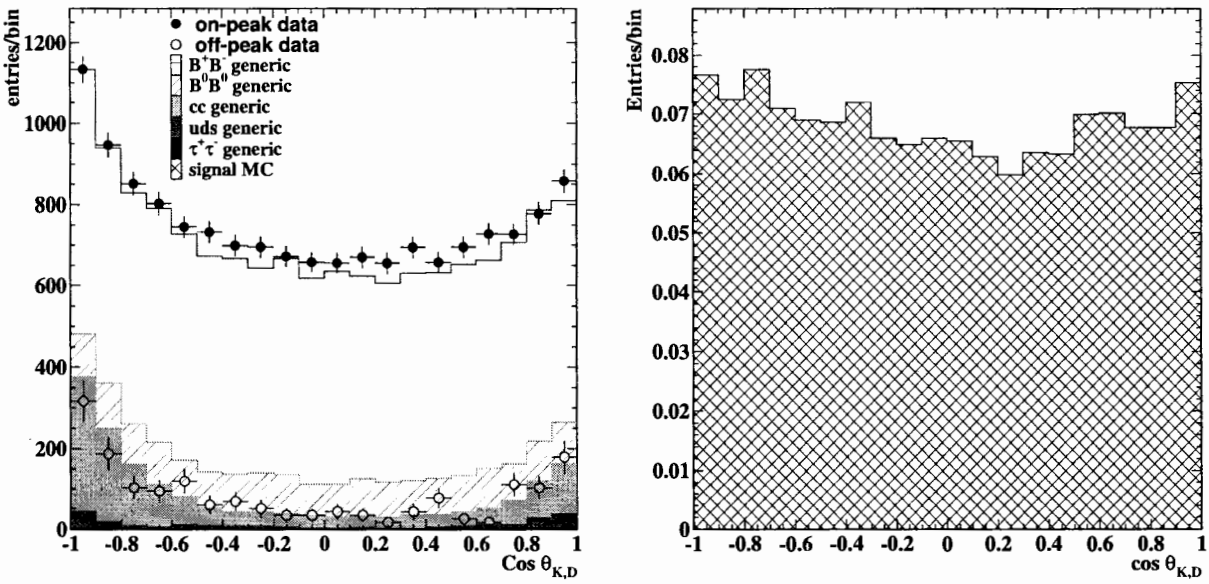

Figure 6.9: Cosine of the angle between the K and D meson used in the tag, $\cos\theta_{K,D^0}$. All Monte Carlo contributions and data are plotted (left) with the signal Monte Carlo plotted (right) for comparison.

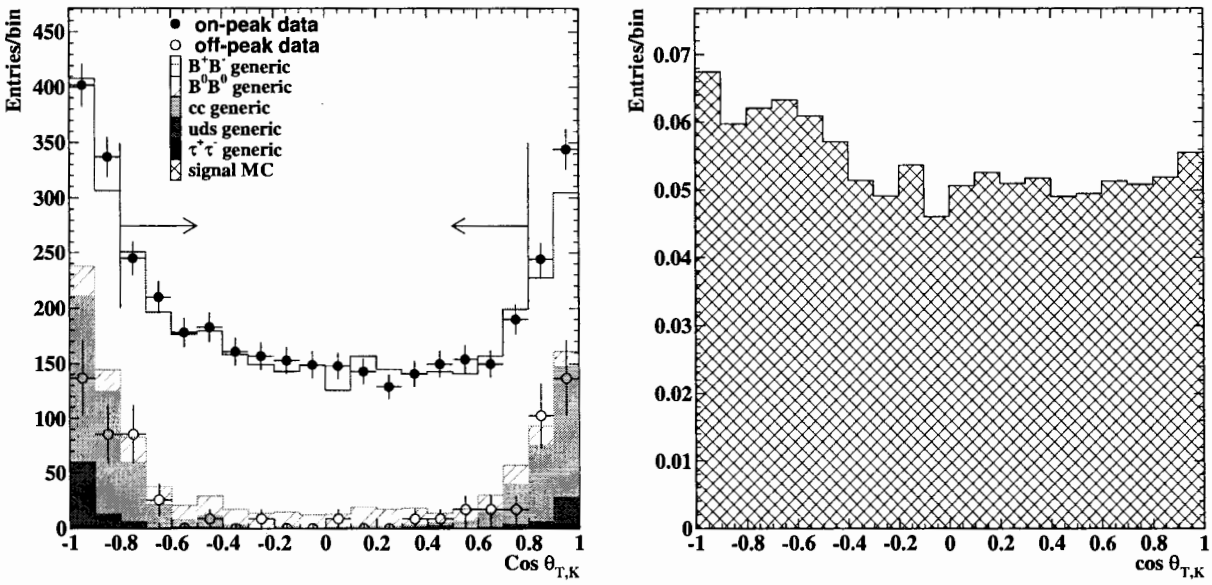

Figure 6.10: Cosine of the angle between the K and thrust axis of the rest of the event, $\cos\theta_{\vec{T},K}$. All Monte Carlo contributions and data are plotted (left) with the signal Monte Carlo plotted (right) for comparison.

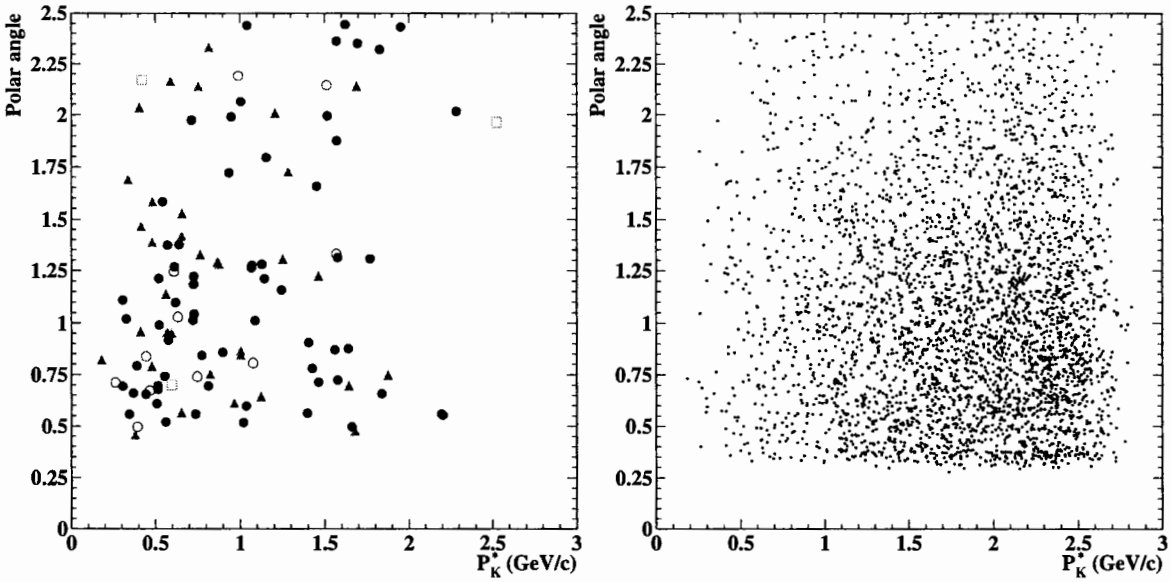

Figure 6.11: Scatter plots of the polar angle, θ, versus momentum of the kaon candidate in the signal region. Generic B^+B^- are symbolised by solid (blue)circles, $B^0\overline{B}^0$ by the open (red)circles and $c\overline{c}$ by the open (green)squares. On-peak data are plotted as solid(magenta) triangles. Signal Monte Carlo for $B^+ \to K^+\nu\overline{\nu}$ is plotted on the right.

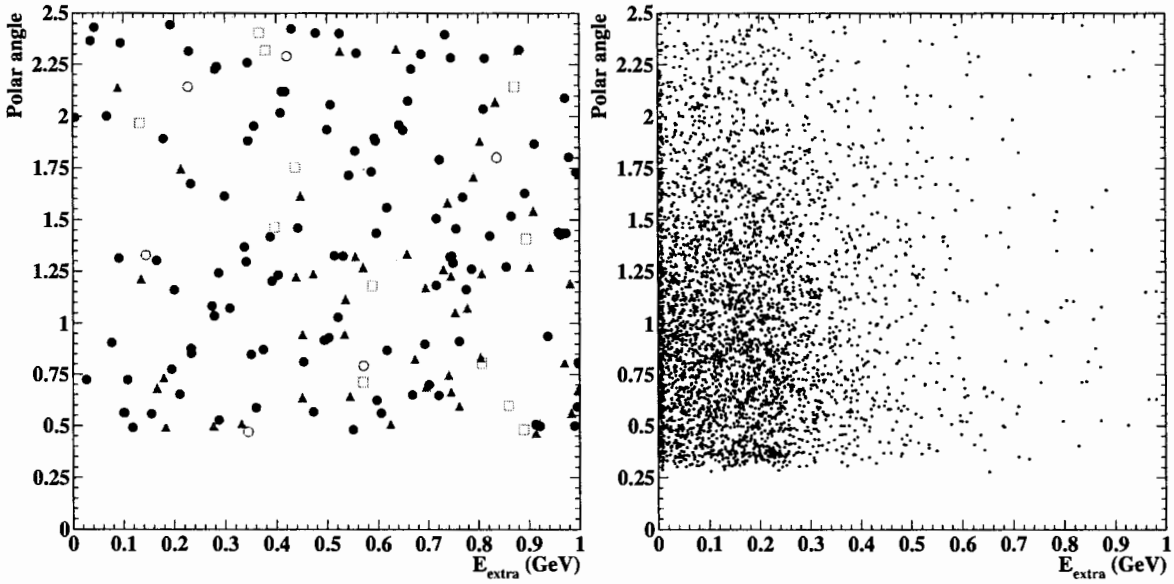

Figure 6.12: Scatter plots of the polar angle, θ, versus E_{extra} of the kaon candidate in the signal region. The same symbols are used as in Figure 6.11.

$$\sigma_{\rm sig} = \sqrt{(N_{\rm cand} + A \times A \times N_{\rm side})} \tag{6.2}$$

Assuming the scaled sideband yield is equal to the signal box yield, we expect a net signal of $0 \pm \sigma_{\rm sig}$. We then turn this into a branching fraction(BF) using

$$BF = \frac{N_{\rm sig}}{N(B^+B^-) \times \epsilon}, \tag{6.3}$$

where ϵ is the efficiency, so that the uncertainty in the BF is

$$E_{\rm BF} = \frac{\sigma_{\rm sig}}{N(B^+B^-) \times \epsilon}. \tag{6.4}$$

We ignore the fractional uncertainty in the efficiency, which will be small in comparison to $\sigma_{\rm sig}/N_{\rm sig}$. We therefore choose cuts that minimize $\sigma_{\rm sig}/\epsilon$. This is the same as choosing to minimize $\sqrt{B}/S$, where B are the number of background events predicted in the MC and S is the yield of signal events in the $B^+ \rightarrow K^+\nu\overline{\nu}$ signal MC sample. Hence this optimization is just the normal $\sqrt{S+B}/S$ in the small signal limit, i.e. when $B >> S$.

Using this prescription we optimize a number of variables. We choose to do a simple one-dimensional optimization where all other selection criteria in the analysis chain are imposed aside from the quantity being plotted. This procedure was iterated until the value was minimized (in practice only one or two iterations of the cuts was required). The results of this are shown in figure 6.13. We choose to cut on the values minimized by this procedure and have chosen these selection criteria throughout the remainder of the analysis chain. It should be noted that only a small gain can be made by vetoing K_L^0 candidates. We plot the optimization plots for EMC and IFR K_L^0's on a similar scale to the E_{extra} and $\rm p^*_{tag\ lepton}$ plots to show that there is little gain to be made wherever a cut is applied. It was decided therefore, that cuts would not be applied to these variables due to both the limited gain, and to avoid the complication of evaluating systematics associated with them.

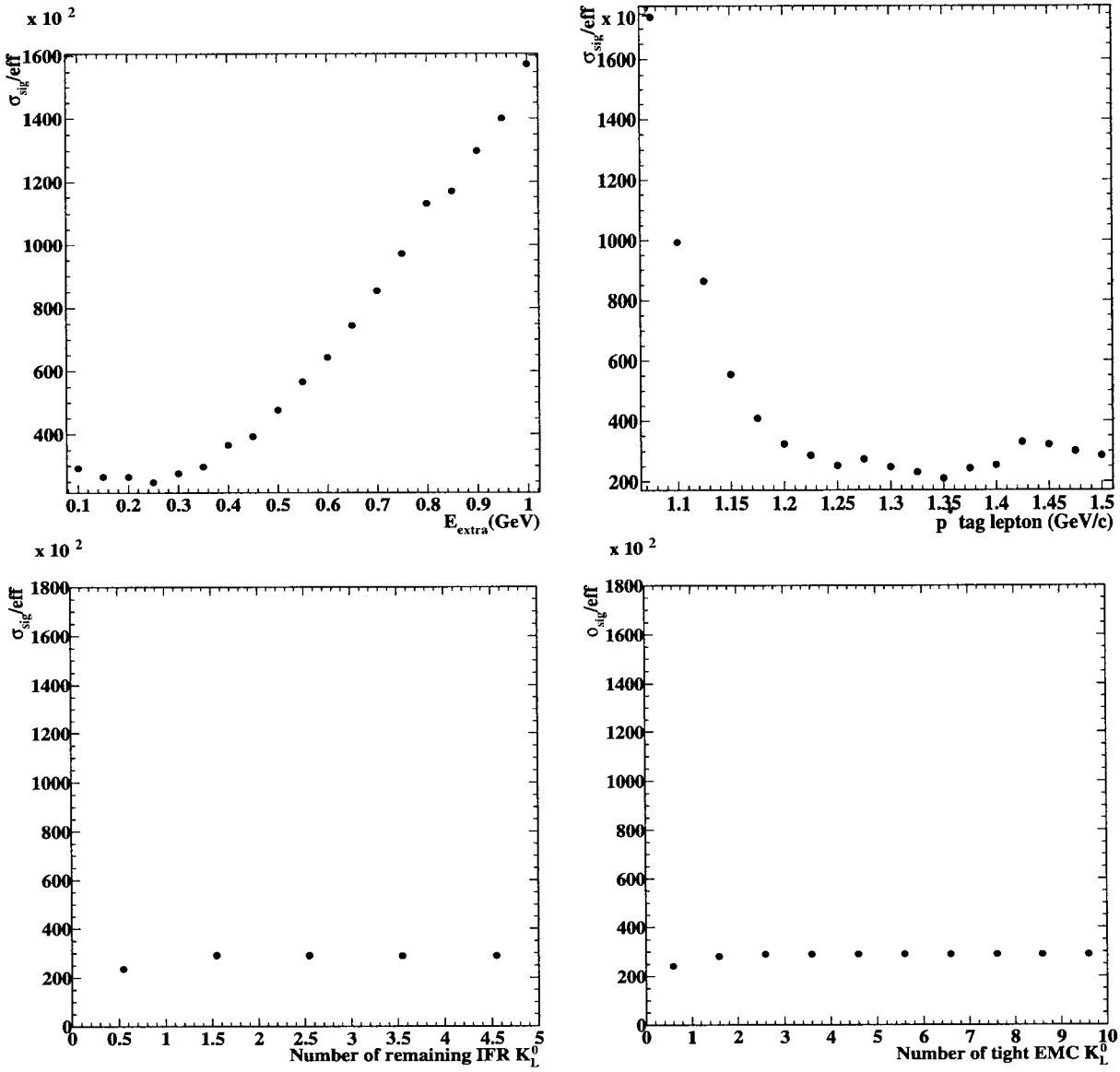

Figure 6.13: $E_{\rm sig}/\epsilon$ (as defined in the text) is plotted for E_{extra}, $\mathrm{p}^*_{\rm tag\ lepton}$ and Number of tight K^0_L candidates.

6.8 Form-factor correction

The signal Monte Carlo is generated according to a phase-space model, as a result the kaon momentum spectrum is not expected to be correctly modeled. In order to obtain an improved estimate of the signal efficiency, the momentum spectrum is re-weighted according to the model described by [19] and the simulated efficiency is corrected accordingly. The $\nu\overline{\nu}$ invariant mass squared distribution obtained from the Monte Carlo and theory models are compared in figure 6.14. Monte Carlo events are individually reweighted in bins of $m_{\nu\overline{\nu}}$ in order to compensate for any effects such as the momentum dependence of the tracking efficiency and kaon particle identification. This reweighting results in a slight reduction in the signal efficiency ϵ_{sig} of approximately $4\% \pm 3\%$. The systematic uncertainty quoted comes from the largest total change in efficiency resulting from reweighting using the various models quoted in [19] and hence should the most conservative estimate. This model enables us to evaluate a bin–by–bin correction and to extract a systematic uncertainty and hence was the preferred model. Another theoretical distribution was found in the literature in [20]. It was found that there was no significant effect on the limit from the phase–space model when reweighting with this model. No other theoretical models for the Standard Model $B^+ \rightarrow K^+\nu\overline{\nu}$ distribution could be found in the literature.

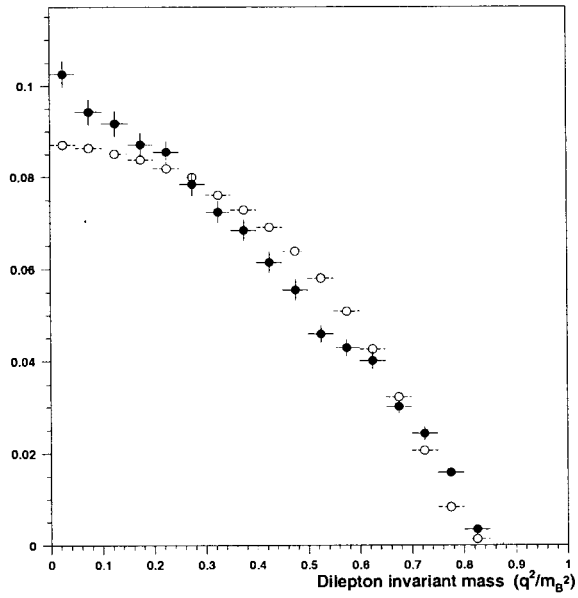

Figure 6.14: The $\nu\overline{\nu}$ invariant mass squared distribution is plotted for $B^+ \to K^+\nu\overline{\nu}$ signal Monte Carlo (solid points) along with the Standard Model theory prediction (open points) taken from [19]. Both curves are normalized to give equal area.

Chapter 7

Sidebands and Signal region

In order to study the agreement between data and simulation we define a set of sidebands and a signal region. The signal region remains blind while the sideband distributions can be studied for potential shape and yield discrepancies. Ultimately we rely on the sideband samples to guide our degree of belief that the simulation is a good model of the data in the region of phase space of particular interest to our analysis. In this chapter we will describe the sideband samples we study and motivate their choice and definition. The plots and tables given will show the level to which data and simulation agree. Furthermore we describe the criteria used in the selection of a suitable signal box.

In all of the sidebands we studied, and in the signal region, the Monte Carlo simulation has been scaled to the luminosity of the data sample.

7.1 Blind analysis

In order to avoid the possibility of biasing the selection procedure, a blinding–region is defined in the E_{extra}–D^0 mass plane surrounding what we define as the signal region. Data within this region remain hidden from the experimenters. The blinding–region spans E_{extra} <1.0 GeV and $\pm 10\sigma$ from the nominal D^0 mass. This encompasses the

regions defined as the E_{extra} sideband, D^0 mass sideband and signal region in section 7.2. The strategy applied to unblinding these regions is described in section 7.4. The use of sidebands in this analysis is critical to be able to understand the agreement between the data and simulation in various regions of phase–space. It will be this reliance on sidebands that will guide the decision of whether to look in the blinded regions. Therefore it is critical that the selected sidebands cover regions where the agreement between data and simulation is inherently good. Furthermore, it is useful to look separately at regions where the backgrounds are either combinatoric in nature or dominated by $B\overline{B}$ processes.

7.2 Sideband studies

The sidebands that are studied provide us with information about regions of phase space similar to that in which we will search for signal candidate events.
Examining distributions of the variables shown in chapter 6 leads us to the sideband definition given in table 7.1.

Since the E_{extra} distribution is one of the most sensitive variables to our signal candidate yield it seems reasonable to study several regions of the entire E_{extra} spectrum. Figures 7.1, 7.2 and 7.3 show sidebands used to compare Monte Carlo and data in specific regions similar to the signal region. These distributions show data/Monte Carlo comparisons in the E_{extra} variable for the three-track, two-track and big E_{extra} sidebands respectively (as defined in table 7.1). In the case of the two(three)-track sideband we require there to be one(two) additional charged tracks other than the signal candidate track. In figures 7.1 and 7.2 these two distributions are plotted for the E_{extra} spectrum between 0 and 3.0 GeV. To compare these yields quantitatively between data and simulation we look only at the yield in the region $E_{extra} < 0.25$ GeV.

Table 7.1: Definition of signal box and sidebands.

	Signal Region	E_{extra}	Big E_{extra}	2-track	3-track
E_{extra}(GeV)	< 0.25	$> 0.25, < 1.0$	$> 1.0, < 2.5$	≤ 0.25	≤ 0.25
p^*_K (GeV/c)	> 1.25	> 1.25	> 1.25	> 1.25	> 1.25
Number of tracks (on signal side)	1	1	1	2	3
Kaon Id	tight	tight	tight	tight	tight
$\lvert\cos\theta_{\vec{T},K}\rvert$	<0.8	<0.8	<0.8	<0.8	<0.8

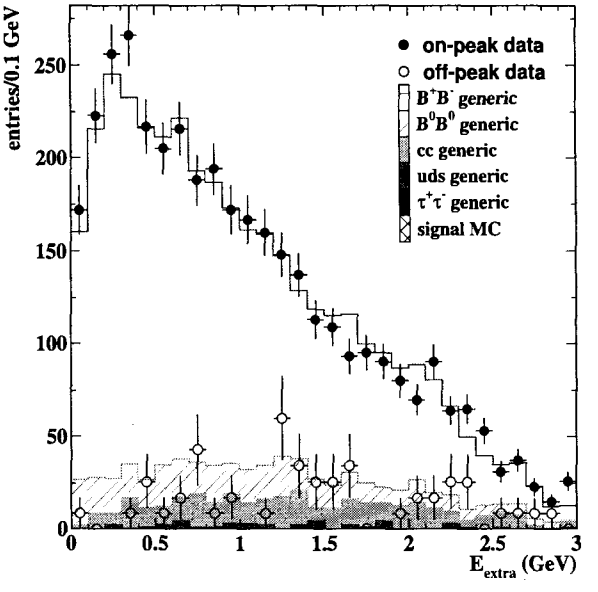

Figure 7.1: Here we demand the same final selection cuts as in the signal region but loosen the selection to allow for two additional charged tracks as well as the signal candidate kaon and $E_{extra} \leq 3.0$ GeV. This corresponds to the three-track sideband outlined in table 7.1.

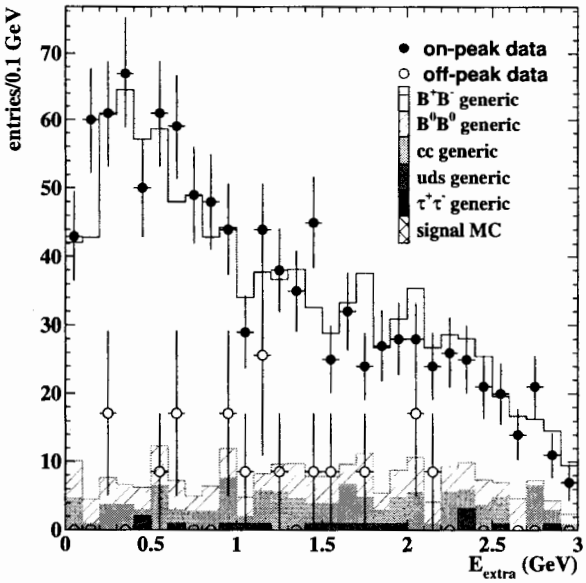

Figure 7.2: Here we demand the same final selection cuts as in the signal region but loosen the selection to allow for a second charged track as well as the signal candidate kaon and $E_{extra} \leq 3.0$ GeV. This corresponds to the two-track sideband outlined in table 7.1.

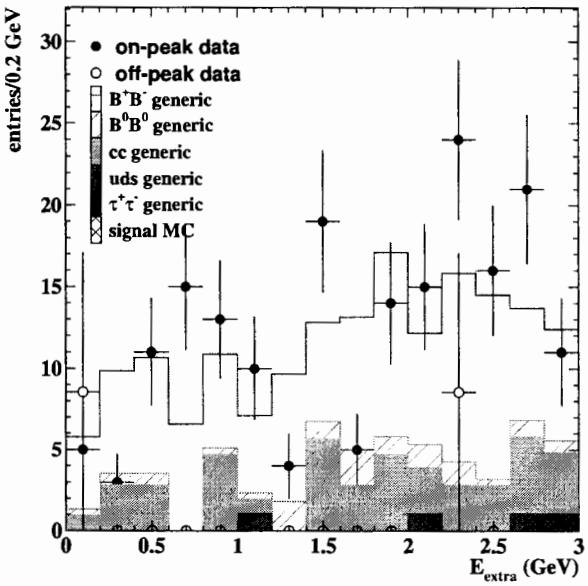

Figure 7.3: The same final selection cuts as in the signal region are demanded for this plot. The region between $1.0 < E_{extra} < 2.5$ GeV corresponds to the Big E_{extra} sideband outlined in table 7.1.

Table 7.2: Definition of the D^0 mass sidebands.

D^0 decay mode	lower sideband	upper sideband
All modes	M(D^0) - $10\sigma \rightarrow$ M(D^0) - 3σ	M(D^0) + $3\sigma \rightarrow$ M(D^0) + 10σ

7.3 D^0 mass sidebands

The three and two-track sidebands are also studied in the D^0 mass distribution. These are plotted in figures 7.4 and 7.5. We can see that the combinatorial component of the background is flat in these plots. Hence the requirement of a high momentum kaon and low missing energy is reducing the effect of any combinatorial peaking component from the signal region if one compares figue 7.5 with figure 7.6. Since demanding only a single track in the signal region further reduces this background we decide to scale and subtract the combinatorial background from the D^0 mass sidebands in the signal region.

Therefore we define sidebands in the D^0 mass spectrum in order to compare the data and Monte Carlo distributions outside of the requirements imposed on the tagging side for signal events Doing this provides a cross-check as to how well the data and Monte Carlo agree in the signal regions and an example of the amounts of background present in each. Furthermore, since we subtract the sidebands from the signal box region as is outlined in section 7.4 we need to extract the yields for both data and Monte Carlo. Figure 7.6 shows the sideband regions which are defined in table 7.2 where the distributions are scaled according to the data sample luminosity. The distributions are separated by D^0 decay mode for clarity and we see reasonable agreement (for the

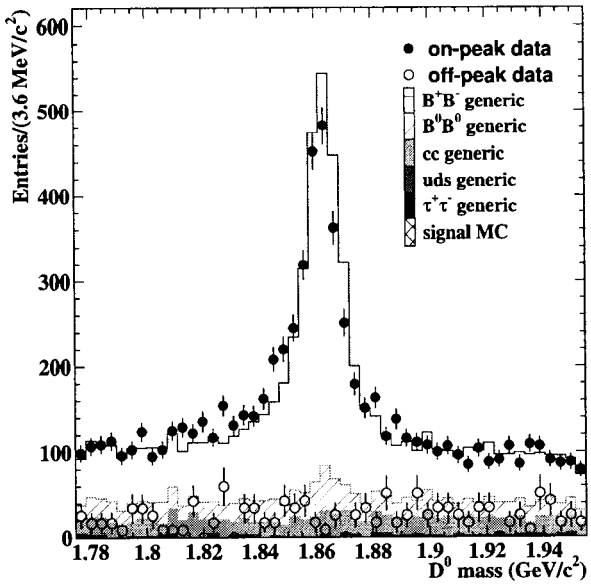

Figure 7.4: Here we demand the same final selection cuts as in the signal region but loosen the selection to allow for up to three charged tracks, including the signal candidate kaon.

loose cuts applied) between data and Monte Carlo in all modes in both the signal and sideband regions.

7.4 Signal region

A suitable distribution in which to plot the signal and sideband regions can be defined in the D^0 mass vs E_{extra} plane.

Table 7.6 presents a breakdown of the yields in the two and three track sidebands as defined in table 7.1. We see that the data and simulation agree well from the yields we extract and the Monte Carlo yields are as expected with the B^+B^- events dominating.

Figure 7.7 shows the definitions of the sideband and signal regions with the $B^+ \rightarrow K^+\nu\overline{\nu}$ Monte Carlo simulation overlayed. The plot shows the number of sigma from

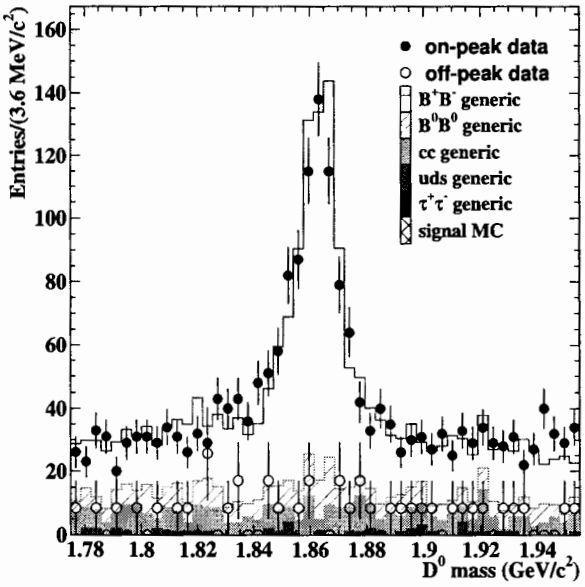

Figure 7.5: Here we demand the same final selection criteria as in the signal region but loosen the selection to allow for a second charged track as well as the signal candidate kaon.

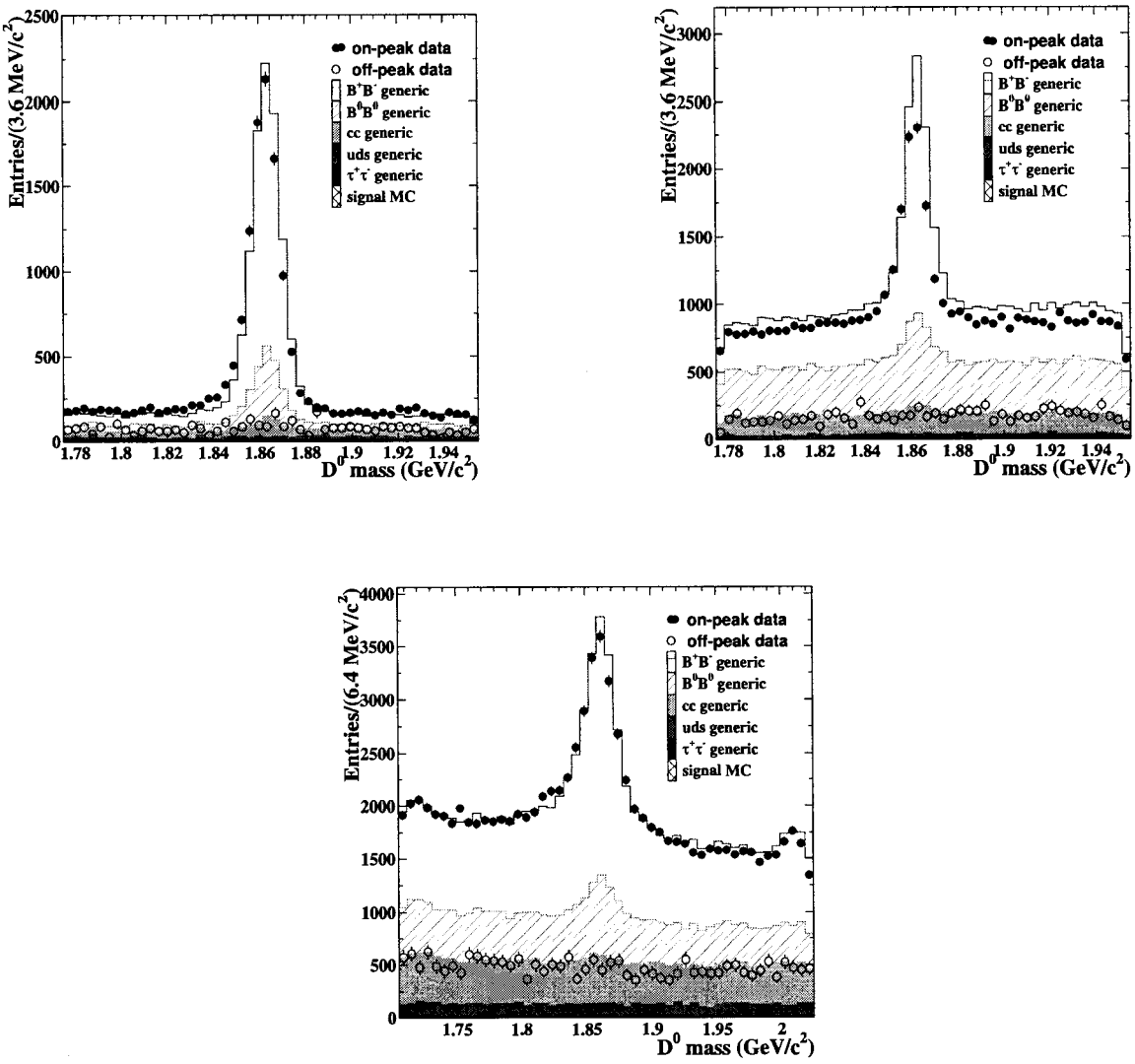

Figure 7.6: The D^0 mass distribution with sideband regions included. Each mode is plotted separately using all Monte Carlo ($B\overline{B}$, $q\overline{q}(q = u, d, s$ or $c)$ and $\tau^+\tau^-$), onpeak and offpeak data. All distributions are scaled to the onpeak data luminosity. The upper left plot, upper right plot and lower plot correspond to the $K^-\pi^+$, $K^-\pi^+\pi^+\pi^-$ and $K^-\pi^+\pi^0$ modes respectively.

the mean of the D^0 mass distribution versus the left over neutral energy. The signal box and big E_{extra} sideband contain events with a $\pm$ 3σ window in the D^0 mass. These definitions are examined after all other selection criteria from table 7.1 except that on E_{extra} are applied. The procedure then begins with comparing the yields in Monte Carlo and data in the big E_{extra} sideband. It is expected that there should be an equal (or comparable) number of events in this sideband, within experimental uncertainty, for data and Monte Carlo. This is explained in further detail in section 7.6 with table 7.7 providing the numbers of total events in each sideband for comparison. From the signal box yield in the MC the number of expected signal events in the data can be estimated. Prior to unblinding the signal box in data, the E_{extra} sideband is unblinded as a final cross check. The unblinding strategy can be summarised as follows:

1. Apply all selection criteria, except E_{extra}, and compare data–Monte Carlo yield in the big E_{extra} sideband.

2. When satisfied with the big E_{extra} sideband data–Monte Carlo agreement proceed by unblinding the E_{extra} region.

3. A final cross–check is done by comparing the E_{extra} sideband. If the data–Monte Carlo agreement is good there then signal region and D^0 mass sidebands are unblinded, the scaled D^0 mass sideband yields are subtracted from the signal region yield. This yield is then used to extract the upper limit.

Figure 7.8 shows the signal box and E_{extra} sidebands as defined in figure 7.7 for the assorted background Monte Carlo distrbutions.

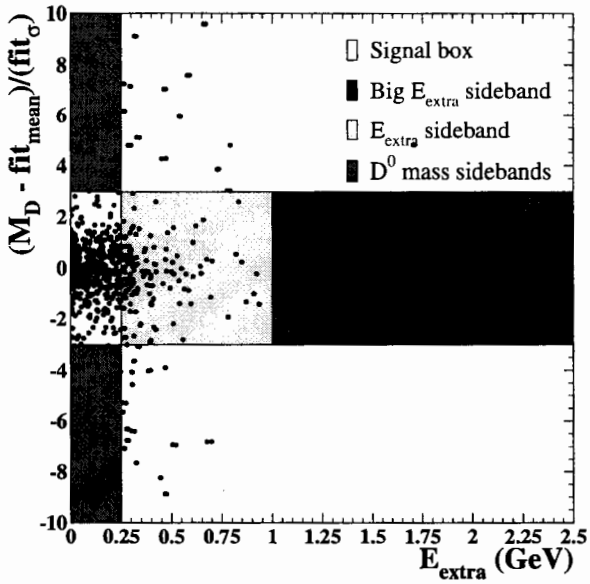

Figure 7.7: The signal and sideband region definitions with $B^+ \rightarrow K^+\nu\overline{\nu}$ signal Monte Carlo overlayed. The y axis corresponds to the number of sigma from the mean of the D^0 mass and the x axis is E_{extra}..

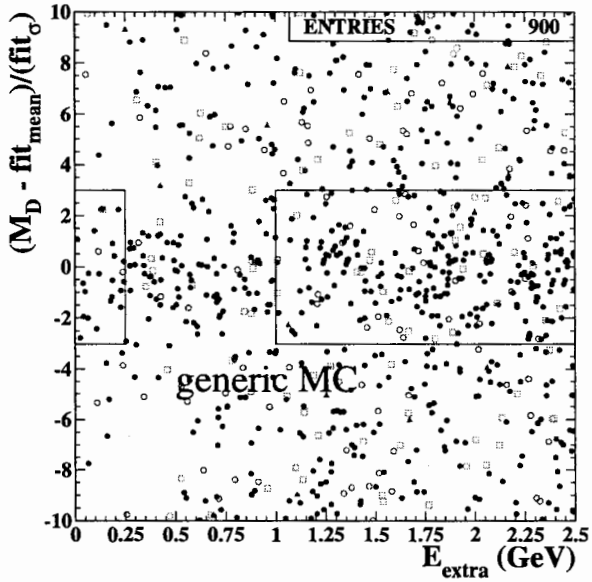

Figure 7.8: The signal and sideband regions for all generic Monte Carlo. The Monte Carlo is split up by type into B^+B^-(solid (blue) circles), $B^0\overline{B}^0$(open (red) circles), $c\bar{c}$(open (green) squares) and uds(solid (red) triangles). No scaling is applied to this distribution.

7.5 Cut flow tables

The following selection criteria are imposed for the $B^+ \to K^+\nu\overline{\nu}$ signal search:

- one signal side track which satisfies tight K identification;
- $|\cos\theta_{\vec{T},K}| < 0.8$;
- $p_K^* > 1.25$ GeV/c;
- $E_{extra} < 0.25$ GeV.

In order to study the impact of individual criteria in the context of the overall selection we produce a number of cut flow tables. These are a convenient way to compare the effective efficiencies and yields of data and simulation at different stages in the selection. The 'primordial' selection refers to the number of events used in the analysis. 'Precuts' refers to the selection of a suitable tag $B^- \to D^0\ell^-\overline{\nu}\,X$ candidate. Both the marginal and cumulative efficiencies are given. The cumulative gives the efficiency of all selection criteria up to that point. The marginal is the efficiency of each criteria compared to the previous selection criteria.

Table 7.3 shows the cut-flow for signal Monte Carlo. The yield given in the precuts row is consistent with that quoted in table 5.3. The efficiency has been corrected by various factors to account for known drawbacks in the simulation. Corrections are applied to the tagging efficiency, p_K^* and E_{extra}. The premise for imposing such corrections is that the signal Monte Carlo is not necessarily a good reflection of the data which we study when searching for signal candidates. The correction factors included in table 7.3 are extracted using a "double-tag" technique which is described in detail in chapter 8. This provides a means of accounting for any differences between

the tag efficiency in data and simulation, where the ratio of the two is taken as the correction factor to the tag efficiency.

In table 7.4 contributions from each of the Monte Carlo sources is shown. All of the quantities therein have been scaled to the on-peak data set luminosity. The final lines of each section of table 7.4 show the Monte Carlo contribution from each of the individual sources to the sideband and signal regions. Sideband and signal region definitions are given in table 7.1. Table 7.5 shows the same information as table 7.4 for the on and off-peak data, background and continuum Monte Carlo. The continuum Monte Carlo is $c\bar{c}$, $\tau^+\tau^-$ and uds all scaled to the off-peak luminosity. The background Monte Carlo is the summation of all contributions given in table 7.4. From these two tables we can compare sideband yields in the E_{extra} and D^0 mass sidebands and this information has been gathered in table 7.7.

7.6 Event Yield

The event yields in Monte Carlo and data can be extracted from tables 7.4 and 7.5 and are summarised in tables 7.6 and 7.7. These comparisons show good agreement between data and Monte Carlo in the big E_{extra} sideband for both on-peak and off-peak data. The yields in the D^0 mass sidebands are also compared. The unblinding procedure was outlined in section 7.4. Chapter 10 describes in greater detail the procedure for extracting the result based on the number of observed events and the consistency with the number of expected events in the signal box.

Table 7.3: Cut-flow table for signal Monte Carlo where all numbers are unscaled. A correction is applied to the efficiency calculation where applicable. The corrections applied to Ntrkleft=1 and E_{extra} are described in section 8.2. The correction to p^*_K comes from reweighting the signal Monte Carlo distribution as mentioned in section 7.5.

	signal Monte Carlo		
Cut	Yield	Marginal efficiency	Cumulative efficiency
primordial	2.38×10^6	-	-
precuts	12620	(5.30×10^{-3})	
Ntrkleft=1	8758	0.69	
corrected efficiency	1.078	0.75	0.7460
Kaon PID	6165	0.70	0.5251
$\cos\theta_{\vec{T},K}$	4829	0.78	0.4113
p^*_K	3917	0.81	0.3337
corrected efficiency	0.96	0.78	0.3203
signal box	2927	0.75	
corrected efficiency	0.967	0.72	0.2315
D^0 mass sideband	423	–	–
E_{extra} sideband	926	–	–

Table 7.4: Cut-flow table for B^+B^-, $B^0\overline{B}^0$, $c\bar{c}$ and uds Monte Carlo all scaled to the data set luminosity. The precuts line counts all event passing those selection criteria outlined in table 5.2. Each of the selection criteria in the table are then applied successively. The marginal efficiency of the precuts is the number passing the precuts divided by the primordial number of entries into the original sample considered.

	B^+B^-			$B^0\overline{B}^0$		
Cut	Yield	Marginal efficiency	Cumulative efficiency	Yield	Marginal efficiency	Cumulative efficiency
primordial	0.43×10^8	-	-	0.43×10^8	-	-
precuts	337616	-	-	205794	-	-
Ntrkleft=1	7891	0.023	0.023	2415	0.012	0.012
Kaon PID	619	0.078	1.83×10^{-3}	120	0.050	5.82×10^{-4}
$\cos\theta_{\vec{T},K}$	471	0.762	1.40×10^{-3}	89	0.740	4.31×10^{-4}
p_K^*	123	0.261	3.65×10^{-4}	14	0.161	6.95×10^{-5}
Big E_{extra} sideband	61	0.498	1.81×10^{-4}	10	0.675	4.69×10^{-5}
D^0 mass sideband	3.9	0.032	1.17×10^{-5}	1.8	0.125	8.69×10^{-6}
2-track sideband	98.6	0.801	2.92×10^{-4}	10.7	0.750	5.22×10^{-5}
3-track sideband	423.4	3.440	1.25×10^{-3}	54.4	3.800	2.642×10^{-4}
E_{extra} sideband	24.2	0.197	7.17×10^{-5}	1.4	0.100	6.95×10^{-6}
signal box	6.1	0.049	1.79×10^{-5}	0.7	0.050	3.48×10^{-6}
	$c\bar{c}$			uds		
Cut	Yield	Marginal efficiency	Cumulative efficiency	Yield	Marginal efficiency	Cumulative efficiency
primordial	1.07×10^8	-	-	1.72×10^8	-	-
precuts	70670	-	-	22516	-	-
Ntrkleft=1	3205	0.045	0.045	837	0.037	0.037
Kaon PID	489	0.153	6.92×10^{-3}	95	0.114	4.23×10^{-3}
$\cos\theta_{\vec{T},K}$	243	0.497	3.44×10^{-3}	24	0.256	1.08×10^{-3}
p_K^*	52	0.214	7.36×10^{-4}	6	0.261	2.82×10^{-4}
Big E_{extra} sideband	22	0.418	3.08×10^{-4}	2.1	0.333	9.40×10^{-5}
D^0 mass sideband	3.8	0.073	5.35×10^{-5}	0.0	0.000	0.000
2-track sideband	8.5	0.164	1.20×10^{-4}	0.0	0.000	0.000
3-track sideband	15.1	0.291	2.14×10^{-4}	1.1	0.167	4.70×10^{-5}
E_{extra} sideband	10.4	0.200	1.47×10^{-4}	0.0	0.000	0.000
signal box	0.9	0.044	1.34×10^{-5}	0.0	0.000	0.000

Table 7.5: Cut-flow table for on-peak data, off-peak data, all background and continuum background. The numbers in all tables have been scaled correspondingly to either the on or off-peak data sample luminosity. All background Monte Carlo is a sum of all on-peak contributions given in table 7.4

	on-peak data			background Monte Carlo		
Cut	# pass	Marginal efficiency	Cumulative efficiency	# pass	Marginal efficiency	Cumulative efficiency
primordial	4.42×10^{8}			4.41×10^{8}	-	-
precuts	664188	-	-	637321	-	-
Ntrkleft=1	16160	0.0243	0.0243	14663	0.0230	0.0230
Kaon PID	1524	0.0943	2.295×10^{-3}	1335	0.0911	2.095×10^{-3}
$\cos\theta_{\vec{T},K}$	926	0.6076	1.394×10^{-3}	828	0.6203	1.300×10^{-3}
p_K^*	213	0.2300	3.207×10^{-4}	196	0.2363	3.071×10^{-4}
Big E_{extra} sideband	100	0.4695	1.506×10^{-4}	95	0.4843	1.488×10^{-4}
D^0 sideband	8	0.0376	1.204×10^{-5}	9.5	0.0486	1.493×10^{-5}
2-track sideband	136	0.6385	2.048×10^{-4}	118	0.5889	1.849×10^{-4}
3-track sideband	537	2.5211	8.085×10^{-4}	494	2.5204	7.751×10^{-4}
E_{extra} sideband	41	0.1925	6.173×10^{-5}	36.0	0.1840	5.653×10^{-5}
signal box	6	0.0282	0.903×10^{-5}	7.7	0.0394	1.210×10^{-5}

	off-peak data			continuum Monte Carlo		
Cut	Yield	Marginal efficiency	Cumulative efficiency	Yield	Marginal efficiency	Cumulative efficiency
primordial	0.41×10^{8}	-	-	0.42×10^{8}	-	-
precuts	11801	-	-	10985	-	-
Ntrkleft=1	511	0.0433	0.0433	510	0.0464	0.0464
Kaon PID	63	0.1233	5.339×10^{-3}	70	0.1370	6.355×10^{-3}
$\cos\theta_{\vec{T},K}$	25	0.3968	2.118×10^{-3}	31	0.4496	2.857×10^{-3}
p_K^*	4	0.1600	3.390×10^{-4}	7	0.2175	6.214×10^{-4}
Big E_{extra} sideband	1	0.2500	8.474×10^{-5}	3	0.4089	2.541×10^{-4}
D^0 sideband	0	0.0000	0.0000	0.4	0.0648	4.027×10^{-5}
2-track sideband	0	0.0000	0.0000	1.0	0.1458	9.062×10^{-5}
3-track sideband	1	0.2500	8.474×10^{-5}	1.9	0.1458	1.730×10^{-4}
E_{extra} sideband	0	0.0000	0.0000	1.2	0.1782	1.108×10^{-4}
signal box	1	0.2500	8.474×10^{-5}	0.1	0.0162	1.007×10^{-5}

Table 7.6: Monte Carlo and data in the two-track and three-track sidebands. The sideband definitions are given in table 7.1.

Event Sample	two-track sideband	three-track sideband
B^+B^-	99.9±5.1	418.1±10.4
$B^0\overline{B}^0$	10.7±2.0	54.4±4.4
$c\overline{c}$	8.5±2.8	15.1±3.8
$\tau^+\tau^-$	0.0±0.0	0.0±0.0
uds	0.0±0.0	1.1±1.0
Total Monte Carlo	**115±6.2**	**491±12.0**
Total on–peak data	**136±11.7**	**537±23.2**
Total off–peak Monte Carlo	**1.0±1.0**	**1.9±1.4**
Total off–peak data	**0.0±0.0**	**1.0±1.0**

Table 7.7: Monte Carlo and data in the E_{extra} and D^0 mass sidebands. The sideband definitions are given in table 7.1.

Event Sample	E_{extra} sideband	Big E_{extra} sideband	D^0 mass sideband
B^+B^-	24.2±2.5	61±4.0	3.9±1.0
$B^0\overline{B}^0$	1.4±0.7	10±1.9	1.8±0.8
$c\overline{c}$	10.4±3.1	22±4.6	3.8±1.8
uds	0±0	2±1.4	0±0
$\tau^+\tau^-$	0±0	0±0	0±0
Total Monte Carlo	**36.0±4.0**	**95±6.5**	**9.5±2.2**
Total on–peak data	**41±6.4**	**100±10**	**8±2.8**
Total off–peak Monte Carlo	**1.2±1.1**	**2.8±1.7**	**0.4±0.6**
Total off–peak data	**0±0**	**1.0±1.0**	**0±0**

Chapter 8

Systematic uncertainties

8.1 Introduction

In order to correct for known discrepancies between the simulation and the data we must calculate correction factors and associated systematic uncertainties. First we note that the efficiency calculated in chapter 6 was done using signal Monte Carlo simulations, where one B is forced (at the generator level) to decay to the signal in question (note that the same will be true for the efficiency calculation in chapter 9). To account for uncertainties in branching fractions and the tag reconstruction efficiency, a control sample of events where all B daughters are assigned is used in order to compare data and simulation for the tagging efficiency and E_{extra}. This is described in section 8.2. Assigning a systematic uncertainty to the tagging efficiency accounts for uncertainties in tracking efficiency, particle and neutral identification (for all tag particles) and any other reconstruction effects in the tag B, while also accounting for uncertainties in branching fractions. A breakdown of the systematic uncertainties is given in section 8.3. The systematic uncertainty on the overall normalization is explained in section 8.3.1. Systematic uncertainties associated with the tag B are described in section 8.3.2. All other systematic uncertainties will be associated with

the signal candidate B and are described in section 8.3.3.

8.2 Double-tagged Events

The high tagging efficiency in the $B^- \to D^0 \ell^- \overline{\nu}\, X$ channel results in a sizeable number of events where both B decays are reconstructed in this mode and such events will be referred to herein as "double-tagged" events. This is the first time that double-tagged events have been used in $\Upsilon(4S) \to B\overline{B}$ decays and this represents the first instance where the yields of such events were determined for use in an analysis. Double-tagged events can be used to compare the data and simulation in various ways, as will be described in this section.

The selection of double-tagged events proceeds as follows. First, a check of the yield using all D^0 decay modes for both B decays is performed. The D^0 invariant masses must lie within 3σ of the mean of the fitted distribution. The $\cos\theta_{B,D\ell}$ variable of both B candidates must be greater than -2.5 and less than 1.1. The p* of the leptons must be greater than 1.35 GeV/c and there must be no additional charged tracks other than those associated with the two tags. Studying $B^+ \to \overline{D}^0 \ell^+ \nu(X)$ vs $B^- \to D^0 \ell^- \overline{\nu}\, X$ events where all D^0 decay modes ($D^0 \to K^-\pi^+$, $K^-\pi^+\pi^+\pi^-$ or $K^-\pi^+\pi^0$) are considered one extracts the distributions shown in figure 8.1. Taking the yields from B^+B^- and $B^0\overline{B}^0$, adding the small number of double–tags from continuum events, and scaling them all to the dataset luminosity gives:

$$N_{B^+B^-} = 2293 \cdot \frac{81.9\,\mathrm{fb}^{-1}}{311.4\,\mathrm{fb}^{-1}} = 603 \tag{8.1}$$

$$N_{B^0\overline{B}^0} = 153 \cdot \frac{81.9\,\mathrm{fb}^{-1}}{229.0\,\mathrm{fb}^{-1}} = 55 \tag{8.2}$$

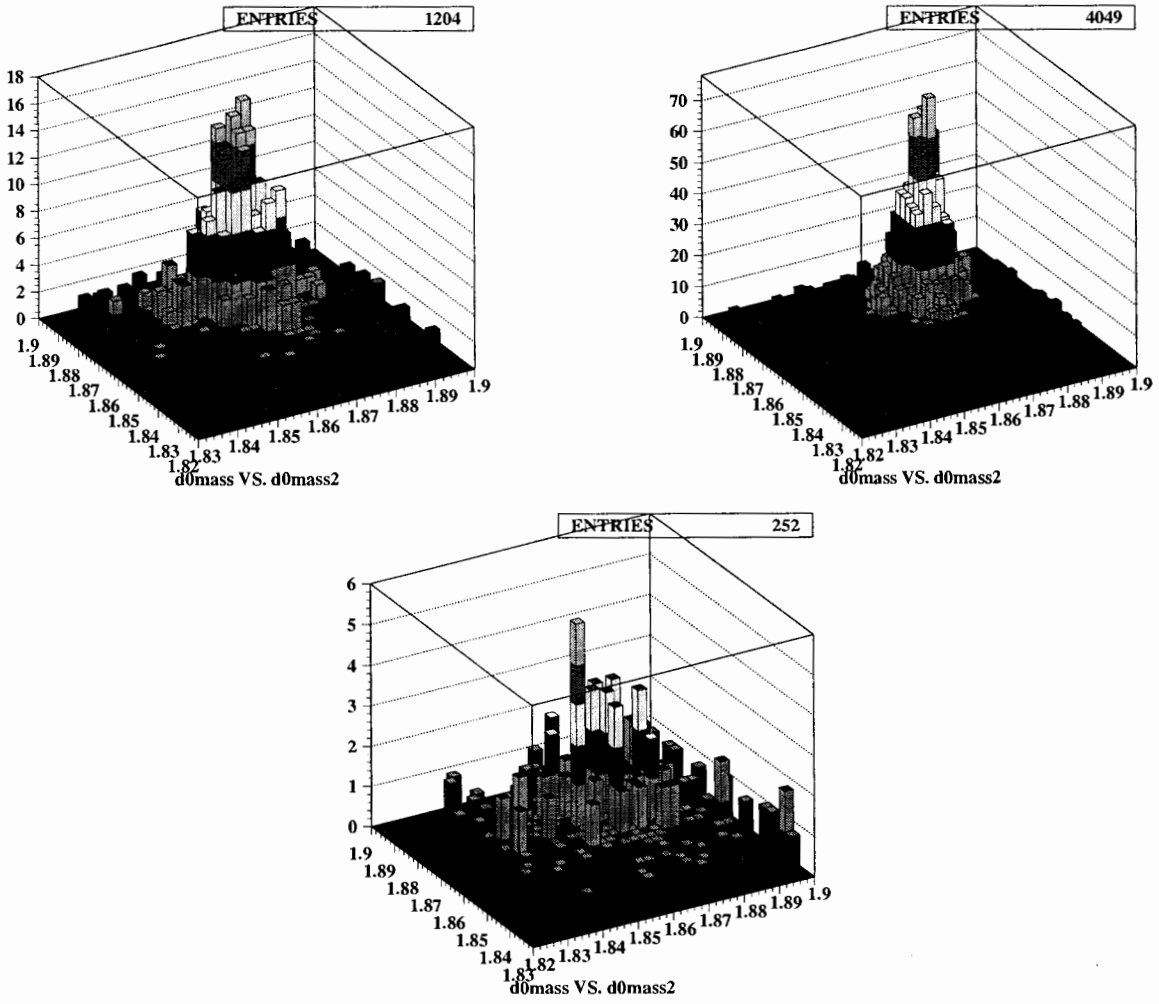

Figure 8.1: Distributions of the D^0 mass from one tag candidate plotted against the D^0 mass for the second tag candidate. On-peak data(left), B^+B^-(right) and $B^0\overline{B}^0$(centre) are plotted. None of the distributions have been scaled and the yields are described in the text.

$$N_{c\bar{c}} = 6 \cdot \frac{81.9\,\mathrm{fb}^{-1}}{86.6\,\mathrm{fb}^{-1}} = 6 \tag{8.3}$$

$$\begin{aligned} N_{\text{data doubletags}} &= 740 \pm 27 \\ N_{\text{Monte Carlo doubletags}} &= 664 \pm 14 \end{aligned}$$

Therefore, data/All Monte Carlo = 740/664 = 1.114±0.047 As can be seen from this comparison, the agreement between data and simulation is reasonably good. Under the assumption that the probabilities of selecting each D^0-ℓ in the double–tag event are identical we can easily calculate the number of expected double–tags. Using the tag efficiency given in table 5.3 we can use the simple expression,

$$N_{\text{doubletags}} = \epsilon^2 \cdot N_{B^+B^-} \tag{8.4}$$

where ϵ is the tag efficiency (which must be multiplied by the factor for having zero charged tracks left other than those assigned to the tag B).
This yields $N_{\text{doubletags}}$=594±12.3 events, which is consistent with what was observed from the B^+B^- Monte Carlo.

A second method of double-tagging exploits the intrinsic cleanliness of the $D^0 \rightarrow K^-\pi^+$ mode. In this case the double tags studied are required to include at least one decay in this mode, hereafter referred to as a $(K^-\pi^+)\ell$ candidate. In each event we search for two distinct, independent (non-overlapping) double-tagged decays, one of which must be a $(K^-\pi^+)\ell$ candidate. Hence, only two candidates that do not share any particles are considered. If more than two independent $D\ell\nu$ candidates exist in an event the two with the smallest values of $|cos\theta_{\mathrm{B}-(\mathrm{K}^-\pi^+)\ell}|$ are retained. Although one of the B's must be reconstructed in the $(K^-\pi^+)\ell$ mode the other B

decay is searched for in any of the 3 D^0 decay modes considered in the analysis. By considering the $(K^-\pi^+)\ell$ candidate as our 'signal' mode in this case we are able to extract a $B^- \to D^0\ell^-\overline{\nu}\ X$ tagging efficiency from both data and simulation. Using the data and full simulation allows the tagging efficiency to be calculated in a more realistic environment than is permitted by using signal Monte Carlo alone. Such a calculation then allows us to weight the tagging efficiency from signal Monte Carlo accordingly to account for any data/Monte Carlo differences.

The ratio,

$$\frac{(K^-\pi^+)\ell \text{ vs } D\ell\nu}{(K^-\pi^+)\ell \text{ vs generic } B} \tag{8.5}$$

enables a net efficiency for the tag to be extracted. The data/Monte Carlo ratio of this ratio then provides an independent correction to the tag efficiency.

One important factor to consider in this case is whether or not to impose a restriction on the number of charged tracks remaining after finding the single–tag or double–tag. One can see from equation 8.5 that imposing different constraints on the multiplicity after selecting single and double–tagged events would introduce an inherent bias into the technique. The ratio would then include factors other than that which is under investigation. Clearly this is not the correct thing to do. Indeed, any criteria imposed on the charged track (or neutral) multiplicity would introduce a dependence on how well modelled the multiplicity is. To avoid any such issues we choose to place no cut on the number of charged tracks in the event that are not assigned to the $B^- \to D^0\ell^-\overline{\nu}\ X$ candidate(s). This provides us with the correction we wish to extract. The assumption that the yields are dominated by only B^+B^- events is no longer valid since $B^0\overline{B}^0$ and $c\overline{c}$ also contribute significantly to the single tag yield. We extract the following yields, where a breakdown of the detailed contri-

Table 8.1: Comparing Monte Carlo and data in the inclusive $(K^-\pi^+)\ell$ and for double-tags where (at least) one B has decayed via $(K^-\pi^+)\ell$. The Monte Carlo yields have been scaled to the on-peak dataset luminosity.

EventSample	single-tag $(K^-\pi^+)\ell$ vs generic B yield	double-tag $(K^-\pi^+)\ell$ vs $D^0\ell$ yield
B^+B^-	103544	440
$B^0\overline{B}^0$	58531	135
$c\bar{c}$	15814	4
uds	6772	0
$\tau^+\tau^-$	343	0
Total background Monte Carlo	185004	579
Total on-peak data	193476	651

bution is given in table 8.1. Each Monte Carlo type has been scaled to the on-peak data luminosity. In all generic Monte Carlo decays:

$$\frac{(K^-\pi^+)\ell \text{ vs } D\ell\nu}{(K^-\pi^+)\ell \text{ vs generic } B} = \frac{579}{185004} = (3.130 \pm 0.0.069) \times 10^{-3} \tag{8.6}$$

In the on-peak data:

$$\frac{(K^-\pi^+)\ell \text{ vs } D\ell\nu}{(K^-\pi^+)\ell \text{ vs generic } B} = \frac{651}{193476} = (3.365 \pm 0.130) \times 10^{-3} \tag{8.7}$$

Therefore, the double–tag/single–tag ratio comparison, after correctly evaluating and subtracting the combinatorial contribution from the sidebands, yields,

$$\frac{\text{data}}{\text{MonteCarlo}} = 1.078 \pm 0.045 \tag{8.8}$$

The double–tagged events are also useful for testing the simulation of E_{extra}, the unassigned neutral energy in the detector. This provides a convenient way to compare Monte Carlo and data in E_{extra} as, in these events, both B's are reconstructed, leaving all other measured neutral clusters to be considered as E_{extra}. The plots in figure 8.2 show the data and simulation for the remaining neutral energy after assigning all energy associated with both tag candidates in the event. Comparing the mean E_{extra} we extract from all Monte Carlo simulation = 0.46±0.04 GeV and from data = 0.48±0.04 GeV.

In order to evaluate a systematic error from these distributions we compare the yield of events with and without a cut applied to E_{extra}. This ratio is then compared between data and simulation. We choose to apply a cut at 400 MeV for this purpose. The choice of 400 MeV was made to account for neutral energy from both B's. It was chosen to mimic the 250 MeV cut from the signal search with an additional amount

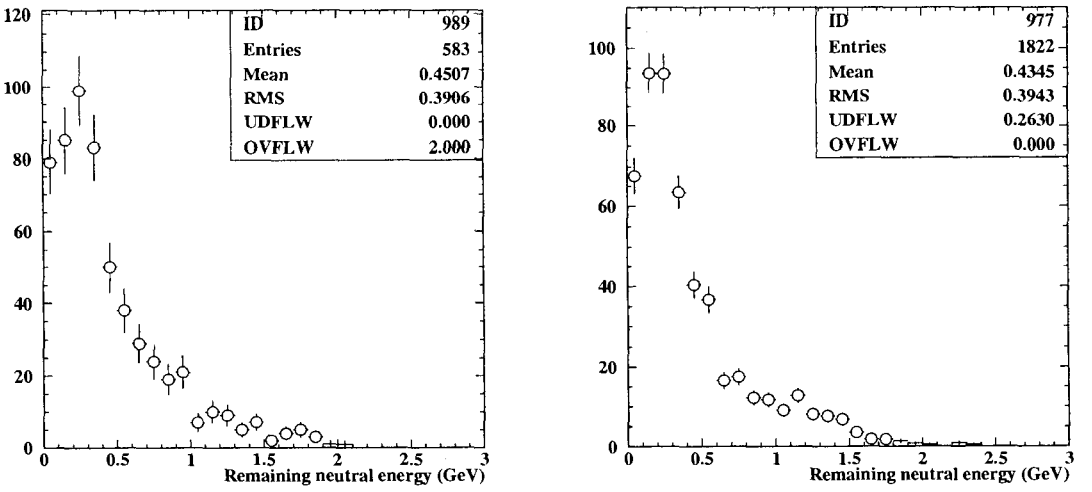

Figure 8.2: E_{extra} distribution for double-tagged events. We plot on-peak data(left) and All Monte Carlo simulation(right). The mean and error from these distributions are used to calculate the correction to the efficiency and the systematic error.

of neutral energy potentially produced by the other reconstructed B. Some neutral energy comes from beam backgrounds and other non-physics sources and so does not scale with the number of tag particles. The data/Monte Carlo ratio is for the most part insensitive to this choice as the ratio remains relatively stable for 50 MeV intervals from 250→500 MeV.

In data 0.562±0.019 of the distribution lies below the cut and in Monte Carlo 0.581±0.011 lies below the cut. A factor of 0.967±0.038 is extracted from this procedure. The difference between data and simulation is used as a correction factor. The statistical error in this procedure is taken to be the systematic error associated with the E_{extra} cut.

8.3 Systematics

In the analyses described herein, we are attempting to set an upper limit on the reactions $B^+ \to K^+\nu\overline{\nu}$ and $B^+ \to \pi^+\nu\overline{\nu}$. This is done under the assumption that

all events remaining in the signal region, after performing a sideband subtraction to remove the combinatorial background component, are signal events. If all selected events are treated this way for the purposes of setting an upper limit then only uncertainties on the efficiency need to be worried about; Systematic uncertainties due to backgrounds need not be directly addressed, since the background yield is not being explicitly used. For the most part the systematic errors can be separated into those associated with the tagging B and those on the signal side. For the tagging B it is sufficient to address only the uncertainty of the tagging efficiency whereas for the signal side each of the applied selection criteria will be discussed. A summary of the systematic errors is given in table 8.2.

8.3.1 Systematic Error on the Normalization

The procedure used to determine the total number of events with $\Upsilon(4S) \rightarrow B\overline{B}$ decays is reported in [60]. The systematic error quoted in this document is 1.1 %, which is taken to be the systematic uncertainty associated with the overall normalisation.

8.3.2 Systematic Error on the tagging efficiency

In order to extract the correction to the tagging efficiency a "double tag" study has been performed as was outlined in section 8.2. This method yields a systematic uncertainty of 4.5 % on the tagging efficiency. The tagging efficiency systematic uncertainty accomodates all effects in the reconstruction of the tag B such as errors on branching fractions and detector modeling.

8.3.3 Systematic Error on the signal selection criteria

A systematic uncertainty of 3.8 % is assigned to E_{extra} using the method described in section 8.2. It is assumed that a systematic error on the $\cos\theta_{\vec{T},K}$ is negligible since the

Table 8.2: A summary of the systematic errors for $\mathcal{B}(B^+ \to K^+\nu\bar{\nu})$. $\delta\epsilon/\epsilon$ is the relative uncertainty on the overall efficiency.

Quantity	$\delta\epsilon/\epsilon$[%]
B–counting	1.1
tagging efficiency	4.5
Kaon selection	2.0
$\cos\theta_{\vec{T},K}$	negligible
E_{extra}	3.8
Kaon momentum	3.0

signal Monte Carlo is evenly distributed in this variable. For the kaon identification a systematic uncertainty is extracted from the paper describing kaon identification [59] and the specific selector that was used. Further efforts from the particle identification group within *BABAR* suggest that a conservative uncertainty of 2 % be used. For the kaon momentum distribution an uncertainty is extracted using the reweighting of the signal Monte Carlo distribution to the correct theoretical model as described in section 6.8. The uncertainty extracted from this method is 3%.

8.3.4 Total Systematic Uncertainty

The systematics from section 8.3.1, 8.3.2 and 8.3.3 are summarized in table 8.2. All systematic uncertainties are combined in quadrature.

In combining these systematic uncertainties the total relative uncertainty on the selection efficiency is found to be

$$\delta\epsilon/\epsilon = 7.0\ \%. \tag{8.9}$$

Chapter 9

Search for $B^+ \rightarrow \pi^+ \nu\overline{\nu}$

In addition to the search for $B^+ \rightarrow K^+ \nu\overline{\nu}$ we perform a search for the reaction $B^+ \rightarrow \pi^+ \nu\overline{\nu}$. The analysis method is identical to that described in chapters 5, 6 and 7 except for the particle identification criteria imposed on the signal candidate track. As was discussed in section 2.3.2 the reaction $B^+ \rightarrow \pi^+ \nu\overline{\nu}$ is suppressed in the SM (compared to the $b \rightarrow s$ transition) by the factor $|V_{td}/V_{ts}^*|^2$. The search is performed in parallel to the $B^+ \rightarrow K^+ \nu\overline{\nu}$ search. The sensitivity to this decay is reduced since there is inherently greater background in the $B^+ \rightarrow \pi^+ \nu\overline{\nu}$ channel than in $B^+ \rightarrow K^+ \nu\overline{\nu}$. The higher background can be understood by the average multiplicity of pions per event being greater than that of kaons. Much of the background is from real $B^- \rightarrow D^0 \ell^- \overline{\nu}\, X$ combinations and is therefore peaking in the signal region for the D^0 mass. Possible new physics that may manifest itself in this channel would be from similar models to those outlined in chapter 2 for the $B^+ \rightarrow K^+ \nu\overline{\nu}$ channel. The main motivation for performing a search for $B^+ \rightarrow \pi^+ \nu\overline{\nu}$ therefore is that no search has ever been carried out for this process and there is no published measurement.

We use the same sample of $B^- \rightarrow D^0 \ell^- \overline{\nu}\, X$ tags and use a phase-space generated model for the $B^+ \rightarrow \pi^+ \nu\overline{\nu}$ simulated signal MC. The same selection criteria are applied aside from the particle identification of the signal track being treated

differently. For the $B^+ \to \pi^+\nu\overline{\nu}$ search we veto any tracks satisfying tight K identification (as described in section 6.1) or tight electron identification (as described in appendix A). No veto is applied based on muon identification. Hence we explicitly veto those events selected in the $B^+ \to K^+\nu\overline{\nu}$ search and any identified electrons. The decision to resist placing a veto on muon candidates was taken due to the high π as μ misidentification and the potential complication this could incorporate when interpreting a limit. So any charged track that does not satisfy our veto criteria is considered a pion and accepted as a potential signal candidate. No background subtraction is performed and for the sake of producing a conservative upper limit at 90% confidence level all candidates are taken as signal events. We assume this introduces no further systematic uncertainties. The same corrections calculated using the double-tag sample are applied.

It should be noted that all of the data/simulation comparison plots shown in chapter 5 would remain unchanged for this analysis. Plots for signal and background are shown for the pion momentum distribution and for the remaining neutral energy in figure 9.1. The $B^+ \to \pi^+\nu\overline{\nu}$ signal Monte Carlo distribution is shown in figure 9.2. The cut flow tables for signal and background are included to show the level of agreement between data and simulation and also to provide the final efficiency for the search, as used in the limit extraction. These numbers are given in tables 9.1 and 9.2. The background yield in Monte Carlo can be seen in figure 9.3. The yield in data for the $B^+ \to \pi^+\nu\overline{\nu}$ search can be seen in figure 9.4.

The final efficiency we extract from table 9.1 for the $B^+ \to \pi^+\nu\overline{\nu}$ search is 1.16×10^{-3}. Using the background yield in Monte Carlo we can extract an upper limit on the branching fraction at 90% confidence level. We use the same systematic corrections as imposed in the $B^+ \to K^+\nu\overline{\nu}$ search outlined in chapter 8 except

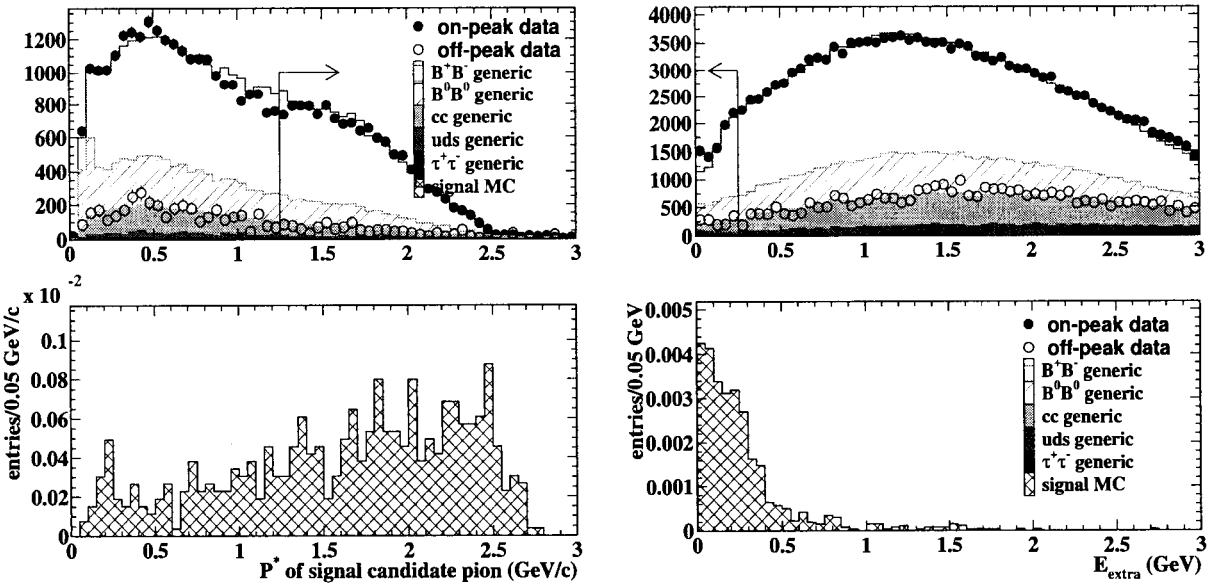

Figure 9.1: A plot of the momentum of the signal candidate track (left) and E_{extra} (right) after all the tag side particles have been removed. All modes using all Monte Carlo ($B\overline{B}$, $q\overline{q}(q = u, d, s$ or $c)$ and $\tau^+\tau^-$), onpeak and offpeak data. All distributions are scaled to the onpeak data luminosity. The $B^+ \to \pi^+\nu\overline{\nu}$ signal Monte Carlo is plotted for comparison.

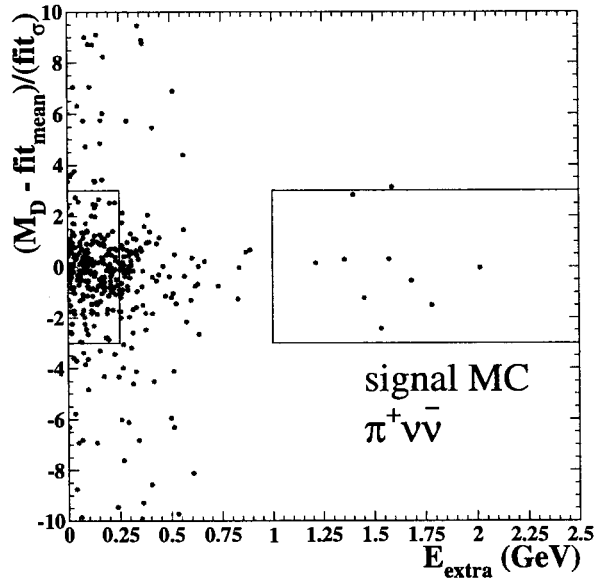

Figure 9.2: Signal Monte Carlo distribution for $B^+ \to \pi^+\nu\overline{\nu}$ search showing number of sigma from the mean of the D^0 mass vs E_{extra}.

Table 9.1: Cut-flow table for $B^+ \to \pi^+ \nu\overline{\nu}$ signal Monte Carlo where all numbers are unscaled. A correction is applied to the efficiency calculation where applicable.

	signal Monte Carlo		
Cut	Yield	Marginal efficiency	Cumulative efficiency
primordial	1.48×10^5	-	-
precuts	776	(5.26×10^{-3})	
Ntrkleft=1	565	0.73	
corrected efficiency	1.078	0.78	0.7827
PID veto	431	0.76	0.5971
$\cos\theta_{\vec{T},\pi}$	329	0.76	0.4558
p^*_π	237	0.72	
signal box	164	0.69	
corrected efficiency	0.967	0.67	0.2197
D^0 mass sideband	27	–	–
E_{extra} sideband	69	–	–

Table 9.2: Cut-flow table for on-peak data, off-peak data, all background and continuum background. The numbers in all tables have been scaled correspondingly to either the on or off-peak data sample luminosity. All background Monte Carlo is a sum of all on-peak contributions.

	on-peak data			background Monte Carlo		
Cut	Yield	Marginal efficiency	Cumulative efficiency	Yield	Marginal efficiency	Cumulative efficiency
primordial	4.42×10^8	-	-	4.41×10^8	-	-
precuts	664188			637321		
Ntrkleft=1	16160	0.0243	0.0243	14663	0.0230	0.0230
PID veto	8139	0.5030	0.0122	7507	0.5115	0.0118
$\cos\theta_{\vec{T},\pi}$	5386	0.6618	8.095×10^{-3}	4961	0.6608	7.783×10^{-3}
p^*_π	1483	0.2753	2.229×10^{-3}	1302	0.2624	2.043×10^{-3}
Big E_{extra} sideband	980	0.6608	1.473×10^{-3}	853	0.6554	1.339×10^{-3}
D^0 sideband	27	0.0182	4.058×10^{-5}	24	0.0183	3.736×10^{-5}
2-track sideband	293	0.1976	4.404×10^{-4}	312	0.2398	4.898×10^{-4}
3-track sideband	1445	0.9744	2.172×10^{-3}	1403	0.2398	2.202×10^{-3}
E_{extra} sideband	245	0.1652	3.682×10^{-4}	197.5	0.1517	3.099×10^{-4}
signal box	28	0.0189	4.208×10^{-5}	27.7	0.0213	4.347×10^{-5}
	off-peak data			continuum Monte Carlo		
Cut	Yield	Marginal efficiency	Cumulative efficiency	Yield	Marginal efficiency	Cumulative efficiency
primordial	0.41×10^8	-	-	0.42×10^8	-	-
precuts	11801			10985		
Ntrkleft=1	511	0.0433	0.0433	510	0.0464	0.0464
PID veto	276	0.5401	0.0234	280.00	0.5477	0.0255
$\cos\theta_{\vec{T},\pi}$	141	0.5109	0.0119	131	0.4665	0.0119
p^*_π	9	0.0638	7.627×10^{-4}	12	0.0923	1.097×10^{-3}
Big E_{extra} sideband	7	0.7778	5.932×10^{-4}	7	0.5515	6.047×10^{-4}
D^0 sideband	0	0.000	0.000	0.5	0.0381	4.173×10^{-5}
2-track sideband	0	0.000	0.000	0.6	0.0470	5.153×10^{-5}
3-track sideband	4	0.4444	3.390×10^{-4}	3.8	0.0470	3.431×10^{-4}
E_{extra} sideband	0	0.000	0.000	1.7	0.1388	1.522×10^{-4}
signal box	0	0.000	0.000	0.3	0.0275	3.019×10^{-5}

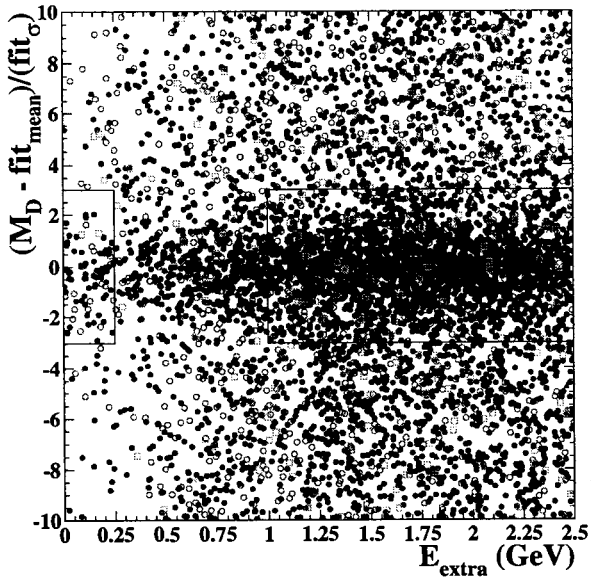

Figure 9.3: All background Monte Carlo distribution for $B^+ \to \pi^+\nu\overline{\nu}$ search showing number of sigma from the mean of the D^0 mass vs E_{extra}. The Monte Carlo is split up by type into B^+B^-(solid (blue) circles), $B^0\overline{B}^0$(open (red) circles), $c\bar{c}$(open (green) squares) and uds(solid (red) triangles).

for that associated with the kaon identification. This is clearly not relevant for the $B^+ \to \pi^+\nu\overline{\nu}$ search. Instead we impose a 5% systematic uncertainty for both the pion and electron vetos. This is considered a particularly conservative course to take. Adding these in quadrature with the other systematic errors yields a systematic uncertainty of $\delta\epsilon/\epsilon = 8.4\%$.

The data yield is shown in figure 9.4. In figure 9.5 the unblinded distributions for E_{extra} and p^*_π are presented in a similar way to those for the $B^+ \to K^+\nu\overline{\nu}$ analysis. The results of this search are given in chapter 10.

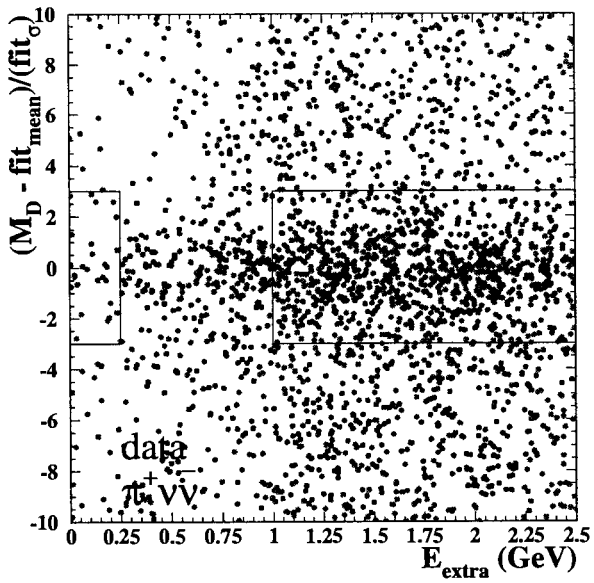

Figure 9.4: Unblinded onpeak data distribution for $B^+ \to \pi^+\nu\overline{\nu}$ search showing number of sigma from the mean of the D^0 mass vs E_{extra}.

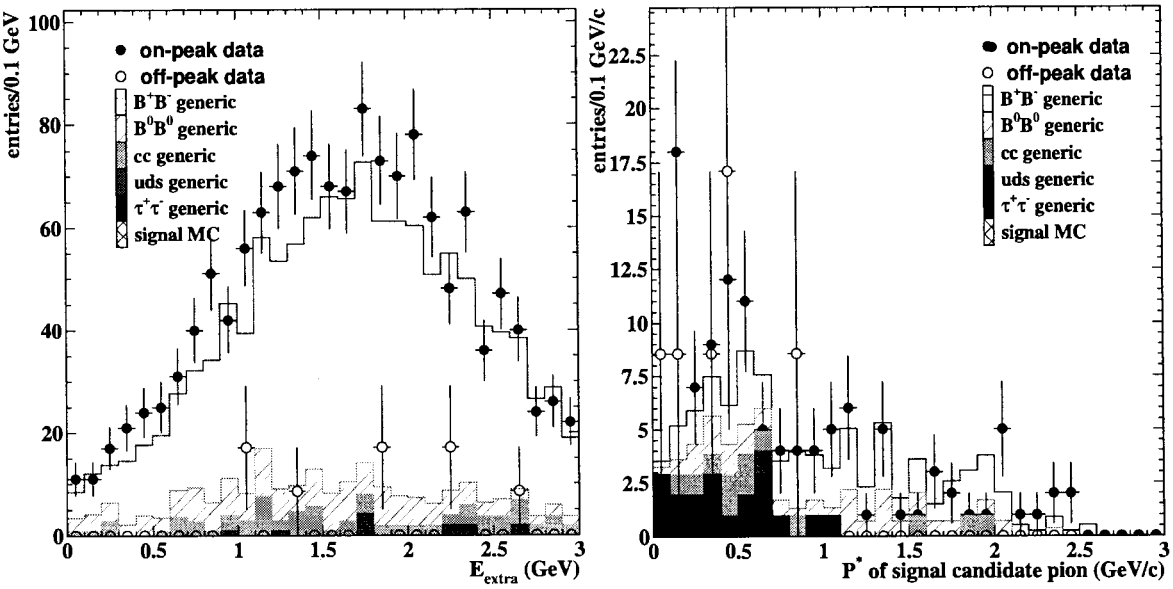

Figure 9.5: Unblinded distribution showing the E_{extra} and p^*_π for all Monte Carlo contributions with the data overlayed for the $B^+ \to \pi^+\nu\overline{\nu}$ channel. The $p^*_\pi > 1.25$GeV/c cut is applied to the E_{extra} plot and the $E_{extra} < 0.25$GeV is applied to the p^*_π distribution.

Chapter 10

Results

Our method of extracting the branching fraction is a 'cut-and-count' comparison between the signal box and E_{extra} sideband in Monte Carlo and data. Unblinding yields the number of observed events in the signal box (N_{obs}). The upper limit follows from

$$\mathrm{UL}_{90\%} = \frac{N^{90\%}_{\mathrm{signal}}}{N_{B^+} \cdot \epsilon}, \tag{10.1}$$

where $N^{90\%}_{\mathrm{signal}}$ is the 90% confidence level upper limit on the number of background-subtracted signal events, N_{B^+} is the number of B^+ mesons produced in the data and ϵ is the overall signal efficiency. We know $N_{B^+} + N_{B^-} = N_{B\overline{B}}$ under the assumption of an equal production of $B^0\overline{B}^0$ and B^+B^- in $\Upsilon(4S)$ decays. In the combined Run1 and Run2 data set with a luminosity of 81.9 fb^{-1} B-counting [60] yields $N_{B\bar{B}} = (88.9 \pm 1.0) \times 10^6$. In section 10.1 we quote the number of events. The upper limit was derived after subtracting the sidebands from the signal region with the appropriate scaling factor.

We begin by selecting a value for $N^{90\%}_{\mathrm{signal}}$. A random number A is generated on a Gaussian distribution with a mean of 1 and a standard deviation, σ, equal to the percentage systematic error on the efficiency $\delta\epsilon/\epsilon$. A second random number n is gen-

erated on a Poisson distribution with mean $N_{\rm signal}^{90\%}/A$. The question is then asked how often the n thus sampled is larger than the observed number of background subtracted signal events in the experiment. This toy experiment is repeated 10000 times. The process is iterated until the probability is 0.90, averaged over these samplings, then this value is used as $N_{\rm signal}^{90\%}$ in the 90% confidence level calculation. The procedure used to extract the 90% confidence level upper limit is described elsewhere [61].

It should be noted that the method used for these analyses is only valid for setting an upper limit and, even with a considerable number of observed events in the data, we would be unable to claim a signal. This course was considered reasonable since our sensitivity is a long way from the Standard Model predictions in these modes.

Table 10.1 contains entries quoting the observed number of events and the efficiency as a function of the cut applied to the p^* of the K candidate for the on-peak data. The final efficiency for all cuts prior to the p_K^* cuts given is 1.485×10^{-3}. The efficiency of each p_K^* bin (the fraction of the entire distribution contained within that bin) is then given in table 10.1. The background yields given are for the D^0 mass sidebands which need to be scaled by the factor 3/7 to subtract them from the signal region yield.

10.1 After unblinding

After unblinding the signal region for $B^+ \to K^+\nu\overline{\nu}$ it was found that the number of observed events was

$$N_{obs} = 6 \text{ events.} \tag{10.2}$$

Scaling the yield from the D^0 mass sidebands gives 3.4±1.2 background events.

The unblinded distribution is plotted in figure 10.1. Using the yield from table 7.3

Table 10.1: A table to show the p_K^* yield in on-peak data as a function of the cut range and the model.

p_K^*	Number of Events		
(GeV/c)	Yield	Background×7/3	Efficiency
1.00–1.25	3	4	0.085905
1.25–1.50	2	3	0.099527
1.50–1.75	3	2	0.128996
1.75–2.00	1	0	0.140395
2.00–2.25	0	1	0.181262
2.25–2.50	0	1	0.183486
2.50–2.75	0	1	0.077843
2.75–3.00	0	0	0.001668

we found an efficiency of 1.201×10^{-3}. However, due to the non-zero yield from signal Monte Carlo in the D^0 mass sidebands, as is evidenced from figure 7.7, we need to subtract the scaled yield in the D^0 mass sideband region from the signal region prior to extracting the final signal efficiency. This procedure reduces our signal efficiency to 1.151×10^{-3}.

From this study, we set an upper limit on the branching fraction, at 90% confidence level, of

$$\mathcal{B}\,(B^+ \to K^+\nu\overline{\nu}\,) < 7.2 \times 10^{-5}. \tag{10.3}$$

The same blinding strategy as defined in section 7.1 was used for the $B^+ \to \pi^+\nu\overline{\nu}$ search. After unblinding the result, we found that, in the signal region,

$$N_{obs} = 28 \text{ events}, \tag{10.4}$$

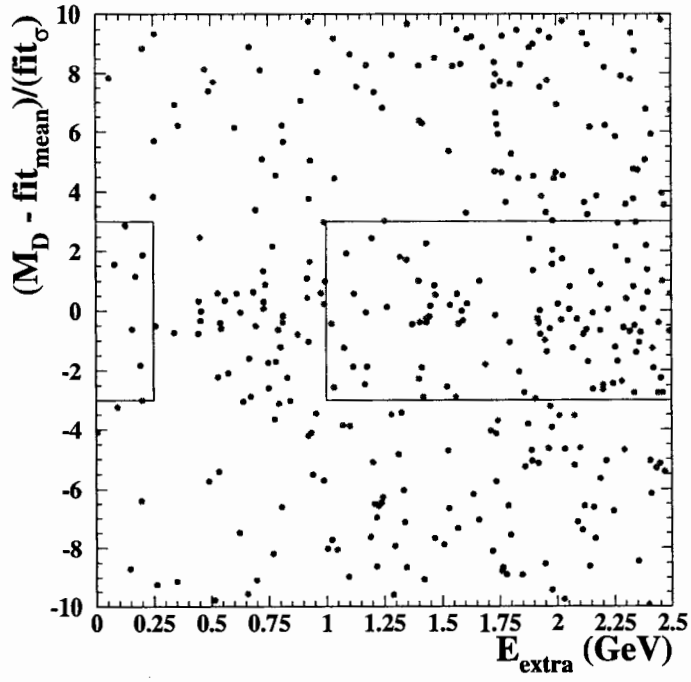

Figure 10.1: Unblinded distribution showing number of sigma from the mean of the D^0 mass vs the remaining neutral energy.

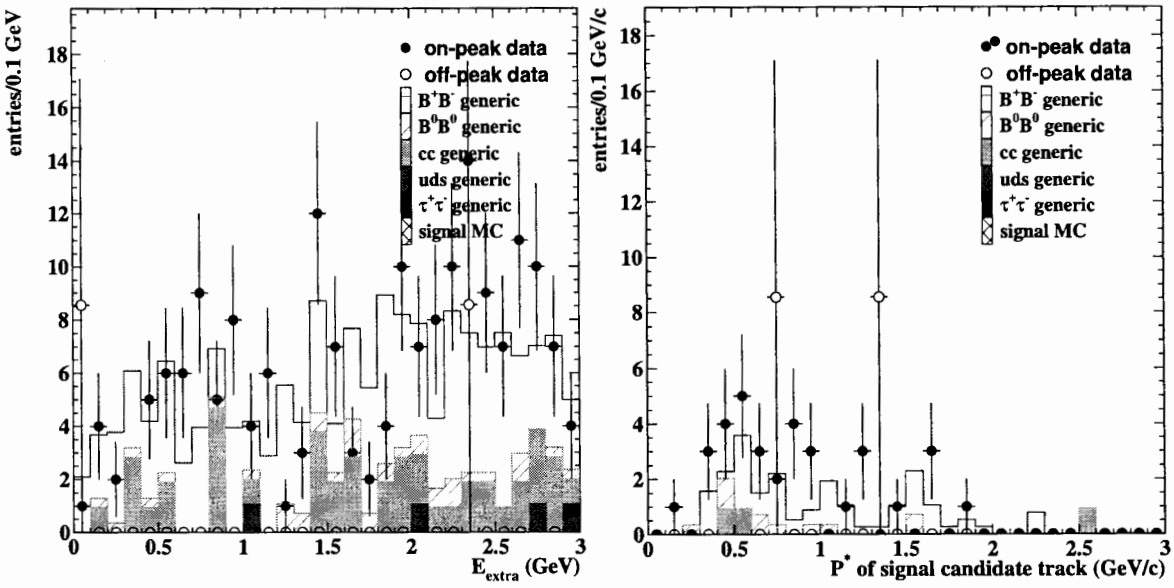

Figure 10.2: Unblinded distribution showing the E_{extra} and p*K for all Monte Carlo contributions with the data overlayed. The p^*_K >1.25 GeV/c cut is applied to the E_{extra} plot and the E_{extra} <0.25 GeV is applied to the p*K distribution.

which is in very good agreement with the background expectation from Monte Carlo. The scaled number of background events is 11.6±2.2. Using the prescription mentioned above we find that, if we subtract the scaled combinatorial background component from the D^0 mass sidebands, we set an upper limit on the branching fraction, at 90% confidence level, of

$$\mathcal{B}\,(B^+ \rightarrow \pi^+ \nu\overline{\nu}\,) < 2.5 \times 10^{-4}. \tag{10.5}$$

One should note that this limit is based on a phase-space model for the $B^+ \rightarrow \pi^+ \nu\overline{\nu}$ decay.

10.2 Interpretation of results

The limit quoted in equation 10.3 is an improvement on the previous best published limit but still someway short of the expected Standard Model branching fraction, both of which were quoted in section 2.3.2. No discernible evidence for processes beyond the Standard Model was observed during this search. This is evidenced by the plots in figure 10.2. If there were hints of a signal there would be a peaking component in the data that is not present in the simulation in the E_{extra} and p_K^* distributions. Clearly no such component is visible, although perhaps one could make a claim that at kaon momenta lower than 1 GeV/c there is an excess of data over simulation, but this is far from statistically compelling.

We can constrain contributions from beyond the Standard Model using the limit we extracted. As outlined recently in the literature [38] the $B \rightarrow K$+missing energy process is sensitive to the effect of light dark matter scalars below masses of around 2.2 GeV/c^2. Since no effect is seen in the data this model described in [38] is constrained by this result.

Chapter 11

Conclusions

A search for the rare, flavour-changing neutral current decay $B^+ \to K^+\nu\overline{\nu}$ in 81.9 fb^{-1} of data collected at the $\Upsilon(4S)$ resonance by the *BABAR* experiment has been presented. Signal candidate events were selected through the identification of a high momentum charged kaon and significant missing energy, where the other B meson in the event has decayed semileptonically via $B^- \to D^0\ell^-\overline{\nu}\,X$ and X is kinematically constrained to be either nothing or a low momentum photon or π^0. The analysis was performed blind and 6 candidates were selected with a combinatorial background expectation of 3.4±1.2. This leads to an upper limit on the branching fraction of $\mathcal{B}\,(B^+ \to K^+\nu\overline{\nu}\,) < 7.2 \times 10^{-5}$ at 90% confidence level. An additional search for the reaction $B^+ \to \pi^+\nu\overline{\nu}$ was performed and an upper limit on the branching fraction of $\mathcal{B}\,(B^+ \to \pi^+\nu\overline{\nu}\,) < 2.5 \times 10^{-4}$ at 90% confidence level was extracted.

No evidence for physics beyond the Standard Model was observed in either of the two channels.

Bibliography

[1] A. Einstein, Annalen Phys. **17**, 891 (1905).

[2] V. Fock, Z. Phys. **39**, 226 (1926) [Surveys High Energy Physics **5**, 245 (1926)].
H. Weyl, Z. Phys. **56**, 330 (1929) [Surveys High Energy Physics **5**, 261 (1929)].
C. N. Yang and R. L. Mills, Phys. Rev. **96**, 191 (1954).

[3] Y. Nambu, Phys. Rev. Lett. **4**, 380 (1960).
J. Goldstone, Nuovo Cim. **19**, 154 (1961).
J. Goldstone, A. Salam and S. Weinberg, Phys. Rev. **127**, 965 (1962).
P. W. Higgs, Phys. Rev. Lett. **12**, 132 (1964).
P. W. Higgs, Phys. Rev. Lett. **145**, 1156 (1966).

[4] M. Y. Han and Y. Nambu, Phys. Rev. **139**, B1006 (1965).

[5] S. L. Glashow, Nucl. Phys. **22**, 579 (1961).
S. Weinberg, Phys. Rev. Lett. **19**, 1264 (1967).
A. Salam, *Originally printed in *Svartholm: Elementary Particle Theory, Proceedings of the Nobel Symposium Held 1968 at Lerum, Sweden*, Stockholm, 1968, 367-377.*

[6] M. Kobayashi and T. Maskawa, Prog. Theor. Phys. **49**, 652 (1973).

[7] S. L. Glashow, J. Illiopolous and L. Maiani, Phys. Rev. D**2**, 1285 (1970).

[8] S. Weinberg, Phys. Rev. Lett. **27** 1688 (1971).

[9] F. Abe *et al.*, CDF Collaboration, Phys. Rev. Lett. 73 (1994) 225, Phys. Rev. D50 (1994) 2966, Phys. Rev. D51 (1995) 4623, Phys. Rev. Lett. 74 (1995) 2626, Phys. Rev. D52 (1995) R2605; S. Abachi *et al.*, D0 Collaboration, Phys. Rev. Lett. 74 (1995) 2632.

[10] K. G. Wilson, Phys. Rev. **179**, 1499 (1969).

[11] B. Aubert *et al.*, *BABAR* collaboration. Phys. Rev. Lett. **91** 221802 (2003).

[12] P. Colangelo, F. De Fazio, P. Santorelli, E. Scrimieri "Rare $B \to K^* \nu\overline{\nu}$ Decays at B factories." hep-ph/9610297.

[13] T. Inami and C. S. Lim, Prog. Theory. Phys. 65 (1981) 287.

[14] G. Buchalla and A. J. Buras, Nucl. Phys. B400 (1993) 225.

[15] For a review see: G. Buchalla, A. J. Buras and M. E. Lautenbacher, report MPI-Ph/95-10, TUM-T31-100/95, Fermilab-Pub.95/305-T, SLAC-PUB 7009, hep-ph/9512380.

[16] G. Isidori, "Rare decays: theory vs experiment", CERN-TH/2001-284 (presented at Lepton Photon 01, Rome, July 2001).

[17] D. Melikhov, N. Nikitin and S. Simula, "Rare decays $B \to (K, K^*)(\ell^+\ell^-, \nu\overline{\nu})$ in the quark model". INFN-ISS 97/2, hep-ph/9704268.

[18] Y. Grossman, Z. Ligeti, E. Nardi, "New limit on the inclusive $b \to s\nu\overline{\nu}$ decay and constraints on new physics"
Nucl. Phys. **B465**:369-398,1996, Erratum-ibid.**B480**:753-754 (1996).

[19] G. Buchalla, G. Hiller and G. Isidori,
"Phenomenology of non-standard Z couplings in exclusive semileptonic $b \to s$ transitions" hep-ph/0006136 v2.

[20] A. Faessler *et al.*, "The exclusive rare decays $B \to K\bar{\ell}\ell$ and $B_c \to D(D^*)\bar{\ell}\ell$ in a relativistic quark model" hep-ph/0205287.

[21] T. M. Aliev, C. S. Kim, "Measuring V_{td}/V_{ub} through $B \to M\nu\overline{\nu}$ ($M = \pi$, K, ρ, K^*) decays." hep-ph/9710428.

[22] C. S. Kim, Y. G. Kim and T. Morozumi, "New Physics Effects in $B \to K^{(*)}\nu\nu$ Decays" hep-ph/9905528.

[23] X. Zhenjun, Y. Liping, "Rare $B \to X_s\nu\overline{\nu}$ in the two-Higgs-doublet model of type III." hep-ph/0212008.

[24] T. M. Aliev, A. Ozpineci, M. Savci "Rare $B \to K^*\nu\overline{\nu}$ decay beyond the Standard Model." hep-ph/01011066.

[25] C. Bobeth, A. J. Buras, F. Kruger, J. Urban, "QCD Corrections to $B \to X_{d,s}\nu\overline{\nu}$, $B_{d,s} \to \ell^+\ell^-$, $K \to \pi\nu\overline{\nu}$ and $K_L^0 \to \mu^+\mu$m in the MSSM" hep-ph/0112305.

[26] A. J. Buras, R. Fleischer, S. Recksiegel, F. Schwab, "$B \to \pi\pi$, New Physics in $B \to \pi K$ and implications for Rare K and B Decays." hep-ph/0312259, CERN-TH/2003-314.

[27] D. Guetta and E. Nardi "Searching for New Physics in rare $B \to \tau$ Decays" hep-ph/9707371.

[28] B. Holdom and M. V. Ramana "New flavor physics in b decays" hep-ph/9509272.

[29] A. J. Buras, M. Spranger, A. Weiler, "The Impact of Universal Extra Dimensions on the Unitarity Triangle and Rare K and B Decays" hep-ph/0212143.

[30] G. Buchalla, G. Burdman, C. T. Hill, D. Kominis, "GIM Violation and New Dynamics of the Third Generation." hep-ph/9510376, FERMILAB-PUB-95/322-T.

[31] G. Isidori "Supersymmetric effects in rare semileptonic decays of B and K mesons." hep-ph/0101121, CERN-TH/2001-003.

[32] D. Melikhov, N. Nikitin and S. Simula "Right-handed currents in rare exclusive $B \to (K, K^*)\nu\overline{\nu}$ decays." hep-ph/9803269, INFN-ISS 98/2.

[33] T. Barakat, "The $B \to K^*\nu\overline{\nu}$ rare decay in the two-Higgs doublet model". J. Phys. G:Nucl. Part. Phys. **24** 1903-1912 (1998).

[34] T. M. Aliev and M. Savci "Exclusive $B \to \pi\ell^+\ell^-$ and $B \to \rho\ell^+\ell^-$ decays in two Higgs doublet model" hep-ph/9812272.

[35] T. M. Aliev, C. S. Kim and M. Savci "Exclusive $B \to M\ell^+\ell^-$ ($M = \pi$, K, ρ, K^*) Decays and Determinations of $\mid V_{ts} \mid$ (and $\mid V_{td}/V_{ts} \mid$)." hep-ph/9804456 v2.

[36] M. S. Alam *et al.*, CLEO Collaboration. Phys. Rev. Lett. **74**, 2885 (1995). For results from an updated analysis see T. Skwarnicki, talk presented at XXIXth International Conference on High Energy Physics, Vancouver, Canada (1998).

[37] C. P. Burgess, M. Pospelov and T. ter Veldhuis, "The Minimal Model of Non-baryonic Dark Matter: A Singlet Scalar" hep-ph/0011335.

[38] C. Bird, P. D. Jackson, R. V. Kowalewski and M. Pospelov, "Search for dark matter scalars in $b \to s$ transitions with missing energy". hep-ph/0401195

[39] P. F. Harrison and K. R. Quinn, *BABAR* Collaboration. "The *BABAR* Physics Book: Physics at an asymmetric B factory", SLAC-R-504 (1998).

[40] R. Barate *et al.*, ALEPH Collaboration. Eur. Phys. J. **C19**:213-227 (2001).

[41] T. E. Browder *et al.*, CLEO Collaboration. Phys. Rev. Lett. **86**:2950-2954 (2001).

[42] C. Caso *et al.*, Particle Data Group. Review of Particle Physics (2002).

[43] B. Aubert *et al.*, *BABAR* Collaboration. Nucl. Instr. and Methods **A479**, 1 (2002).

[44] J. D. Richman, "The *BABAR* silicon vertex tracker", Nucl. Instr. and Methods **A409**, 219-223 (1998).

[45] G. Sciolla, "The *BABAR* drift chamber", Nucl. Instr. and Methods **A419** 310-314 (1998).

[46] D. W. G. S. Leith, "DIRC-the particle identification system for *BABAR*", Nucl. Instr. and Methods **A494** 389-401 (2002).

[47] The vender of fused silica: TSL Group PCL,
P.O. Box 6, Wallsend, Tyne & Wear, NE28 6DG, England.
Quartz Products Co., 1600 W. Lee St., Louisville, Kentucky 40201.
Manufacturer of quartz bars: Boeing, Rockedyne Division, 2511 C Broadbent Parkway NE, Albuquerque, New Mexico 87107.

[48] B. Lewandowski, "The *BABAR* electromagnetic calorimeter", Nucl. Instr. and Methods **A494**, 303-307 (2002).

[49] R. Santonico, R. Cardarelli, Nucl. Instr. Methods A187 (1981) 377.

[50] D. Boutigny *et al.*, *BABAR* Collaboration. Technical design report, SLAC-R-95-457 (1995)

[51] The *BABAR* Simulation Production Group.
Generating Monte Carlo Events with `GenFwkInt`.
http://www.slac.stanford.edu/BFROOT/www/Physics/Tools/generators/GenFwkInt/GenFwkInt.html.

[52] S. Agostinelli *et al.*, `GEANT4` Collaboration. Nucl. Instr. and Meth. **A506**, 250 (2003).

[53] A. Drescher *et al.*, Nucl. Instrum. and Methods **A237**, 464 (1985).

[54] G. C. Fox, S. Wolfram, Phys. Rev. Lett., **41** 1581 (1978).

[55] P. D. Jackson *et al.*, "Tagging using $B \to D\ell\nu(X)$ decays" *BABAR* Analysis Document #537.

[56] S. Sekula *et al.*, *BABAR* Analysis Document #417.

[57] J. Albert *et al.*, *BABAR* Analysis Document #525.

[58] D. Lange, "Study of K_L^0 identification using the EMC", *BABAR* Analysis Document #59.

[59] S. Spanier and G. Mancinelli, "Kaon Identification in the *BABAR* Experiment ", *BABAR* Analysis Document #116.

[60] C. Hearty, "Measurement of the number of $\Upsilon(4S)$ mesons produced in Run 1 (B Counting)", *BABAR* Analysis Document #134.

[61] R. D. Cousins, V. L. Highland, Nucl. Instrum. Meth. **A320**:331-335 (1992)

[62] R. V. Kowalewski *et al.*, "Particle Selection criteria optimized for visible energy measurement", *BABAR* Analysis Document #633.

Appendix A

Lepton identification

A.1 Electron identification

The electron selector is a simple algorithm relying on a dedicated E/p calibration and the following variables:

- The ratio of the energy deposited in the EMC to the momentum of the particle measured at the origin. This is the variable with the most discriminating power.
- LAT is a shower shape variable quantifying the lateral shower profile.
- $|A_{42}|$ is a Zernike moment used to describe the azimuthal shower profile.
- Consistency with the electron hypothesis of the Cherenkov angle to within 3σ is required, if the number of photons expected (for the electron hypothesis) in the DIRC is $n_\gamma \geq 10$.
- Electromagnetic showers start on average earlier in the EMC and are more concentrated around the impact point than showers of hadronic interactions. Therefore they show a smaller azimuthal separation between the track impact point at the EMC and the centre of gravity of the associated cluster.

The following cuts are applied:

- $0.89 < E/p < 1.2$
- $0.1 < LAT < 0.6$
- $n_{Xtal} > 3$
- $|A_{42}| < 0.11$
- DIRC consistency with electron hypothesis
- Track cluster matching

A.2 Muon identification

For the muon selector the following cuts are applied:

- $0.05 < \mathrm{E_{cal}} < 0.4$ applied on track in the angular region covered by EMC θ(rad) < 2.45. E is the energy deposited in the EMC. The cut on this variable is only applied to those tracks that have a matching cluster in the EMC.
- $\mathrm{N_L} \geq 2$, $\mathrm{N_L}$ is the number of IFR layers in a cluster matched to the muon candidate.
- $\lambda > 2.2$, where λ is the measured interaction length traversed by a track in the entire detector.
- $\Delta\lambda > 0.8$, $\Delta\lambda$ is the difference between the expected and measured interaction lengths.
- $\chi^2_{\mathrm{trk}} < 5$, χ^2_{trk} measures how closely the hit IFR strips in a cluster match the track extrapolation.

- $\chi^2_{\rm fit} < 5$, $\chi^2_{\rm fit}$ is the χ^2 of the fit of all the hits in a given cluster to a $3^{\rm rd}$ order polynomial.

- $T_c > 0.34$ (applied only on tracks in the polar angle interval $0.3 < \theta({\rm rad}) < 1$). T_c describes the continuity of the track in the IFR.

- $\overline{\rm m} < 8$, where $\overline{\rm m}$ is the average multiplicity of hit strips per layer.

- $\sigma_{\rm m} < 4$, $\sigma_{\rm m}$ is the standard deviation of $\overline{\rm m}$

Appendix B

Selection criteria for neutral clusters

B.1 Neutral cluster selection

The selection criteria for neutral clusters have been studied. The goal is to optimize the reconstruction of visible energy while maintaining good agreement between data and simulation. This will be of paramount importance to the use of data-simulation comparison in the amount of remaining neutral energy visible in the detector after assigning tag-side tracks and clusters. Cuts are chosen so as to account for all relevant neutral energy contributions in these distributions. The selection criteria imposed and the studies which were carried out were motivated by the work outlined in [62].

All clusters in the `CalorNeutral` list for all events passing the $B^- \to D^0 \ell^- \overline{\nu}\, X$ selection criteria are considered. Contributions to this list can be from a number of sources and using Monte Carlo truth information these clusters can be categorized as follows:

- truth matched to photon or electron (i.e. from Bremsstrahlung)
- truth matched to charged particle (except electron)

- truth matched to neutral hadron (K_L^0 or neutron)
- no truth match.

The last three categories correspond to charged-track splitoffs, neutral hadron interactions in the EMC and beam background photons respectively. A number of cluster variables were studied in [62] and it was found that the following selection criteria isolated those clusters of particular interest to this analysis:

- Number of crystals in the cluster, $N_{crys} > 2$
- Energy of the cluster, $E_{clus} > 50$ MeV
- The polar angle of the cluster in the lab frame, $0.32 < \theta_{clus} < 2.44$
- Angle between the positions of the cluster and the impact point of the nearest charged track at the EMC surface, $\Delta\alpha > 0.15$. The cut is only applied to those tracks that do not pass the tight electron selector. No cut is made on this variable when the track is an electron (in order to retain Bremsstrahlung photons which contribute a reasonable amount of energy to the total remaining neutrals).

All of these selection criteria are motivated by the plots shown in [62]. It should be noted that the common practice of requiring $LAT > \epsilon$, where ϵ is a small value (e.g. 0.01) has the effect of cutting out clusters with less than 3 crystals. Cutting on the number of crystals is chosen to make the intention of the selection obvious.

B.2 D^{*0} reconstruction using single photons and $D^0\ell$ candidates.

One method of reducing the unassigned, remaining neutral energy is to include any potential transition photons from the charm state decay involved in a $B^- \rightarrow D^{*0}\ell^-\overline{\nu}$ decay. In the tag reconstruction this is not explicitly done and hence the neutrals from $D^{*0} \rightarrow D^0\pi^0/\gamma$ will be considered extra neutral energy remaining in the event. Indeed studies show that much of the neutral energy comes from this source.

In order to assign photons from D^{*0} decays to the tag-sde of the event we impose certain criteria to limit adding random background photons to the tag. The best tag candidate in an event is defined using the $\cos\theta_{B,D\ell}$ variable. Hence if a photon is to be added to the tag, the resultant value of $\cos\theta_{B,D^{*0}\ell}$, using the D^{*0} as the meson candidate, should now be within the physical region of ± 1.1 (where we allowed the "physical region" to extend to 1.1 to account for possible reconstruction and detector effects). The inclusion of this additonal photon to the D^0 should not yield a meson of mass greater than the PDG value of the D^{*0} mass [42]. The mass difference between the D^{*0} and D^0 is 142 MeV hence we only accept those candidates that have a mass difference greater than 100 MeV and less than 150 MeV. The rather loose cut on the lower bound is to account for our adding single photons from π^0's where, in reality two photons were present (the reconstruction of the π^0 and inclusion of both photons from it's decay is more challenging, and since the exercise of adding the highest energy photon involved in a $D^{*0}\rightarrow D^0$ transition accounts for most of the transition energy this is sufficient in largely reducing the unassigned neutral energy from these decays).